UNIVERSIDADE D
COIMBRA

Xavier Alexandre Leitão Pinheiro

DEVELOPMENT OF NANOLAMINATES FOR CARRIER SELECTIVITY

Thesis submitted to the University of Coimbra in fulfilment of the requirements for the Master's Degree in Engineering Physics under the scientific supervision of Ph.D. Jennifer Passos Teixeira and Professor Ph.D. Rui César Vilão.

October 2021

FACULDADE DE CIÊNCIAS E TECNOLOGIA
UNIVERSIDADE D COIMBRA

Xavier Alexandre Leitão Pinheiro

Development of Nanolaminates for Carrier Selectivity

Thesis submitted to the University of Coimbra for the fulfilment of the requirements for the Master's Degree in Engineering Physics.

Supervisor:
Ph.D. Jennifer Passos Teixeira

Co-Supervisor:
Professor Ph.D. Rui César Vilão

Coimbra, October 2021

This work was developed in collaboration with:

Nanofabrication for Optoelectronic Applications group - International Iberian Nanotechnology Laboratory

This work was financed by ***NovaCell*** - Development of novel Ultrathin Solar Cell Architectures for lowlight, low-cost, and flexible opto-electronic devices project (PTDC/CTM-CTM/28075/2017) co-funded by Fundação para a Ciência e a Tecnologia (FCT) and the European Regional Development Fund (ERDF) through COMPETE2020, by ***InovSolarCells*** - Development of innovative nanostructured dielectric materials for interface passivation in thin film solar cells project (PTDC/FISMAC/29696/2017) co-funded by FCT and the ERDF through COMPETE2020, and by ***Baterias 2030*** (POCI-01-0247- FEDER-046109) co-funded by Operational Programme for Competitiveness and Internationalisation (COMPETE 2020), under the Portugal 2020 Partnership Agreement, through the ERDF .

Agradecimentos

Começo por demonstrar a minha gratidão para com a Faculdade de Ciências e Tecnologia da Universidade de Coimbra, pela formação inestimável que me proporcionou, e também a todos os Professores do Departamento de Física, que de algum modo me acompanharam ao longo do meu percurso académico.

Ao Professor Pedro Manuel Parracho Salomé, por me acolher e me conceder esta oportunidade única de fazer parte da equipa do NOA e do INL. A todos os elementos do NOA por estes oito meses; foram colegas e amigos, e indespensáveis desde o início ao fim deste trabalho. ”Realmente um grupo extraordinário!” Aos meus orientadores, porque sem eles esta tese não existiria. Ao Professor Rui César Vilão, por toda a ajuda e disponibilidade mostrada, apesar da distância, e pela confiança depositada desde o princípio. À Dra. Jennifer Passos Teixeira, pela proximidade durante todo este trabalho e pela dedicação e tempo despendido, principalmente nas semanas antes da entrega. Quero também agradecer ao Professor José António Paixão, pelo auxílio e acompanhamento das medidas de XRD, que se incluem neste trabalho.

Aos meus amigos de infância e aos ”apêndices” que se foram juntando, por todas os momentos e fins de semana de ”refúgio” e desabafo durante estes cinco anos. À eterna Irmandade: Ala, Cidade, Luigi, Nuno, Rodrigo, Tremoço e Zé, pelas noites de estudo e de tantas outras coisas, trabalhos, cartadas no BM, cafés e jantaradas na ”Casa do Xavi”. Algo que não esquecerei! Não posso deixar de dar uma palavra muito especial à Alice, que me acompanha em tudo há quase 3 anos.

Por fim, agradeço à minha família, à qual não tenho palavras para expressar a minha gratidão e o quanto eles são importantes para mim: pais, irmão, padrinhos e primas e avós, com os quais, infelizmente, já não posso celebrar este momento. A eles não tenho palavras para expressar a minha gratidão e o quanto a presença deles na minha vida é importante. Só consigo deixar um imenso OBRIGADO!

Sem mais, celebro estes belíssimos cinco anos em Coimbra com um excerto da Balada da Despedida 2021, do grupo Capas ao Luar da Secção de Fado da AAC, que tão bem descreve os meus últimos momentos como estudante da Universidade de Coimbra.

”(...)
Canto a última vez
A história da viagem
Que me viu a crescer

E levo no peito
Um verso de saudade
Para um dia o voltar a ler

Levo amigos e memórias
O fado que me embala
A torre em sua glória
A guitarra que se cala

Oh Coimbra!
Mil poetas te choraram

Ficarás para a eternidade
Oh Coimbra do Mondego
Capas, guitarras e saudade
Dentro de mim em segredo”

Braga, 27 de Outubro de 2021

Resumo

Os compostos nanolaminados são estruturas multicamadas nanométricas que combinam materiais e que permitem a manipulação de propriedades fundamentais, que tipicamente não estão disponíveis nos materiais base, através do controlo da espessura e composição das subcamadas, bem como a estrutura geral. Este trabalho estabelece uma primeira abordagem para posterior desenvolvimento de contactos seletivos. Assim, foram estudadas camadas individuais e nanolaminados baseados em SiO_2, Si_3N_4, TiO_2, ZnO, e HfO_2, de modo a analisar o seu potencial como contactos seletivos para eletrões em células solares $Cu(In,Ga)Se_2$ (CIGS). As amostras foram depositadas recorrendo a técnicas com aplicabilidade industrial (Deposição Química na Fase de Vapor assistida por Plasma e Pulverização Catódica com Magnetrão) e as suas propriedades fundamentais foram examinadas através de técnicas de caracterização avançada. Medidas de Espectroscopia de Fotoeletrão de Raios-X permitiram determinar desvios na composição das camadas individuais amorfas: $SiO_{1.7}$, $SiO_{0.2}N_{1.0}$, $TiO_{2.1}$, $ZnO_{0.7}$, e $HfO_{1.8}$. As várias técnicas de caracterização envolvidas demonstraram a presença de multi-camadas, no entanto, com valores de espessura diferentes dos valores pretendidos. Foram observados desvios na composição dos nanolaminados, relativamente às camadas individuais, o que origina alterações nas propriedades de transporte elétrico. Assim, é necessária uma otimização dos métodos de deposição utilizados, de forma a permitir uma manipulação meticulosa. Na análise por métodos óticos, a aproximação de meio efetivo não descreve todos os nanolaminados, contudo o índice de refração foi manipulado com sucesso para valores compatíveis com a integração numa célula solar CIGS. Um nanolaminado com repetição dupla (5:10 nm) ZnO_x-TiO_x apresentou um desfasamento na banda de condução de 1.2 eV e na de valência de 1.7 eV, em relação ao CIGS. Adicionalmente, foi observada uma elevada capacidade de passivação de lacunas por efeito de campo que, em conjunto com os desfasamentos da estrutura eletrónica, origina uma camada capaz de bloquear lacunas e um melhoramento na seletividade de eletrões. O desenvolvimento de dispositivos permitiu estudar as propriedades elétricas e debater as limitações aquando da sua integração. No entanto para um estudo completo, é necessário a otimização de tais dispositivos. Com este trabalho, foi estabelecida uma diretriz para o desenvolvimento de contactos seletivos, baseados em nanolaminados. Os resultados deste trabalho monstram a possibilidade de manipular propriedades fundamentais, abrindo a porta para a criação de materiais *à la carte*.

Palavras-Chave - Nanolaminados, Contactos Seletivos, Nanofabricação, Caracterização Avançada, Dispositivos Optoelectrónicos

Abstract

Nanolaminates are compounds based on nanometric multilayered materials that allow for tailoring of fundamental properties, otherwise not available by individual layer materials, through the manipulation of sublayers composition, thickness, and design. The present work establishes the first approach, to further develop customized electron selective contacts based on nanolaminates. Thus, individual layers and complex nanolaminate systems based on nominal: SiO_2, Si_3N_4, TiO_2, ZnO, and HfO_2 were studied, in order to understand their potential to be integrated as an electron selective contact in Cu(In,Ga)Se_2 (CIGS) solar cells. For this purpose, fundamental properties were scrutinized through advanced characterisation. The samples were deposited via industrial compatible techniques, Plasma Enhanced Chemical Vapour Deposition and Magnetron Sputtering. Deviations in the elemental composition, determined by X-ray Photoelectron Spectroscopy (XPS) analysis, indicate amorphous single layers of $SiO_{1.7}$, $SiO_{0.2}N_{1.0}$, $TiO_{2.1}$, $ZnO_{0.7}$, and $HfO_{1.8}$ Moreover, XPS and Scanning Transmission Electron Microscopy results point to variations in the sublayer thickness in comparison to the nominal values and as well as a multilayer structure in the nanolaminate. Regarding composition, deviations were observed in the nanolaminate samples, compared to the individual layers, which lead to distinct conductive behaviours. Hence, the used upscale deposition methods need to be further optimized in order to provide meticulous control of the sublayers for efficient nano tailoring. From an optical point of view, the effective medium approximation does not provide an accurate description for all the studied nanolaminates. However, the refractive index was successfully tailored to a range compatible for integration in the aimed solar cell architecture. A two times bilayer 5:10 nm ZnO_x-TiO_x nanolaminate presented an electronic surface structure with an 1.2 eV conduction band offset for CIGS, and a valence band offset of 1.7 eV. Furthermore, a high hole field-effect passivation was obtained, in combination with the valence and conduction band offsets, this leads to an efficient hole blocking layer and improved electron selectivity. Custom devices developed to characterize the electric properties nanolaminate's, show no clear results, although, it is important to customize those to a specific objective. This approach allows to discuss possible working limitations of the nanolaminates structures when integrated in optoelectronic selectivity. Furthermore, these devices need to be further optimized in order to fully describe the electrical behaviour of the nanolaminates. In this work, a roadmap to selective contacts based on nanolaminates is given. The results of this work indicate the possibility of properties tailoring, allowing for materials *à la carte*.

Keywords - Nanolaminates, Selective Contacts, Nanofabrication, Advanced characterisation, Optoelectronic Devices

Acronyms

ALD Atomic Layer Deposition

ARC Anti Reflective Coating

CIGS Cu(In,Ga)Se_2

CVD Chemical Vapour Deposition

DWL Direct Write Lithography

EDS Energy Dispersive Spectroscopy

EQE External Quantum Efficiency

FF Fill Factor

GIXRD Grazing Incidence X-Ray Diffraction

HAADF High-angle Annular Dark-Field

PCE Power Conversion Efficiency

PE Power Efficiency

PECVD Plasma Enhanced Chemical Vapour Deposition

PV Photovoltaic

PVD Physical Vapour Deposition

QTD-TLM Quasi Two-Dimensional TLM

REELS Reflection Electron Energy Loss Spectroscopy

RF Radio Frequency

RSF Relative Sensing Factor

SEM Scanning Electron Microscopy

SLG Soda Lime Glass

STEM Scanning Transmission Electron Microscopy

TCO Transparent Conductive Oxide

TEM Transmission Electron Microscopy

TLM Transfer Length Method

TMO Transmission Metal Oxide

UPS Ultraviolet Photoelectron Spectroscopy

XPS X-ray Photoelectron Spectroscopy

XRD X-Ray Diffraction

List of Figures

List of Tables

Contents

1

Introduction

Now, more than ever, an economically efficient clean energy employment is of most importance. The continuous increase in energy demand boosted by the technological progress, the growing population on earth, the present climate crisis, and environmental degradation call for a commitment to change our way of life. The urge for both, sustainable and efficient energetic sources is a true challenge for the scientific community. The faster way to answer the aforementioned requirements is to go through the existing technological portfolio and update it. There is knowledge about the weak points, problems, and setbacks of the state-of-the-art technology. Thus, they must be explored and, hopefully, improved. In this framework, optoelectronic solutions that boost Energy Transition Technologies through stability and performance are required.

1.1 The Power of Materials Design

The 21st century brought unparalleled challenges to Materials' Science in different technological domains. Over the past years, there has been an increasing demand for the development of novel material concepts, while classical materials tend to be less requested. Thus, what if we could be able to design and develop materials with tailored properties for a specific application? Is it tailoring the pathway that materials should take? Is it even possible? Too many questions that certainly the scientific community will have answered in a couple of years.

Combining solid-state physics and chemistry, Material's Science studies the relation between the material's properties and the its composition and structure. This powerful branch of science has therefore searched the backbone of material's applicability. Before the technological integration of any material, it is essential to know its fundamental properties and understand its response to different circumstances. Hence, the development of devices that study a specific property, in a set of conditions, should be coupled with the established techniques that study the fundamental properties, in order to have a complete characterisation. Single material properties (bulk) have been studied for decades and a significant amount of research has been conducted from both the theoretical and the experimental point of view. [1]

The use of single materials can be technologically useful, but if a substantial quantity is needed, it can be critical. The raw material shortage is a reality due to the high market demand and incorrect disposal of obsolete everyday equipment. [2] The life cycle of such raw materials can be modified, even though this solution is not a long term one, and new ways to use more abundant materials or/and reduce consumption are required. Nanolaminates, a low dimensional concept created from multiple layers of two or more materials with naometric thicknesses, have been gaining momentum. [3, 4, 5, 6] This new way of creating materials offers significant improvements over the use of individual layer materials as sublayers. [7] Nanolaminates properties are highly tunable depending on the composition of each material and on the thickness of the sublayers, where the interface characteristics between those sublayers are a determinant agent. [18] Nanoscale developing tools allow for materials tailoring at an almost atomic scale, and so achieve extraordinary tunable properties. Depending on the tailored property (mechanical, thermal, optical, electrical), the applications can be diverse as sensors to energy storage materials, coatings, electronics, photovoltaic cells. [18]

Unquestionably, Photovoltaic (PV) technologies will play a key role in the energy transition. [8]. The PV generation cost is significantly linked with the power conversion efficiency value. [9] Thus, as for other renewables, PVs need additional development in order to increase their performance, to ensure scalability and to further decrease their costs. Cu(In,Ga)Se_2 (CIGS) solar cells appear, albeit with a small PV market share [10], with demonstrated laboratorial scale potential that outperforms their thin film solar cells counterparts. A major need of CIGS technologies is the development of efficient, stable, and non-toxic selective contacts. Efficient selective contacts incorporation in CIGS cells will allow for the use of an absorber layer, avoiding the use of toxic elements such as cadmium (Cd), as well as increasing its performance. CIGS devices with thickness of 490 nm have reached 15.2% [11], which is far behind that of 23.35% [12] obtained for thin film technology. Thus, further efficiency improvements in CIGS ultrathin technology will necessarily be linked to two key factors: (1) reduction of electrical and optical losses at the interfaces of the absorber layer, requiring an excellent interface passivation, and (2) an efficient selective carrier separation and extraction.

1.2 NOA at INL

The Nanofabrication and Optoelectronic Applications (NOA) group is one of 24 groups that form the International Iberian Nanotechnology Laboratory (INL). Located in Braga - Portugal, INL is a Portuguese and Spanish governments founded entity with an international legal framework. With the nanotechnological scope in mind, interdisciplinary research and diverse collaborative international and industrial projects are done on this space. The work activities are centred on six key clusters: Clean Energy, Foodture, Precise Personalised Healthtech, Smart Digital NanoSystems, Sustainable Environment, and Advanced Materials and Computing.

The NOA group, founded in 2017, is inserted on three clusters: Clean Energy, Sustainable Environment and Advanced Materials and Computing. The work done is focused on the incorporation of nanotechnology in optoelectronic devices with a strong industrial and innovation potential. Bottom-up nanofabrication and characterisation of optoelectronic materials and devices are some of the group core competences and the CIGS solar cell is a big focal point. Although, from 2021 NOA as expanded into energy storage (Project Baterias 2030), functional coating applications, and industry services/projects.

At the time of this work, NOA counted with around fifteen main elements, from Research Fellows to PhD and MsC students, but during the year it welcomes many undergraduate students in winter or summer internships. Close relations with some international and national universities and laboratories allow a grand exchange of knowledge and experience, and provides great opportunities for group members. NOA's work can be seen in various published articles, some of them being journal's cover material. For more information, the INL official website is available at `https://inl.int/` and more information about NOA can be found `https://inl.int/micro-nanofabrication/nanofabication-optoelectronic-applications/`.

1.3 Objectives

The end goal of this work is to establish a roadmap to develop customized electron selective contacts, based on multilayer systems - nanolaminates, to be implemented on optoelectronic devices. To achieve such an ambitious goal, individual layers and complex nanolaminated systems, of materials chosen based on their tabulated properties, were deposited and fully characterized in an interactive dynamic way to unveil and explore the potential of the studied nanolaminates, specifically as selective contacts.

In this work, multilayer systems based in SiO_x, SiN_x, TiO_x, ZnO_x, and HfO_x were studied, as well as their single layer counterparts, in order to be potentially integrate as selective contacts in CIGS solar cells. An in-depth fundamental study of structural, elemental composition, optical, electronic, and electrical properties was conducted.

This Thesis gives the fundamentals properties and guides the exploitation of novel nanolaminates for optimization and incorporation in final technology, following its singular challenges and demands.

1.4 Thesis Overview

This Thesis is divided in five main Chapters. Chapter 1, **Introduction**, presents the motivation that leads to the development of this work, and the defined objectives. Also, NOA and INL are presented. Chapter 2, **State-of-the-Art**, provides an introduction of nanomaterials, specifically, the nanolaminate concept is presented, described and a brief review of the possible applications is given. Regarding the nanomaterials applications in optoelectronic devices, the CIGS based solar cells are overviewed, and then, the selective contact notion is explained, followed by a discussion of the necessary requirements for such technology. A review of the implemented hole and electron

selective contacts is also given. To conclude, the chosen materials are presented, accompanied by the reasons for such choice of materials. In Chapter 3, **Experimental Details**, all the processes and techniques used are detailed. Firstly, the deposition methods are exploited, and their conditions presented. Afterwards, a description of the nanofabrication procedures and techniques used is done. The fabrication process of the devices is also shown and explained, step by step, and a list of such devices is provided. Furthermore, the characterisation techniques for structural, elemental composition, optical, electronic, and electrical properties are detailed, and the measuring conditions shown, together with the equipments used. Chapter 4, **Results and Discussion**, reveals the obtained results and data, accompanied by the corresponding discussion. It starts by presenting the structural characterisation, followed by an estimation of the samples elemental composition. Afterwards, the optical and electronic properties are studied; finally, the electrical characterisation is presented. In Chapter 5, **Conclusion**, the conclusions of this work are drawn and future work is proposed. Moreover, in the Appendix, supplementary information is provided in order to complement the results and discussion of Chapter 4.

2

State-of-the-Art

The interest in atomic scale nanomaterials boomed in 2004, when Novoselov *et al.* successfully synthesized, by scotch tape exfoliation, a monolayer of graphite, graphene, which demonstrated excellent physical and chemical properties, such as large charge carrier mobility, excellent thermal conductivity, and broadband optical absorption. [13]. Since then, many studies have been carried out to exploit materials consisting of mono- and few atomic layers and, more recently, a renewed interest in layered structures has appeared. Such material advancements have been considered the building block for the next generation of optoelectronic devices.

Before discussing results or reaching any conclusion, it is necessary to understand what is a nanolaminate, what are the benefits and possible applications, and fully grasp the notion of selective contacts. The current Chapter provides a base and presents a broad overview of published results of nanolaminates and selective contacts. Additionally, the choice of materials used in this work is discussed.

2.1 Nanomaterials

Nanomaterials have been synthesized and characterized for the past decades, due to their multifunctional properties that might differ from the bulk ones. [14] For example, when a semiconductor and a metal suffer a size reduction from bulk to a nanoparticle, a significant change in the electronic structure is observed, which, in the limit, lead to the properties of an insulator and of a semiconductor, respectively. [15] A nanomaterial can be classified as N-dimensional, being N = 0, 1, 2 (0D, 1D or 2D). Generically, a nanomaterial is N dimensional if it has 3-N nanoscale dimension(s) and N much larger dimension(s). [16] A nanoscale material, ranges from between 1-100 nm, and can be created as an individual nanostructure, or as a collection of individual nanostructures. Quantum dots, nanocrystals, or nanoparticles are examples of 0D individual nanostructures, nanowires and nanotubes of 1D, and nanosheets of 2D nanostructures. [14] The integration and development of individual or complex nanostructures tends to provide unique properties, which are in great demand for improving current technology and to designing the next nanotechnology generation.

2.2 Nanolaminates

Nanolaminates are a class of nanomaterials in which the individual nanostructure is a 2D layer with thickness ranging for one to tens of nanometres. Two or more alternate 2D layers (sublayers) can be used to build the nanolaminate system. [17] A simple two material nanolaminate system is schematically shown in Fig. 2.1. The combined sublayers A and B form a bilayer. Then, the bilayer is repeated a number of times to form the nanolaminate system. Thus, nanolaminates are fully dense nanometric multilayered combined materials, that can be designed to enhance the fundamental properties of the individual materials used as sublayers. The properties of this heterostructure layered materials can be attained through a meticulous control of layers' thickness, composition, arrangement, where the interface characteristics between sublayers are determinant. [18]

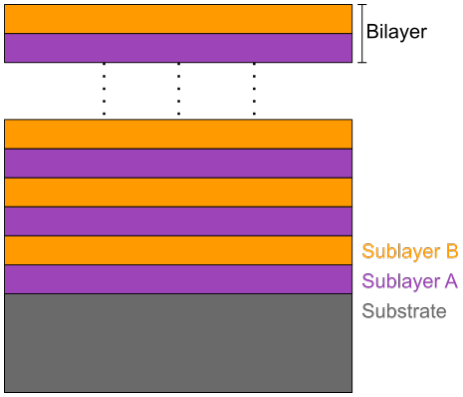

Figure 2.1: Representation of a nanolaminate system consisting of two materials, A and B.

Contrary to the bulk composites, the nanolaminates properties cannot be predicted by the rule of mixtures (weighted mean with the volume fraction). Instead, the key factors in this determination are the individual layers thickness and interfaces. [19] Therefore, when designing nanolaminates, one can estimate the final properties or the necessary individual layer's thickness to achieve a required property. This seems very simple and easy. However, in practice the material's interaction may not strictly follow that rule, especially if the layers thicknesses are tend to an atomic layer. For instance, considering polycrystalline materials, interfaces comprise less than 0.01% of volume, nevertheless, they play a critical role in properties. [20] Then, nanolaminates with a high interface/layer density should reveal significantly different properties from those of the bulk materials.

Atomic Layer Deposition (ALD) is a commonly used deposition method in the fabrication of nanolaminates, as it allows to develop them with incredibly small thicknesses and atomic precision, while still being able to coat a large area and maintaining high uniformity. ALD uses sequential self-terminating surface reactions if the chosen chemistries are adequately behaved, and allows for a wide variety of precursors. [21] For lab-scale, temporal ALD is preferable, for upscaling, spatial-ALD becomes the choice, due to its high deposition rates. [22] Although, other methods as thermal evaporation, pulsed laser deposition, magnetron sputtering, chemical vapour

deposition, electrochemical deposition, etc. can also be used. [18] Then, Chapter 3 discusses additional challenges to produce nanolamintes in more detail, and the deposition method choice.

The applicability of the nanolaminates depends greatly on material's choice, schemes used, and integration. In the remaining part of this Section several nanolaminates results with distinct applications are presented and discussed in order to show the potential of this material concept.

So far, metallic based nanolaminates were explored mostly for mechanical applications, where properties like hardness-yield strength, elastic modulus, ductility, fracture behaviour, among others are explored. Hardness is recognized as the most tailored mechanical property through nanolaminate systems. Ultra-high hardness can be obtained when the individual layer's thickness is lower than the slip-plane dislocation length value. [19] The most impacting factors on mechanical properties are the layer thickness, crystallography of each layer, combination of constituent phases, structures, and properties of interfaces and grain morphologies. [23]

Due to the complex layered structure and versatility of the design in the nanoscale or even sub-nanoscale, nanolaminates have great potential to explore nonlinear optics behaviour and be used as metamaterials. [24] Metamaterials are a well-known material class due to their unique interaction with electromagnetic waves, which may allow for a large, fast, and broadband linear (negative refractive index, hyperbolic dispersion, etc.) or nonlinear response (light modulation on the GHz range, optical gates, etc.). [25] For a simple illustration, Alloatti *et al.* showed that a ABC-type nanolaminate (A = aluminium oxide (Al_2O_3), B = titanium oxide (TiO_2), and C = hafnium oxide (HfO_2)) can be designed with 12 ALD deposition cycles and 25 trilayer repetition, to achieve second order nonlinearity, while a simpler two material nanolaminate (AB, BC, or AC) cannot. Also, if the samples are created with thinner layers or with more materials, higher order nonlinearities can be achieved. [25]

A simpler optical application of nanolaminates is transparent coatings, in energy efficient windows (Anti Reflective Coating (ARC) or infrared reflectors). One common problem with this type of coating is that a material may have the proper transparency, however, lack mechanical integrity and flexibility, or vice versa. Although, the combination of such materials on a nanolaminate structure may merge both properties. A nanolaminate system of TiO_2 and silicone (SiO_xN_y) can be designed, in different architectures, to work as: a transparent Bragg Mirror (BM) and an ARC. Three different BMs were developed in a three layer ($TiO_2/SiO_xN_y/TiO_2$), with distinct sublayers thickness values, configuration to exhibit high transmittance in a specific wavelength range (blue, green, and yellow), showing that by varying the sublayers thicknesses it is possible to achieve different characteristic. The transparent five alternative layer ARC, created on a TEC-15 glass substrate, showed a gain of 3 to 4% in transparency when compared to an uncoated TEC-15 glass. Then, when deposited on a flexible device, no cracks or deformations appeared after an extensive bending test and encapsulation capabilities were additionally obtained (harsh environment protection). [26] A similar approach was developed using Al_2O_3 and TiO_2 nanolaminate (ATO) [1] with a polymer caping layer, to provide efficient transparency, structural rigidity, passivation, and encapsulation for a red phosphorescent organic light emitting diode (OLED). [27] An ATO

[1] ATO-laminate is the most successful binary combo used in nanolaminates for electronic and super-capacitors applications.

nanolaminate was also used on a n-type silicon (Si) solar cell to protect the Al_2O_3 passivation layer from humidity, since this layer outperform when exposed to moisture. [28] Two different stacks were studied: Al_2O_3/ATO/TiO_2 and Al_2O_3/TiO_2/ATO. It was concluded that the 20 nm total thickness ATO nanolaminate, with 1.1 nm Al_2O_3 and 0.9 nm TiO_2 sublayers thickness, must be the capping layer, because it does not allow the humidity flow to the grain boundaries of the thicker TiO^2 layer below.

Besides being a part of the optoelectronic device, a nanolaminated can also be the main element. A metal oxide semiconductor light-emitting device (MOSLED) capable of providing red (613 nm) electroluminescence, although with an External Quantum Efficiency (EQE) of 5.47% and 0.14% Power Efficiency (PE), was designed with two nanolaminate systems in their structure: Al doped ZnO (AZO)/ATO/Al_2O_3-europium oxide (Eu_2O_3) nanolaminate/Si/aluminium (Al). (see Fig. 2.2) The ATO nanolaminate was introduced as a transparent and protection layer, and the Al_2O_3-Eu_2O_3 one as the main electroluminescence source due to the trivalent europium ions (Eu_{3+}). [29]

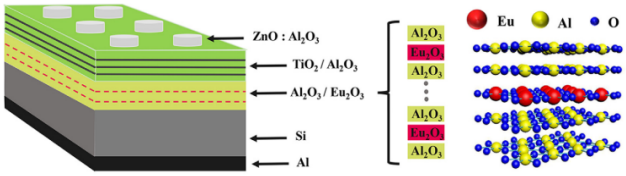

Figure 2.2: Scheme of the MOSLED structure, based on two nanolaminated systems. (From [30]).

Considering microelectronics applications, the current state-of-the-art gate transistors requires thinner and thinner high-κ (ε_r - dielectric permittivity). Although the *Ångström* range thickness can be reached, the materials start to lose dielectric properties and suffer from a diminished bandgap. The introduction of nanolaminates with morphotropic phase boundaries (MBS), zones where coexist different ferroelectric phases, can be advantageous, because near these zones it is possible to increase ε_r without degrading the bandgap (E_g) energy value. [30] Kahir *et al.* demonstrated this in a HfO_2 and zirconium oxide (ZrO_2) nanolaminate with enhanced ε_r of 64, when compared to individual layers ε_r of 25, while maintaining the around 6 eV bandgap. When there is no constraint, as the before E_g energy value, a nanolaminate system involving sublayers of two binary metal oxide with relatively low-ε_r value can suffer an exponential ε_r increase. Despite the Al_2O_3 and TiO_2 ε_r value close to 9 and 95, respectively, a 1:3 Al_2O_3/TiO_2 with sublayer's thickness values less than 0.5 nm achieve ε_r values of approximately 1000. [31]

In micro-electro-mechanical systems (MEMS), nanolaminates were also used to produce efficient micro-chip initiators that radiate and conduct heat and energy in a very rapid way. These micro-chips have a metal-interlayer-metal (MIM) configuration, in which the interlayer is a reactive multilayer film (RMF). RMFs based on Al and copper oxide (CuO) nanolaminates were intensely investigated to achieve the optimized architecture, and an initiator with faster ignition (less than 1 μs) than the typical Al film initiator (2-4 μs) and long flame duration (260 μs) was reached. [32] Also, in RMF Al and molybdenum oxide (MoO_3) nanolaminate study was found that a structure with more oxide than metal provides a more energetic reaction of 613.0 J/g, faster

ignition, highest duration of 600 μs and bigger flame area of 9.56 mm^2. [33]

Concerning solar cells application, in n- and p- type float-zone Si (fz-Si), nanolaminates have also been implemented to perform symmetrical and conductive passivation. [34] The first one passivates the solar cell front and rear side with the same material or structure, and the second one, is similar to symmetrical passivation, although the layers used are conductive, so it is not necessary to introduce contacts, because the layers act as a full area contact - this can be considered as selective contact. For symmetrical passivation, a thinner 0.60 nm layer of HfO_2 or 1.25 nm Al doped silicon oxide (Al:SiO_2) was needed to provide negligible fixed charge passivation (null density of fixed charges) when compared with a simple 1.3 nm SiO_2 layer, and the best performance was attained with a HfO_2/Al_2O_3 (1.2 nm HfO_2 interface layer) double layer with effective minority carrier lifetime above 1 ms. [34] No current density was measured in this configuration because conductivity was not a requirement. For the conductive passivation, the best balance between conductivity and passivation was a 5 nm Al_2O_3/15 nm TiO_2 double layer with a current density of about 0.5 mA/cm^2 at 10 mV and a carrier lifetime of about 20 ms. If no Al_2O_3 passivation layer was introduced in the bilayer structure (meaning a 20 nm TiO_2 layer), a carrier lifetime of 10 μs and approximate 1 mA/cm^2 current density are obtained. On the other hand, if only a 20 nm Al_2O_3 passivation layer is applied provides, 5 ms of carrier lifetime and 10^{-8} mA/cm^2 are registered. [35] Hence, it is clear that a nanolaminate system can successfully combine two desired properties, while the individual materials can only provide one of them.

The nanolaminates results presented here show the practical applicability and potential of this nanomaterial approach. However, these are a small sample of the whole picture. Most of the papers published about nanolaminates are an extensive study of the structural, mechanical, optical, and electrical properties that these materials exhibit. These papers were not referenced here, because the point of this Section was not to do a vast review but to illustrate the development and implementation of nanolaminates. Fig. 2.3 shows the evolution of published papers on this subject, there are no doubts on the growing interest in nanometric multilayer systems.

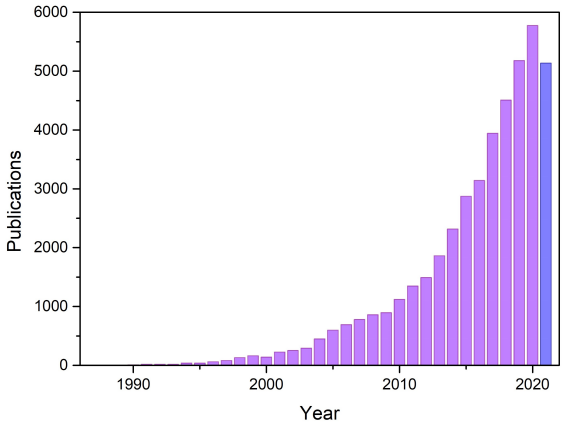

Figure 2.3: Evolution of the published papers evolving the words "nanolaminate", "heterostructure", "multilayer", "multi-layer" *OR* "multi layer(s)" *AND* "nanometric", "nanoscale", "nano scale" *OR* "nano-scale". Data obtain from Scopus website [2]and consulted on 28 September, 2021. The number of publications in 2021 (blue) is almost the same as in 2019, but it is expected that it will surpass the 2020 value.

[1]Bibliography data base at `https://www.scopus.com/home.uri`

2.3 Applications

2.3.1 CIGS Solar Cells

CIGS solar cells, are heterojunction technology inorganic thin film PV cells based on the CIGS absorber. The CIGS alloy has a I-III-VI chalcopyrite structure being the p-type component of the heterojunction technology. Due to the elements that compose the absorber, this solar cell concept exhibits excellent optoelectronic properties: tunable direct bandgap with energy values in a range of 1.02$\sim$1.67 eV, high absorption coefficient value ($>1\times10^5$ cm^{-1}), 3D symmetric carrier transport, and excellent thermodynamic stability. [36]

The current state-of-the-art of CIGS based solar cells architecture is typically made up of a substrate and five layers. First, the absorber is grown on a metallic contact, usually a molybdenum (Mo) coated Soda Lime Glass (SLG) substrate, and this can be done in a wide variety of methods, which may be classified in three main categories: (1) co-evaporation, (2) selenization of vacuum deposited metallic precursors, and (3) non-vacuum techniques. [37] Then, since the CIGS subtract acts as a p-type semiconductor, it is necessary to add at the top of it a n-type layer that completes the heterojunction. Thus, following the CIGS growth, a chemical bath deposition of cadmium sulphide (CdS) is performed. For the solar cell to be complete and display high efficiency, an intrinsic zinc oxide (i-ZnO) and a AZO layers are added to form a Transparent Conductive Oxide (TCO), to function as an optical window. [38] A scheme of a CIGS solar cell structure is presented in Figure 2.4.

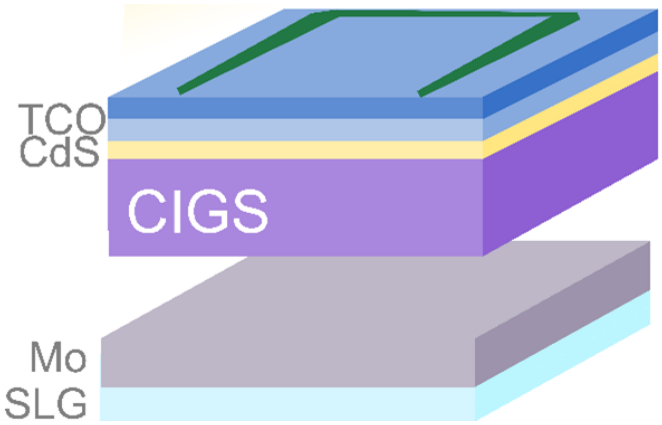

Figure 2.4: Schematic representation of a CIGS solar cell, where the different layers are distinct. Also, it is possible to observe the ”U” shaped front contact.

Across the years, this technology has attracted the research community's attention due to its appealing properties and industrial applicability. Therefore, many advances have been made, mostly focused on improving the CIGS layer, through compositional adjustments and doping. [39, 40, 41, 42, 43] Nevertheless, the CIGS based solar cells architecture has not changed since the 80s and several improvements can be employed. [44] At the present date, a 23.35% highest efficiency value for a thin CIGS solar cell was reported and with no CdS layers, which is a problematic component due to the Cd toxicity. [12]

Hence, the main focus can be redirected to improve the architecture and replace problematic sections, such as the CdS and Mo layers where the latter is a poor reflector. One path to alter these solar cells, is to develop ultra-thin devices (thickness below 500 μm) that may allow flexibility and consume less raw materials. [45] Although with promising results, there are critical points in ultrathin cells: (1) it requires excellent optical management due to the smaller optical path length and (2) the interface recombination becomes a major loss mechanism. [46, 47] To deal with light management different strategies can be taken [46] and the common way to prevent recombination is to introduce a passivation layer between the contact and the absorber. [47, 48, 49, 50, 51] Despite beneficial, these solutions are not sufficient, in the way that they do not solve, for example, the CdS and Mo problem. It is required to start from scratch and develop a contact that provides passivation and carrier extraction - Selective Contact.

2.3.2 Selective Contacts

Selective contacts, also known as heterocontacts or passivating contacts, are structures that provide passivation and, at the same time, operate as contacts for excellent carrier extraction. [52]

Designing a contact with excellent carrier extraction is not trivial. The selective contact cannot just have high conductivity for both charge carries. An asymmetry that allows for one carrier type to pass while the other is blocked leading to charge separation, is necessary. This is called Selectivity. Thus, an electron selective contact must allow the transport of electrons (majority charge carriers), while block the holes (minority charge carriers), and vice versa for the hole selective contact.[3] Moreover, there are several other properties that a selective contact should present to be integrated in an efficient solar cell, naming: passivation, adequate optical constant, low-contact resistance, chemical stability, diffusion barriers, among other specific properties.

Selectivity is accomplished through a suitable band alignment, as depicted in Fig. 2.5. In a selective contact, the offset between the majority carrier band (conduction band for electrons and valence band for hole) and the respective device band should be minor so that they have high conductivity; while for the minority carriers the band offset should be large enough to work as a barrier and block its transport. [53] To achieve the required band offsets, two main type of materials can be used: high bandgap materials with asymmetric band off-set or high and low work function materials. [54]

[3] Note that the terms majority or minority charge carriers refers to the carriers in and at the vicinity of the contact, not in the whole optoelectronic device.

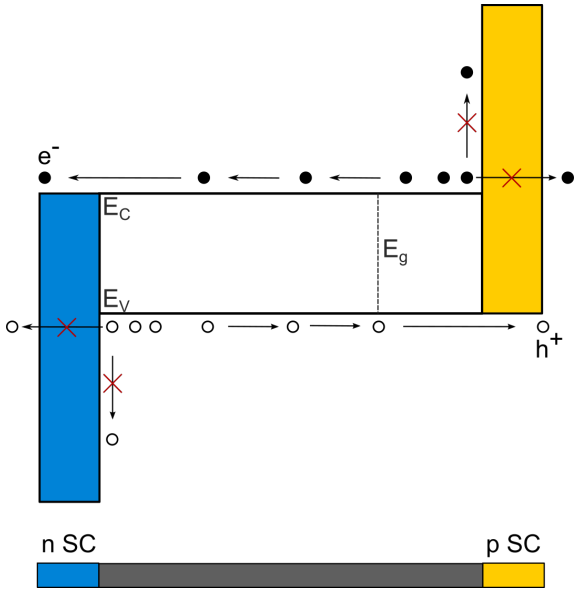

Figure 2.5: Band diagram representation of a flat band optoelectronic device with and electron (n) and hole (p) selective contact (SC). The conduction (E_C) and valence (E_V) band and respective difference, the bandgap (E_g), are represented. Majority charge carriers can be transported in the, respective, selective contact, while the minority charge transport is blocked, no matter what type of transport. The contacts thickness is sufficient to do not allow tunnelling.

Passivation, minimization of the recombination losses, is implemented on solar cells by the introduction of a passivation dielectric layer between the absorber and the contact. Although beneficial, these nonconductive layers add complexity since local contacts are required. [53] Passivation can be accomplished by two ways: (1) chemical passivation or (2) field-effect passivation. Dielectric materials usually provide both types of passivation. Chemical passivation reduces the active recombination centers, leading to a low value of active trap density (D_{it}). Field-effect passivation diffuses the minority charge carriers and alters the electron and hole concentration at the surface through intrinsic fixed charges in the dielectric layer. The impact of this type of passivation can be quantified with the density of fixed charges (Q_f). Thus, to design a selective contact three main requirements are imposed: (1) Passivation, (2) Conductivity, and (3) Selectivity. Although they may seem independent from one another, they are not. *Onno et al.* showed, by PC1D simulations [4], that passivation and conductivity are necessary and sufficient (because implies selectivity) in a full area contact for a solar cell, but the reciprocal it is not true, a selective contact can have selectivity but can lack passivation or conductivity. [55] So, selectivity is necessary, but not sufficient for high efficiency solar cells.

The applications of selective contacts are many and diverse. Although, at the current time most of the applications and published results are in Si solar cells. Fig. 2.6 presents a graphical view of the band alignment of some selective contact candidates, several of the described in the following subsections. The remaining part of this Section serves as two small reviews of some of the existent electron and hole selective contacts.

[4] One-dimensional semiconductor device (PC1D) simulator is the most commonly used and regarded as the industry standard for photovoltaic simulations.

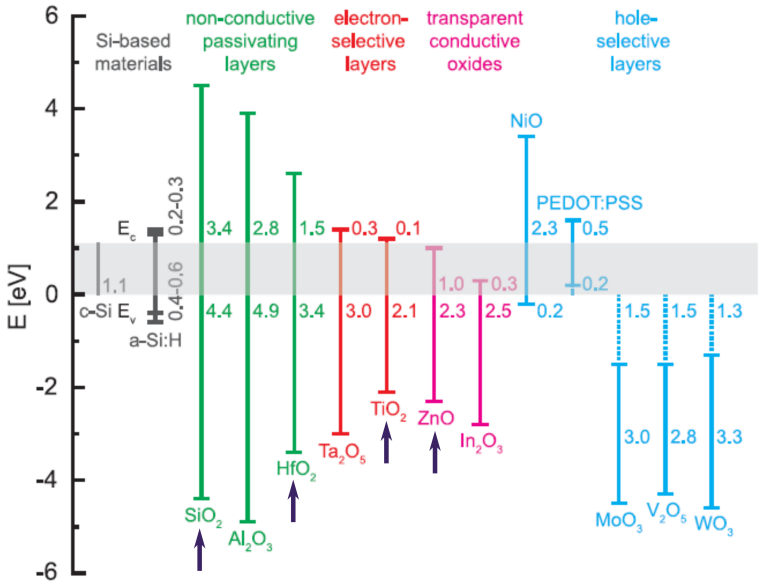

Figure 2.6: Band offsets graphical representation of various materials in respect to c-Si. Depending on the offset value, the materials can be divided in different categories with distinct applicabilities. Note that these values are only representative, since the actual values have many dependences and need to be accurately determined. [55]

The research on organic solar cells has provided to the PV technology a considerable knowledge on carrier selective materials. Hybrid solar cells combining organic hole transport layer such as PEDOT:PSS with crystalline Si (c-Si) absorber has generated promising results but air and ultraviolet stability of the selective layers remain, even now, a major concern. [56] Another kind of materials that have been extensively explored as efficient carrier selectivity in solar cells were the Transmission Metal Oxide (TMO), which combine an extensive range of electron affinity, a high work function, high transparency and a semiconductive behaviour (n- or p-type) determined by susceptibility in their stoichiometry. [57] Since TMOs are more stable than their organic counterparts, and due to it aforementioned features, these oxides have been explored to be incorporated in silicon heterojunction (SHJ) architecture.

Perovskite solar cells are one of the more recent driving forces in the development of selective contacts, since they require two charge carriers transport layers in their structure. [58] These layers commonly referenced as hole and electron transport layers (HTL and ETLS, respectively), are mandatory to exist in the perovskite solar cells, since their efficiency is based on the charge selectivity of such layers. [59] Common HTL can be formed with organic (molecular, polymeric and organometallic complexes) or inorganic (as TMOs and halides) compounds, while ETL are build with organic, inorganic or composite materials. [60] The most employed inorganic ETL is the TiO_2 material, in the compact and mesoporous form, although ZnO as emerged has an excellent TiO_2 replace due to the good transparency. [59] Moreover, recently tin oxide (SnO_2) has arisen as new and better ETL, because of its attractive optical and electronic properties, and its introduction bring the perovskite solar cells efficiency close to the Shockley-Queisser limit. [58] Nevertheless, improvements at the interface and HTL level are still mandatory. [60]

Hole Selective Contacts

One of the most investigated TMO for hole selectivity is MoO_x. The introduction of a 4 nm MoO_x layer on a SHJ solar cell, achieves a 23.5% efficiency and 81.8% Fill Factor (FF), higher than the reference (values not mentioned). It is stated that this thin layer protects the underlying intrinsic hydrogenated amorphous Si layer ((i)a-Si:H), used for passivation, from sputtering damage, provide the solar cell better transparency, and enhances its performance via high selectivity and good charge carrier transport. [61]

Tungsten and vanadium oxide (WO_3 and V_2O_5) have also been investigated as hole selective contacts and directly compared with MoO_x. All three TMOs have the correct electronic, structural, and optical properties, to work as a front hole selective contact for a n-type Si solar cell and show a substantial EQE improvement in 300 to 600 nm range. The solar cells with a 15 nm V_2O_5 layer achieved a Power Conversion Efficiency (PCE) value of 15.7%, followed by MoO_x with 13.6% and WO_x 12.5%. [62] Besides good results and relative high efficiency, the reference heterojunction device with a-Si:H emitter performance was not surpassed (18.3% PCE). When studied alone on n-type solar cells, it is concluded that a V_2O_5 contact is superior to the MoO_x one, the superior performance is justified by the open circuit voltage (V_{oc}) enhancement, from 563 mV to 662 mV, as the V_2O_5 layer provides better passivation on flat than random texturized solar cells. [63]

Anther TMO often used in optoelectronic devices is copper oxide (CuO or Cu_2O). This material has no toxic element, high chemical stability, abundant reserves, and is also a good candidate for a hole selective contact. A 10 nm Cu_2O layer and a 10 nm boron doped Cu_2O layer (B:Cu_2O) were introduced in a c-Si solar cell. The boron doping improved the film transparency, hole density, and conductivity, but a decrease in the hole mobility was observed. To prevent Cu diffusion into the silicon cell, a thin SiO_x was introduced. The current density, V_{oc} (114 mV, 290 mV and 370 mV), FF (29.2%, 40.1% and 40.6%) and efficiency (0.64%, 3.9% and 5.48%) values for the Cu_2O/Si, B:Cu_2O/Si and B:Cu_2O/SiO_x/Si, respectively, prove that the B:Cu_2O layer provides the required selectivity but may be missing passivation. [57]

TCOs, like indium-tin-oxide (ITO) and AZO, that provide high optical transparency and good electrical conductivity, have also been studied for selective contacts. One of those TCOs is nickel oxide (NiO) which is a p-type material with hole selective contact potential. A 30 nm NiO layer introduced on a Si solar cell showed a 77.87% average transmittance in the 300 to 1100 nm range, much lower leakage current than the ITO and AZO cases (proving a good replacement) and a 17.37% efficiency (almost double than without a layer - 6.73%). [64]

Electron Selective Contacts

Almost all selective contacts achieve optimum performance due to the band bending induce by the material's high or low work function. One selective contact developing approach used a thin passivation layer with a low work function metal. Simulation results show that a thin layer of SiO_x, used to passivate the n-type Si solar cell with additional hole blocking capabilities due the high E_g, and a low work function metals (3.7-4.3 eV) can reduce the contact resistivity and the effective

barrier height. Additionally, if a MoO_x layer is added a theoretically 21.8% efficiency can be achieved. [65] The SiO_x layer may have some selective contact qualities, nevertheless they are not optimum. Hence, in the before SiO_x and a low work function architecture, a layer with the correct selective contact electronic structure must be added. Various complex structures of (i)a-Si:H, SiO_x, SnO_2 and low work function metal were investigated. The best performance of 18.35%, when compared with the lowest 15.53%, was achieved with the (i)a-Si:H/SiO_x/SnO_2/magnesium (Mg) in which the first two layers provide passivation and the remaining selectivity, while low contact resistivity when compared with other results. Moreover, with the increase of the metal work function the efficiency is degraded. [66]

A selective contact constituted by magnesium fluoride (MgF_2) and Al layers was proven, reaching a 20.1% efficiency and low contact resistance on n-type Si solar cell. Although, it was necessary to add an (i)a-Si:H layer between the Si and the MgF_2 due to poor passivation performance (only 15 μs of minority carrier lifetime). [67] With a similar configuration, a TiO_2 can function as an electron or hole selective contact depending on the deposition process and final contact. [68] The selective contacts development done on Si solar cells can also be done on other types of solar cells like CIGS. For example, on indium phosphide (InP) solar cell a simple 8 nm tantalum oxide (Ta_2O_5) layer can enhance the PCE from 9.4% to 19.1% due to the favourable band offsets.

Almost all the results presented lack passivation when only the selective layer is added, so it was essential to add a layer capable to do so (typically SiO_x or (i)a-Si:H). This layer is essential because, as said before, a good selective contact must provide passivation, conductivity, and selectivity. Without one of them, a maximized efficiency cannot be reached. Thus, the search for a combination of materials that provides all the required properties is still ongoing.

2.4 Materials Choice

From the discussion presented beforehand, it is possible to acknowledge that the materials combination is key to achieve the desire goal. So, the choice must be pondered and always be based on the required properties.

Different cations involving elemental transition metals, post-transition metals, and metalloids: hafnium (Hf), zinc (Zn), titanium (Ti), and Si were used in this work, and considered by the wide-ranging set of features, mostly due to the massive diversity of compositions and structures they may adopt. Their simplicity of binary matrix, compositional and structural diversity, offer flexibility to tailor desirable fundamental properties, while presenting a high chemical and thermal stability with excellent mechanical and optical properties. Binary oxides can mostly be divided into two categories: dielectrics (Al, Ti, zirconium (Zr), Hf, niobium (Nb), Vb oxides, etc.) and conductors/semiconductors (gallium (Ga), Zn, indium (In), W, Ni oxides, etc.). [18] Several of these oxides are TMOs or TCOs, which are implemented in many portions of optoelectronic devices, or high-ε_r materials [69] used in microelectronics applications, additionally, in solar cells, chemical and biochemical sensors, reflective and protective coatings, among many others.

So, the materials used to develop the selective contacts based on nanolaminates were the fol-

lowing: SiO_x, silicon nitride (SiN_x), zinc oxide (ZnO_x), TiO_2 and HfO_x.[5] The first two were combined in binary nanolaminates and the remaining three also, with TiO_2 the common material. This means that in this work were created SiO_x - SiN_x, ZnO_x - TiO_2, and HfO_x - TiO_x nanolaminates. The first set was design since both materials are great passivators and due to high bandgap value the nanolaminate may block holes while providing electron conductivity. In the second set, both materials have an electron selective contact correct band offsets for Si, and possibly CIGS, and relative high conductivity; the latter set was design as a intermediate of the first two, a material with good passivation performance and one with the correct band structure and good conductivity.

SiO_x is an extensively used materials on the microelectronics area, but it also applied in optoelectronics devices as passivation layer in Si and CIGS solar cell [70] and ARC [71]. SiN_x is the only non-binary oxide material used in this work, but it is often used in Si-based technology [72, 73] and, similar to SiO_x, can be applied to passivate [74] and on optical management strategies [71]. ZnO_x is a n-type semiconductor and TCO with selective contact suitable band alignment [53], used as contacts [75] for devices or optical windows [76], including CIGS solar cells. TiO_x is a TMO already integrated in nanolaminate structures, as seen before, and has the potential as a selective contact in Si solar cells [77]. To finalize, HfO_x is a high-ε_r dielectric and TMO with passivation capabilities [78, 79], already employed on CIGS solar cells, and a possible replacement for SiO_2 [80].

[5] Note that the established stoichiometric form of this compounds was not used because it was determined at the beginning of this work, and it will be present in Chapter 4.

3

Experimental Details

Deposition processes and characterisation techniques are of great importance in the pathway to design new materials, mainly if multilayer systems down to a nanometric scale are considered. It is indispensable to understand and crosslink, the mechanisms and fundamentals behind the production of individual layers and their multilayers counterparts. Hence, a ”small” parameter can have a big impact on the final result, and not be so ”small” after all. Thus, advanced characterisation continuous feedback is essential to study and comprehend the physics occurring in this novel materials approach.

In this Chapter, individual layers and nanolaminate systems deposition methods, and homemade devices fabrication process, are generically presented. Characterisation techniques used to assess the morphological, structural, optical, and electrical properties of the studied samples, are briefly discussed according to the requirements of the carried study. The following deposition methods, fabrication procedures, and characterisation techniques were employed through equipment available at INL, except the XRD analysis, which was carried out at the Trace Analysis and Imaging Laboratory (TAIL) in the Physics Department of University of Coimbra.

3.1 Cleaning

To ensure that no properties are altered a substrate cleaning procedure is performed before starting deposition or fabrication processes. The substrate is rinsed with acetone and then placed on an ultrasounds acetone bath for 10 min. After that, it is again rinsed with acetone and dried with a nitrogen (N) gun. The above steps are repeated two more times, with an isopropanol and a deionized water solution. Additionally, the deposition chambers are also purged/cleaned before each deposition, to prevent contaminations.

3.2 Deposition

A significant number of nanometric multilayer systems were deposited in this work, based on the material's choice discussed in Section 2.4: SiO_x, SiN_x, ZnO_x, TiO_x and HfO_x. Nanolaminates systems are commonly fabricated by bottom-up methods and mostly by ALD. Despite being an extremely attractive approach to create (sub-)nanometric multilayers systems, ALD is mainly a lab-scale methodology, so to develop nanolaminates systems compatible with rapid integration into existing PV technologies on the market, two industry ready bottom-up methods were used: Plasma Enhanced Chemical Vapour Deposition (PECVD) and Magnetron Sputtering.

Regardless, PECVD and Magnetron Sputtering being based on chemical and physical reactions, respectively, both techniques deposit the film by a vapour deposition process. Although, the synthesis process of such vapour is very distinct. As with any technique or method, advantages and disadvantages exist. PECVD is the most used deposition process in the semiconductor industry, is versatile while being able to maintain control, but the reaction by-products are toxic. Magnetron Sputtering can be applied to almost any material (metals, alloys, ceramics, polymers, and dielectrics), while maintaining chemical composition, but the deposition can be time consuming. [81] Besides the disadvantages mentioned, both these processes allow to develop films with relatively high density, conformal, low impurities and keep paramount properties to carry out in sub-nanometric multilayer systems. [82] Applications of these methods can range from electronics, photovoltaic devices, and sensors to energy [18], indicating that PECVD and Magnetron Sputtering are well established in the industrial world and can be used to produce a new technology based on nanolaminates if such is provided.

Developing bulks (individual layers) is as important as nanolaminates. Previously to study and comprehend the properties and interaction between the different materials layers, it is necessary to characterize the bulks and establish their standalone properties. Thus, the nanolaminate systems development must be complemented by SiO_x, SiN_x, ZnO_x, TiO_x and HfO_x individual layers deposition.

3.2.1 Plasma Enhanced Chemical Vapour Deposition

PECVD is a common version of the Chemical Vapour Deposition (CVD) process class, in which the working principle is identical for all versions. CVD uses a chemical reaction in a gas phase to form a film. By introducing two or more volatile gases in a chamber and driving them to chemically react, the desired solid compound is created and deposited onto the substrate. To keep a constant pressure during the process and induce the required reactions, an inert gas, typically argon (Ar), is constantly pumped into the chamber.

The simpler approach to induce the chemical reaction is to provide thermal energy by increasing the chamber temperature, typically form 300-500 °C. However, this approach is not always viable. The substrate or some compound in it may not survive such a high temperature. Here lays PECVD advantage. Instead of using thermal energy, in a parallel plate's configuration PECVD the required activation energy is provided through plasma. By applying a high voltage (typically

a Radio Frequency (RF) power supply a with working frequency equal to 13.56 MHz) between the plates, the gases form a plasma through high energy collisions, and the chemical reaction is initiated. Fig.3.1 shows a schematic of the PECVD deposition process.

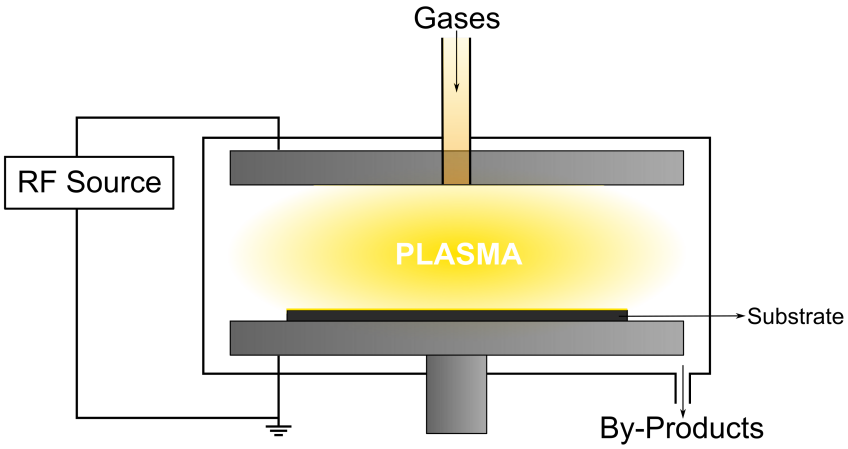

Figure 3.1: Schematic configuration of a PECVD and the corresponding chemical reaction that occurs inside the camber.

The PECVD method was used to deposit the SiO_x and SiN_x thin films. The equipment used was a MPX CVD manufactured by SPTS Technologies, and works with the conditions presented in Table 3.1. To deposit SiO_x, the precursor's gases were silane (SiH_4), and nitrous oxide (N_2O), while for SiN_x, SiH_4 and ammonia (NH_3) were used. The deposition rates used are listed in the equipment and frequently calibrated by the PECVD responsible team.

Table 3.1: Silicon oxide and nitride PECVD deposition conditions used in this work. The deposition temperature was around 300 ° C.

Material	Power (W)	1st Gas Flow (scm)	2nd Gas Flow (scm)	N_2 Flow (scm)	Deposition Rate (nm/min)
SiO_x	30	N_2O 1420	SiH_4 10	392	46.36
SiN_x	30	NH_3 55	SiH_4 40	1960	11.15

3.2.2 Magnetron Sputtering

Sputtering is a high vacuum and low temperature process, classified as a Physical Vapour Deposition (PVD). In this technique, material atoms or clusters are ejected ("sputtered") by high-energy inert atoms (usually Ar gas) from a high purity solid target (over 99%) towards the substrate by means of a direct current (DC) or RF plasma. [83]

In a parallel-plate system, the target is connected to the negative and the substrate to the positive electrode of a power source, as schematically shown in Fig. 3.2, to create a high electrical field. This electrical field ionizes Ar atoms present in the chamber, and accelerates them to the target. The collision of such ions with the target ejects the material's neutral atoms or clusters with the same chemical composition, and redirects them to the substrate, where the deposition occurs.

[81] The power source is typically DC for metals and RF for dielectrics. To improve the process, magnets are added near the target, to magnetically confine the high energy ions close to the target surfaces (magnetron sputtering). The substrate may also be spinning or moving side to side at a constant speed to achieve a homogeneous deposition. A representation of such sputtering version with magnets (Magnetron Sputtering) is also shown in Fig. 3.2.

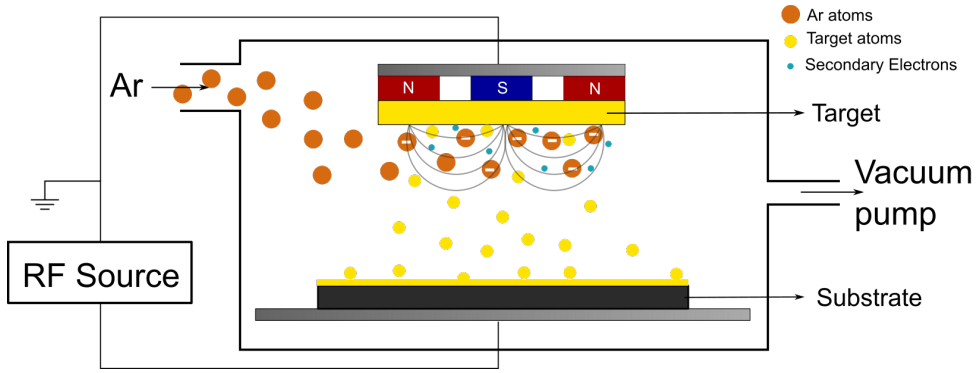

Figure 3.2: Configuration example of a RF sputtering equipment and graphic representation of the physical process occurring in a sputtering equipment.

Magnetron Sputtering was used to deposit ZnO_x, TiO_x and HfO_x. Moreover, electrical contacts of Aluminum-Silicon-Copper (AlSiCu with approximately 1% Cu, 5% Si and 94% Al), used in home-made devices, were also produced by this method. ZnO_x, TiO_x and HfO_x were deposited in a Multi-target UHV Sputtering System manufactured by Kenosistec and the contacts were deposited in a Timaris FTM by Singulus Technologies. The deposition conditions are presented in Table 3.2. The oxides deposition rates had to be assessed, because the ones listed on the equipment were calibrated for thicker depositions and big deviations were experienced in the first depositions attempts. To do a calibration for thin films, a deposition with a specific duration is made on a Si substrate with several parallel permanent ink lines. After the deposition, an acetone cleaning is done to remove the ink and the material deposited on top of it. The ink acts as a protective ”layer”, not allowing the material-substrate adhesion. The acetone cleaning exposes the Si substrate creating the zero reference. Then, a contact profilometer measurement is executed to determine the film thickness. To finalize, the measured thickness is divided by the deposition duration.

Table 3.2: ZnO_x, TiO_x, HfO_x, and AlSiCu Magnetron Sputtering conditions. The AlSiCu depostiton rate has different units because the stage is moving relative to the target during the deposition. This deposition rate is called Dynamic, in contrast to the others called Static, and reflects thickness deposited times the movement velocity. The stage velocity on the Kenosistec is 10 rpm (spining motion) and on the FTM is determined by the required thickness (linear motion).

Material	Target Size	Source	Power (W)	Ar Flow (scm)	Deposition Rate (nm/min)	Temperature (° C)
ZnO_x	2 *in* radius	RF	60	20	0.439	RT
TiO_x	2 *in* radius	RF	60	20	0.137	RT
HfO_x	2 *in* radius	RF	100	40	2.080	RT
AlSiCu	420x110 mm_2	DC	2250	200	632 nm·mm/s	Over 100

Table 3.3 summarizes the fabrication process of the studied monolayers and nanolaminate systems. It is divided by samples set, the corresponding deposition method and architecture characteristics are presented. Onward, any nanolaminate systems is referenced as sample ”SSxx”, in which ”SS” is the set, ”xx” the sample number. For easy remembering, the sets names are the materials combine initials in the corresponding order and the sample's number unit part corresponds to the bilayer repetition (0 to individual layers, 1 to two layers, 2 to four layers systems, etc.) and the decimal part, if existing, is the samples identification inside that set and specific bilayer repetition. If the number is an integer, no similar system exists in that set.

Table 3.3: Nominal characteristics of the nanolaminate systems developed in this work. Sets TZ and ZT are different due to the inverse sublayer orientation.

Set	Material	Deposition Method	Substrate cm_2	Sample Number	Bilayer Repetition	First Sublayer Thickness (nm)	Second Sublayer Thickness (nm)	Total Nominal Thickness (nm)	Deposition Time (min)	**Sample Name**
SS	SiO_x and SiN_x	PECVD	2.5 x 2.5 Si	0.1	0	100	0	100	2.16	**SS0.1**
				0.2	0	0	100	100	8.97	**SS0.2**
				5.1	5	1	2	15	1.00	**SS5.1**
				5.2	5	2	1	15	0.66	**SS5.2**
				5.3	5	1	3	20	1.45	**SS5.3**
				5.4	5	3	1	20	0.77	**SS5.4**
				10.1	10	1	1	20	1.11	**SS10.1**
				10.2	10	2	2	40	2.26	**SS10.2**
				10.3	10	1	2	30	2.01	**SS10.3**
				10.4	10	2	1	30	1.33	**SS10.4**
TZ	TiO_x and ZnO_x	Magnetron Sputtering	2.5 x 2.5 Si and SLG	0.1	0	30	0	30	218.54	**TZ0.1**
				0.2	0	0	30	30	68.29	**TZ0.2**
				1.1	1	15	15	30	143.42	**TZ1.1**
				1.2	1	20	10	30	168.46	**TZ1.2**
				2	2	10	5	30		**TZ2**
				3	3	8	2	30	188.49	**TZ3**
ZT	ZnO_x and TiO_x			1.1	1	15	15	30	143.42	**ZT1.1**
				1.2	1	10	20	30	168.46	**ZT1.2**
				2	2	5	10	30		**ZT2**
				3	3	2	8	30	188.49	**ZT3**
HT	HfO_x and TiO_x			0	0	100	0	100	14	**HT0**
				1	1	10	20	30	150.10	**HT1**
				2	2	5	10	30		**HT2**

3.3 Devices Fabrication

Two types of devices were developed during this work, capacitors and Transfer Length Method (TLM) devices, whereas the latter one were produced with two different architectures and fabrication approaches. In the following Sub-sections will be presented the fabrication techniques description used in the device's fabrication, following the natural flow order of the fabrication process.

3.3.1 Process Flow

The development and fabrication of home-made devices requires various critical physical and chemical processes, as schematically shown in Fig. 3.3. In this work, at a first stage, two sets of shadow masks were fabricated (Fig. 3.3 (1) frame like and (2) line-pattern). The shadow masks were used in all developed devices, as a physical barrier between deposited material and the substrate, allowing for patterning the deposited film with the mask design. As previously pointed in Section 3.1, all processes started by the cleaning procedure of the substrates.

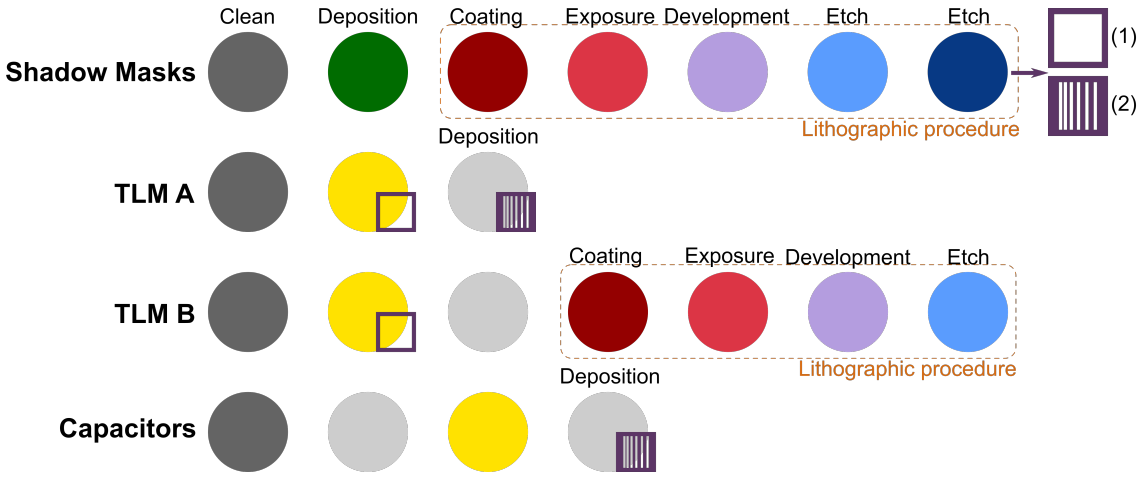

Figure 3.3: Flow chart of each device fabricated. The steps are identified at the top and have different colours to allow differentiation. In the deposition steps, the colour green represents the deposition of SiO_x, yellow of the sample (individual layer or nanolaminate system) and light gray the AlSiCu layer or contacts. When a shadow mask is used in these depositions, the schematic of it appears next to the step circle. Regarding the etch step, light blue for APS etch and dark blue for Pegasus etch are presented).

The fabricated devices process[1] , which is described in Fig. 3.3 is summarized as:

• **Shadow masks:** Si substrate was coated with 3 μm SiO_x, followed by a projection lithographic procedure and adequate etching, detailed discussed in the following Sub-sections.

• **TLM A Devices:** individual or nanolaminate systems were deposited using the frame-like shadow mask on Si substrates, then 400 nm of AlSiCu contacts were deposited by using the line-pattern shadow mask (Fig. 3.4 (a)).

[1]Note that all the deposition details followed the conditions discussed in the former Section.

• **TLM B devices:** individual or nanolaminate systems were deposited on a Si substrate, then using the frame-like shadow mask a 400 nm AlSiCu thick layer was deposited. Thereafter, lithographic and etch procedures were followed, as well discussed in the upcoming Sub-sections (Fig. 3.4 (b)).

• **Capacitors:** 400 nm of AlSiCu were deposited on a Si substrate, followed by the individual or nanolaminates systems, finally the top contact of 400 nm of AlSiCu were deposited using the line and circular pattern shadow mask (Fig. 3.4 (c)). The circular pattern hard mask used was fabricated by NOA, although not as part of this work.

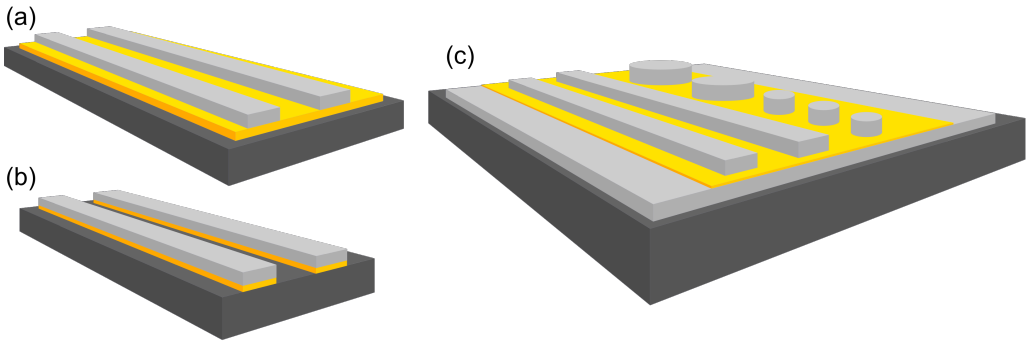

Figure 3.4: 3D representation of the devices fabricated: (a) TLM A, (B) TLM B, and (c) Capacitor. The yellow layers represent the sample, the light grey structure the AlSiCu contacts, and the dark grey layer the substrate (Si or SLG).

3.3.2 Lithography

Lithography is a very powerful procedure that allows the production of 1D, 2D, and 3D patterns in the most diverse materials. With the right conditions and steps, very complex structures can be achieved. Fig. 3.5 exhibits a Scanning Electron Microscopy (SEM) top image of a sub-micrometre line contact pattern performed by NOA, using a maskless Direct Write Lithography (DWL).

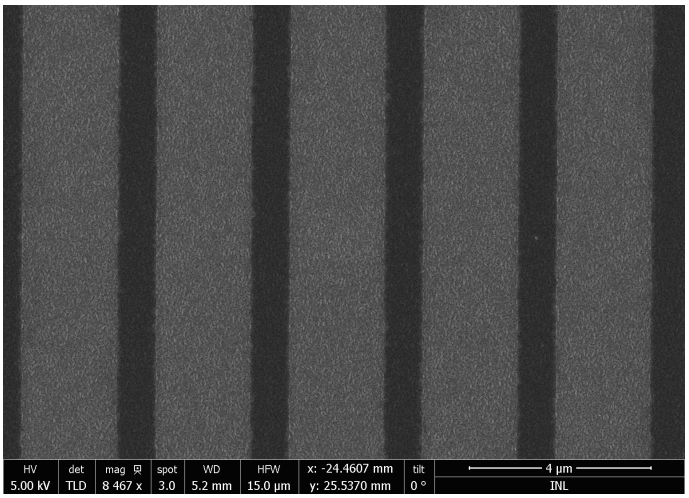

Figure 3.5: Top view SEM image of high-performance substrates for thin film solar cells. The Mo (dark regions) substrate has 20 nm thick SiO_2 (clear regions) lines with 700 nm of width and 2800 nm of pitch, nominal values.

Just like other methods discussed in this Chapter, the term lithography is very vague in the sense that describes a class. Lithography can be performed with a physical mask designed with the desired pattern or even maskless in which a narrow light beam is illuminated upon the sample. In this work, a maskless photolithography process was used to fabricate the shadow mask set and directly TLM devices for the electric measurements discussed in Subsection 3.4.5. As the name suggests, this lithography method uses light with a specific wavelength to pattern complex structures. This may seem simple, but it requires many steps that need to occur in sequence as schematically summarized in Fig. 3.6, where the very first step, creation of a layout, is leaft out. This section is meant to do a step-by-step overview of the whole process: layout, coating, exposure, development, and etch.

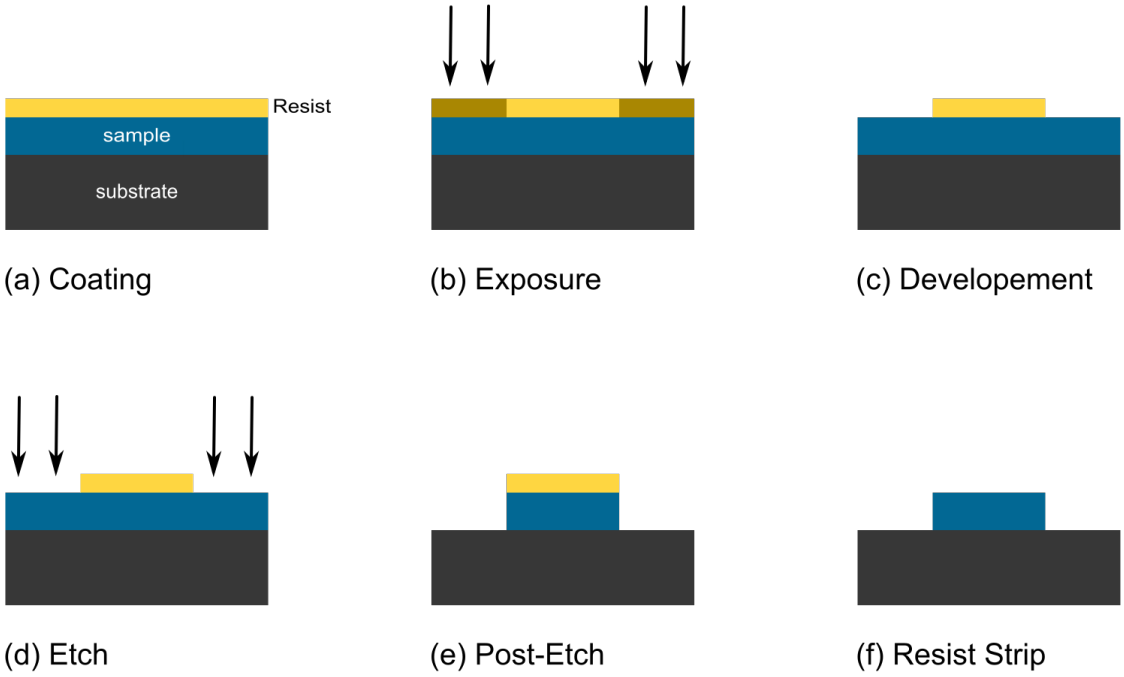

Figure 3.6: A simple lithography process in which a thin film layer is patterned. The process steps are individually represented from (a) to (f).

Layout

The starting point is to create a layout. Firstly, a mask is designed using technical drawing AutoCAD software. Once designed, masks shall be converted and transferred into the DWL equipment's computer.

Two sets of different hard masks (Fig. 3.7 (a) frame like and (b) line-pattern) had to be created to achieve the architecture required by the TLM (see Section 3.4.5): no gap between the contact's edge and sample layer edge must exist on the top or bottom (δ = 0). This is very difficult to achieve if we deposit the entire area of the substrate with the sample, since the hard mask cannot be bigger than the substrate (in area terms) due to fixation problems. So, to ensure no gap, we use a frame like shadow mask to deposit the sample on a smaller area of 20 000 x 20 000 μm^2. The line-pattern hard masks were designed with the following requirements: (1) the contact's

height must be equal to the frame like opening (20 000 μm), (2) the contact's width should be big enough to provide a good contact with the available equipment, and (3) the contact's separation must be bigger big enough to prevent the creation of short circuits during the deposition, and avoid fabrications problems.

Therefore, 4 frame like and 4 line-pattern with different contacts width were created. The shadow masks dimensions are summarized on Table 3.4 and the AutoCAD designs can be seen in Appendix A, Fig. A.1.

Table 3.4: Fabricated shadow mask dimensions. The contact's spacings increase by 200 μm steps

Mask	Height (μm)	Width (μm)	Number of Contacts	Spacings (μm)
Frame Like	20 000	20 000	-	-
Line-Pattern A		1000	10	200 to 1800
Line-Pattern B		1500	8	200 to 1400
Line-Pattern C		2000	7	200 to 1200
Line-Pattern D		2500	6	200 to 1000

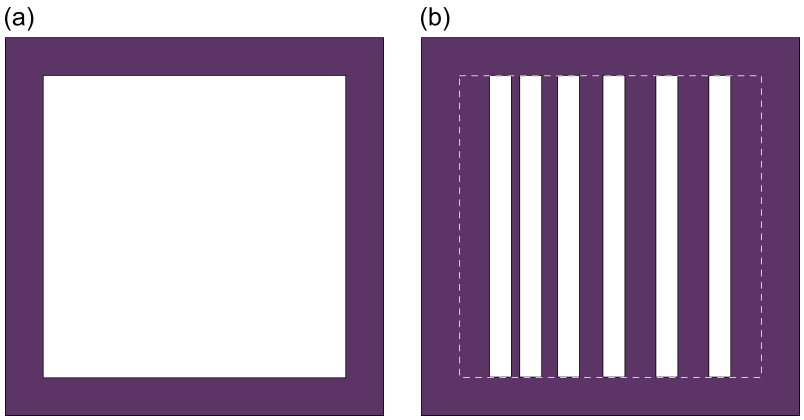

Figure 3.7: Schematic of the fabricated hard masks: (a) frame like and (b) line-pattern. Note that in (b) the contacts are centred. The dashed line represents the frame like mask opening.

Coating

The first experimental step is to coat the sample with a photoactive material that allows patterning. This specific material is called Photoresist and a large selection of it exists depending on the fabrication requirements. Most photoresist formulations consist of three main components: a photosensitive material, film matrix resin, and a solvent. Although, two main classes of photoresist are available: positive and negative. In the present work, it was used a positive resist, so exposed areas will become soluble in the development stage.

For both lithographic procedures executed in shadow masks and TLM B fabrication process (Fig. 3.3), it was used a Gamma Cluster optical track engineered by SÜSS MicroTec for the photoresist spin-coating deposition. The substrates were coated with a 1035 μm uniform layer of positive resist AZ1505 and then placed on a hot plate at 100 ° C for 50 s. This heating step is called soft bake and is used to evaporate the resist's solvent (the coating is done with diluted resit)

and cure it. Prior to photoresist coating, a thermal treatment is done to improve its adhesion. The samples were placed in an oven for about 20 min, in which they are treated with an atmosphere of Hexamethyldisilazane (HMDS) at 150 ° C to remove any organic impurities that may exist on the surface. The oven used was a Vapour Prime Oven, model 310TA of YES.

Exposure and Development

At this point, the sample is completely covered with a photoresist. Thus, the next step is the selective change of the photoresist chemical structure by exposing the selected areas according to the layouts previously established. This step is called Exposure and can be described by the focusing of a light beam of a specific wavelength on a defined region. This light exposure alters the photoresist structure, preparing it for the next step when the exposed areas are removed with an appropriate solution - Development. Basically, the exposure step will define which area of the resist will be soluble in a developer. As said before, in this work positive resist was used, meaning that the exposed areas will be dissolved in the development stage, whereas with negative photoresist, the exposed areas will remain after the development. Essentially, the final resist pattern is binary: parts of the substrate are covered with a photoresist, whereas other parts are completely uncovered. To begin the Exposure step, the desired exposing pattern is loaded on to the equipment, and the sample is placed and aligned on the stage. Then the exposure can be done. Exposure conditions, as of intensity and focus, are determined by the equipment's responsible team, and are dependent on the current calibration (for example, the last lithography process made was with focus -10 and 60% intensity). The equipment used was the DWL 2000 manufactured by Heidelberg Instruments. To develop the exposed samples, they were loaded on to the same optical track used for the coating, to be washed with AZ400K developer for 60 s, and then rinsed with deionized water.

Etch

To complete the lithography process, the material that is not protected by the photoresist must be patterned. This final step is called etch and involves a chemical and/or physical reaction to remove the material. One key property is required for a good etch: it must be selective, which means that the resist etch rate must be much lower than that of the material to be etched. In a good etch process the resist's etch rate is typically one quarter of the material's one. [84] If this last requirement is not met, the photoresists layer thickness should be adjusted.

Two types of etch were used: wet and dry etch. The first type used an acid solution that chemically attacks the material. The second type, more specifically reactive ion etching, combines a physical (sputtering) and a chemical etching process promoted by a plasma. The plasma high energy ions are anisotropically directed to the substrate surface inducing material's sputtering and generating a volatile by-product.

In this work, it was needed to etch AlSiCu, SiO_x, SiN_x and Si. A 400 nm AlSiCu layer was attacked with a FujiFilm wet Aluminum etch (solution of 80% Phosphoric acid, 5% Nitric acid, 5% Acetic acid and 10% water) for 105 s. The remaining layers were attacked by a dry etch on specialized equipment with specific conditions listed in Table 3.5. Si was etched on the Pegasus LPX and the SiO_x and SiN_x on APS, both manufactured by SPTS Technologies. To remove the residual photoresist layer (Resist Strip) an acetone bath is performed for approximately 5 minutes. Table 3.6 lists the nanolaminates systems used on the capacitors and TLM devices.

Table 3.5: Technical specifications and process details of the dry etches used. The deep silicon etch process, in Pegasus, is called Bosch Process in which two gases allow a complete anisotropic (vertical) etch. The fluorine based plasma etches the Si and the fluorocarbon provides sidewall protection and improves selectivity.

Equipment	APS	Pegasus
Gaseous	Octafluorocyclobutane (C_4F_8)	Sulphur hexafluoride (SF_6) for the Si etch and C_4F_8 to passivate the surface etched
Etch rate (nm/min)	SiO_x: 155 SiN_x:114	Very difficult to know exactly because it depends on the features.
Procedure	In the shadow mask's fabrication, a 3 μm SiO_x layer was etched for 8 min. In the TLM B devices, the total thickness of SiO_x and SiN_x etched in one sample was 30 nm for a 30 s.	In the hard mask's fabrication, was etch a Si substrate with approximately 725 μm for 60 min.

Table 3.6: Capacitors and TLM samples lists and respective architecture.

Capacitor Samples	TLM Samples		
SS0.1	Samples	Thickness (nm)	Architecture
SS0.2			
SS10.1	Si	735	A
SS10.2	Cu	30	
SS10.3	TZ0.1		
SS10.4	TZ0.2		
SS5.3	SS0.1		B
SS5.4	SS0.2		
TZ0.1	SS10.1		
TZ0.2	SS10.2		
TZ1.1	SS10.3		
TZ1.2	SS10.4		
TZ2	SS5.		
TZ3	SS5.4		

3.4 Characterisation Techniques

As said in the Chapter's beginning, it is essential to execute a complete and accurate characterisation of the novel materials created. In the following sections, the used techniques are presented and briefly discussed accordingly with this work aims. As novel material designs are studied, a set of characterisation techniques were used to evaluate the material's fundamental properties, and to plotted a path of adjustments that meet the ultimate goal, the selective contacts. To do so, structural, elemental composition, optical, and electronic properties are discussed. Finally, material's behaviour was evaluated when working under load on a device.

3.4.1 Transmission Electron Microscopy

Transmission Electron Microscopy (TEM) is an imaging technique that allows for the observation of *Ångström* size structures (interfaces, grain boundaries, etc.), the study of the atomic number distribution, among other features. [85] The working principle of this technique is based on the incidence of a high-energy and focused electron beam, with a uniform current density, into a thin sample surface, typically 5-100 nm for 100 keV electrons. The electrons interact through elastic or inelastic scattering with the atoms of the thin sample. [86]

Although the information retrieved from TEM is valuable, the main drawback seats on the complex procedures for the sample preparation, which is significantly time consuming. TEM's working principle is mostly based on an electron gun with energies between 80 and 1200 keV [85], 20-200 keV in the system used, and a set of electromagnetic condenser lenses used to focus the electrons. In this way, it will produced a coherent beam that is directed onto the sample surface. In the conventional TEM the sample is irradiated by a parallel electron beam. From this interaction, electrons are diffracted, scattered, and transmitted. Depending on the wanted information, one of these groups of electrons is selected and detected and the corresponding signal is acquired. The complex arrangement of condenser lenses allows focussing the beam on a small area (0.2-10 nm in diameter), and consequently enables the operation in Scanning Transmission Electron Microscopy (STEM) mode. This allows for the analysis of a small area and a desirable region (for example analyse a linear path through several interfaces). In this mode, Energy Dispersive Spectroscopy (EDS) can be employed to determine the samples chemical composition. The collision of an incident electron with an element inner-shell electron, can eject this electron and leave an unoccupied level. The transition of a higher level electron to the empty level, leads to the emission of an Auger electron or X-ray quantum, which are elemental characteristics. Another technique used in STEM mode is High-angle Annular Dark-Field (HAADF), in which the inelastic high angles scattered electrons are detected by an Annular Dark-Field (ADF) detector and the signal provides images of the crystal lattice and information about the composition.

To execute the STEM-HAADF imaging, EDS and HAADF lines profiles, a FEI Titan ChemiSTEM Cs-probe corrected TEM was used.

3.4.2 X-Ray Diffraction

The macroscopic properties depend greatly on the material's microstructure, hence it is important to characterize it. X-Ray Diffraction (XRD) explores the scattering of X-rays by the atoms in a lattice, providing information on the crystalline phases and structure. It is assumed that a periodic lattice with a given orientation and spacing exists in the material. The incident X-rays will scatter in such structure and will suffer interference. The occurrence of constructive or destructive interference is given by Bragg's Law, which has a dependence on the lattice and beam characteristics, and measurement configuration [87]:

$$2dsin(\theta) = q\lambda \tag{3.1}$$

where d is the inter-planar spacing of the periodic crystal lattice, θ half the angle between the incident and reflected beam, q an integer number, and λ the wavelength value. The previous discussion assumes that the material has a crystallographic structure, but it may be amorphous. A material in an amorphous state has an irregular atomic organization and no periodic structure, so the incident X-rays are scattered in many directions, and the signals peak to background ratio is low or zero, and the diffractogram peak will be broad or non-existent. [88]

The conventional symmetric setup, where the source and detector angle are equal, is called Bragg Brentano XRD and is schematically shown in Fig. 3.8 (a). The higher the incident angle, the longer is the total X-ray's path length. Therefore, when a thin sample on a substrate is analysed, the substrate signal will be higher than the thin film one. In this way, the identification complexity, of the lattice pattern of the thin film, is hindered. The Grazing Incidence X-Ray Diffraction (GIXRD) asymmetric configuration may be employed to get around this limitation. The angle of incidence is fixed at a low angle, typically lower than 1°, to provide a higher surface sensibility (Fig. 3.8 (b)).

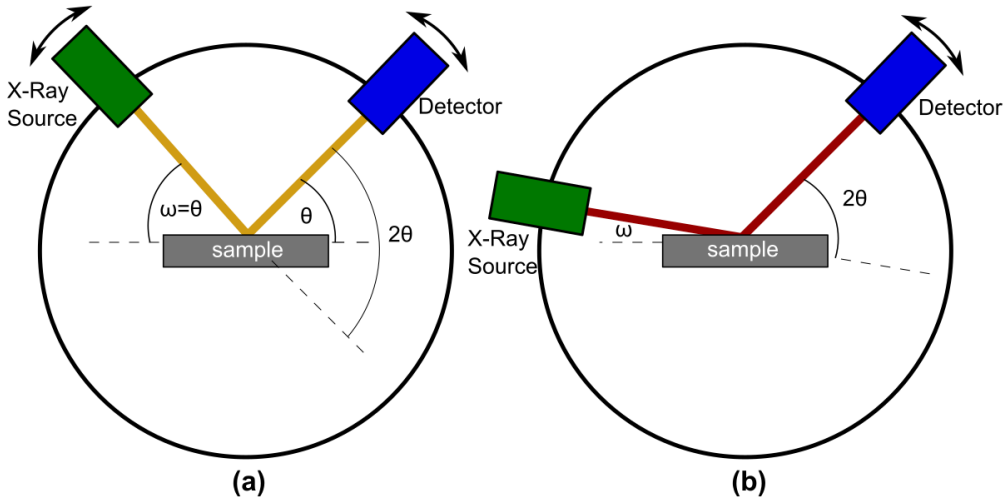

Figure 3.8: XRD configuration to perform (a) conventional Bragg-Brentano and (b) Grazing Incidence (GIXRD) measurements. The incidence angle ω is equal to the detector angle θ in the conventional configuration and remains constant in GIXRD. The angle between the incident and diffracted beam is 2θ, and is the independent variable of the obtained diffractogram.

The system D8 Advance, manufactured by Bruker and with a Cu-Kα parallel beam X-ray source, was used for XRD based measurements. Initially, two Bragg-Brentano XRD measurements with different orientations, rotating the sample on the holder, were done to find out if the samples had a preferential alignment and if it was possible to diminish the substrate (Si) signal. Then, quick GIXRD sweeps at different ω angles were done to determine the angle that provided the best peak intensity to background ratio. Being the ω optimized at 1° for all samples, a long (more than eight hours) measurement was done. Afterwards, the peak fitting was done with a Voigt function, convolution of a Lorentzian and a Gaussian function, to evaluate the samples' structure.

3.4.3 Optical Spectroscopy

Spectroscopic Ellipsometry

Ellipsometry, allows to estimate the optical constants and film thickness values through the interaction of a polarized beam of light with the sample. A linear polarized electromagnetic wave, with *s* and *p* components, is generated at the light source and redirected to the sample at a given angle of incidence (ω). From the incident light-sample interaction results a light beam with a polarization different from the initial. This final polarization is typically elliptical, reason why this technique is called ellipsometry. [89] The polarization state of the electromagnetic wave before and after the reflection in the sample is shown in Fig. 3.9.

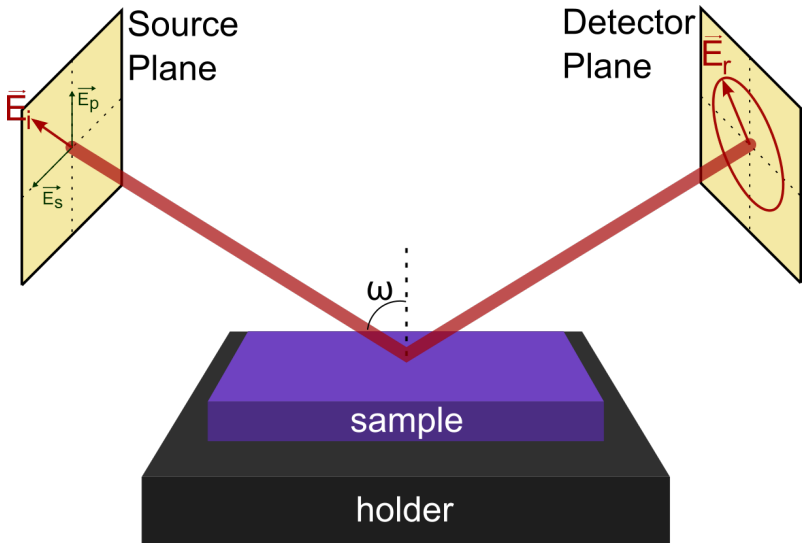

Figure 3.9: Representation of the light beam and sample interaction. $\vec{E_i}$ and $\vec{E_r}$ is the electric field vector of the incident and reflected light beam, respectively, with $\vec{E_p}$ and $\vec{E_s}$ parallel and perpendicular, with respect to the plane of incidence, components, respectively. The electromagnetic wave polarization changes upon sample interaction. The angle on incidence ω is kept constant during each wavelength sweep.

From the light-sample interaction, two parameters that reflect the change in polarization state, after the interaction, are measured. The complex reflectance is parametrized by two wavelength dependent interaction parameters, ψ e δ, which are the amplitude ratio and phase difference, respectively, and are described by [90]:

$$tan\psi exp(i\Delta) = \frac{r_p}{r_s} = \frac{\left(\frac{E_{r,p}}{E_{i,p}}\right)}{\left(\frac{E_{r,s}}{E_{i,s}}\right)} \tag{3.2}$$

where E_r and E_i are the electrical field of the reflected and incident waves, respectively, for both polarizations s ($E_{i,s}$ and $E_{r,s}$) and p ($E_{i,p}$ and $E_{r,p}$), and r_s and r_p are the complex reflectance, again, for both polarizations s and p.

Although correlated, these parameters can be separated and their physical meaning becomes more evident [90].

$$tan\psi = \frac{|r_p|}{|r_s|} \tag{3.3}$$

$$\Delta = \delta_p - \delta_s \tag{3.4}$$

Here δ_p and δ_s are the electromagnetic waves phases of the reflected p and s components, respectively.

After carrying the measurements, a model that describes the studied sample needs to be established. This optical model accounts for all the sample layer's thicknesses and optical characteristics (optical constants, n and k, or complex dielectric function (ε) with real (ε_1) and imaginary (ε_2) part, $\varepsilon = \varepsilon_1 - i\varepsilon_2$) as represented in Fig. 3.10. Hence, some samples insight is always needed. Also, due to the fitting type analysis, as more parameters are known the more accurate the result will be. Thus, the studied material should be coupled with well known references layers. If goal is to measure the layer thickness (d), the layer's optical characteristics must be introduced or selected from the database; if it is aimed to determine the optical characteristics the layer's thickness should be introduced, and the model that best describes the material must be selected for the fitting.

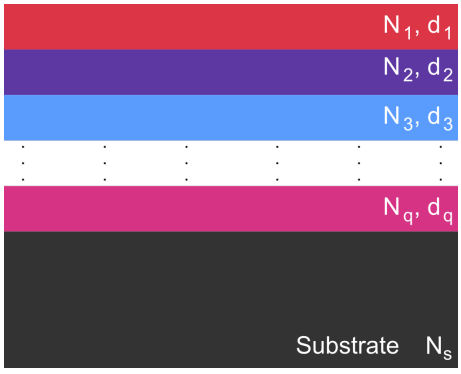

Figure 3.10: Phenomenological representation of the optical model used to describe a q multilayer stack, on a substrate s. Each layer is represented by the optical characteristics, here defined by the complex refractive index N_j and thickness d_j. The optical constants can be introduced as the optical constants n and k ($N = n - ik$) or by the dielectric function ($N = \sqrt{\varepsilon} = \sqrt{\varepsilon_1 - i\varepsilon_2}$).

The parameters that are unknown will be determined by a fitting using a numerical algorithm. In simple steps, the program generates ψ^* and Δ^* parameters with the inputted values and characteristics of the optical model. Then it compares the generated data with the measured one, by internally determining the Mean Square Error (MSE): the sum of the absolute difference of the measured and generated values. If the data sets are equal, which is expected to happen after a few iterations, the fitting is over, MSE is small, and the unknown parameters are determined. If they differ, the program knows which unknown parameters to vary, and by how much, to decrease MSE, and an iteration is done to fit the values.

After executing the software fitting, the fit quality can be analysed by the MSE and the physical meaning of the result must be judge. If necessary, the optical model must be altered to more accurately describe the sample. A flow chart describing this procedure is represented in Fig. 3.11.

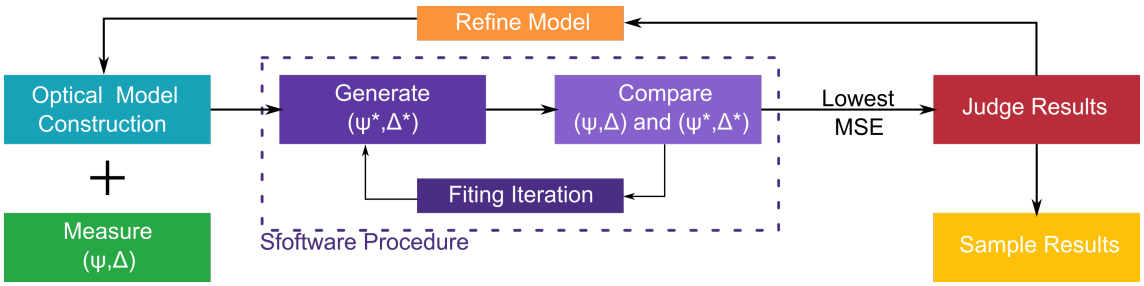

Figure 3.11: Flow chart of the ellipsometry data analysis procedure. Firstly, the measurement is performed and the optical model is constructed. After that, the program can fit the unknown parameters with input values and characteristics of the model, highlighted on "Software Procedure". When the fit is over, it is necessary to find out if the output results make sense and present physical meaning. If accepted the procedure is complete, if not, a model refinement is necessary to improve the results.

Regarding the optical characteristics (optical constants, n and k, or dielectric function, $\varepsilon = \varepsilon_1 - i\varepsilon_2$), these can be directly introduced by an experimental data set or modulated by a mathematical model with parameters, specific of the material. There are several models to describe the optical characteristics, and each one has a distinct modelling fundamentals and applications. The ones used in this work, Cauchy, Lorentz, and a Tauc-Lorentz, are described as follows:

- **Cauchy:**

The empirical Cauchy model can be derived from a theoretical model called Sellmier, which describes the material as a collection of dipoles with a specific resonant frequency. This model is mostly used for transparent materials ($k(\lambda) = 0$): [90]:

$$n(\lambda) = A + \frac{B}{\lambda^2} + \frac{C}{\lambda^4} \tag{3.5}$$

here the parameter A states the amplitude of the refractive index function, and B and C set the function curvature. This model directly describes the optical constants and not the dielectric function. The relation between n and k, and the complex dielectric function (ε_1 and ε_2) is well established [89]:

$$\varepsilon_1 = n^2 - k^2 \qquad \varepsilon_2 = 2nk \tag{3.6}$$

$$n = \sqrt{\frac{\varepsilon_1 + \sqrt{\varepsilon_1^2 + \varepsilon_2^2}}{2}} \qquad k = \sqrt{\frac{-\varepsilon_1 + \sqrt{\varepsilon_1^2 + \varepsilon_2^2}}{2}} \tag{3.7}$$

Also, usually, the independent variable of the dielectric function is the photon energy (hv) and not the light wavelength (λ). Nevertheless, they are correlated by $hv = hc/\lambda$, where h is the Planck's constant and c the free space light speed. Although being designed to modulate transparent materials, the Cauchy model can be extended and introduce some absorption. The Urbach equation is added, which has a decaying exponential shape and describes a small absorption below the bandgap energy [89]:

$$k(hv) = \beta e^{\frac{hv - E_b}{E_U}} \tag{3.8}$$

where β is the amplitude, E_U the Urbach energy and E_b the band edge.

• **Lorentz:**

Lorentz is a theoretical model that takes a more classical approach. It is considered that the electron's response to electrical field is identical to that of a mass connected by a spring when a dissipative force is applied. In this sense, the body mass is a representation of the electrons, the spring is similar to the forces exerted by neighbours electrons and nuclei on the electron, and the dissipative force is the energy loss due to a photon emission. [91]

$$\varepsilon(hv) = \varepsilon_1(hv) - i\varepsilon_2(hv) = 1 + \frac{D}{E_0^2 - (hv)^2 + i\Gamma hv} \tag{3.9}$$

Here, D is the oscillator strength, E_0 the energy centre and Γ the broadening. From Eq. 3.9, the complete complex dielectric function is obtained and not the separate real and imaginary part. One cannot simply separate the real from the imaginary part when the equation is fully resolved, because ε_1 and ε_2 are physically connected. So, the Kramers-Kronig (KK) Relations are utilized. These equations institute a mathematical connection between ε_1 and ε_2. Physically speaking, this connection establishes a cause-effect relationship, which means that the effect (dipole response) can only occur after the cause (electric field) [91]:

$$\varepsilon_1(hv) = 1 + \frac{2}{\pi} P \int_0^{\text{inf}} \frac{E' \varepsilon_2(E')}{E'^2 - (hv)^2} dE' \tag{3.10}$$

$$\varepsilon_2(hv) = -\frac{2E}{\pi} P \int_0^{\text{inf}} \frac{\varepsilon_1(E')}{E'^2 - (hv)^2} dE' \tag{3.11}$$

where P is called the principal part of the integral and E' the integral variable.

The Lorentz model is very well suited to described dielectrics and semiconductors. One variation of this model that only allows the absorption above the bandgap is known as Tauc-Lorentz. This model is suited for most amorphous materials, and follows [91]:

$$\varepsilon_2(hv) = \frac{FE_0C(hv-E_g)^2}{(hv-E_0)^2+G^2(hv)^2}\cdot\frac{1}{hv}, \quad hv > E_g \tag{3.12}$$

$$\varepsilon_2(hv) = 0, \quad hv \leq E_g \tag{3.13}$$

Here, F and G are amplitude and shaping parameters.

Once again, using KK Relations is possible to obtain the dielectric function's real part:

$$\varepsilon_1(gv) = \varepsilon_1(\text{inf}) + \frac{2}{\pi}P\int_{E_g}^{\text{inf}}\frac{E'\varepsilon_2(E')}{E'^2-(hv)^2}dE' \tag{3.14}$$

The optical model constructed in ellipsometry can be simple or complex, depending on the samples complexity. The features described beforehand are the basic requirements to preform these measurements. Advance features as surface roughness, layer optical characteristics grading or a collection of dielectric functions, instead of one, used to model the layer can be applied. Nevertheless, these additional features will complicate the fitting process and no general solution may be found or the fitted parameters may have large uncertainties. A good practice, is to start with the simpler and basic model, but that completely describes the sample, and individually add features. Only accepting the added feature, if the MSE suffers a 25% improvement.

To perform the Ellipsometry measurements (at 55°, 65°, and 75° of incidence) described a J.A. Woollam M2000 ellipsometer was used and the analysis, to obtain the layer thickness and optical constants, were done on the CompleteEase software also provided by J.A. Woollam.

UV-Vis-NIR Spectrophotometry

Since Ellipsometry is a complex technique that requires some knowledge about the sample, it is a good practice to use a complementary technique to validate the obtained results. Thus, Ultraviolet - Visible - Near Infra Red (UV-Vis-NIR) Spectrophotometry was used. This is a simpler technique and relies on the intensity ratio of two light beams. As represented in Fig. 3.12, two identical light beams enter the apparatus: one serves as a reference and the other will interact with the sample. Two related quantities can be measured depending on the sample's position: relative transmittance and reflectance. For each, total or diffuse behaviour can be scrutinized. Relative total reflectance and transmittance were measured in the wavelength value range of 300-1100 nm and a step size of 1 nm using a Perkin Elmer Lambda 950.

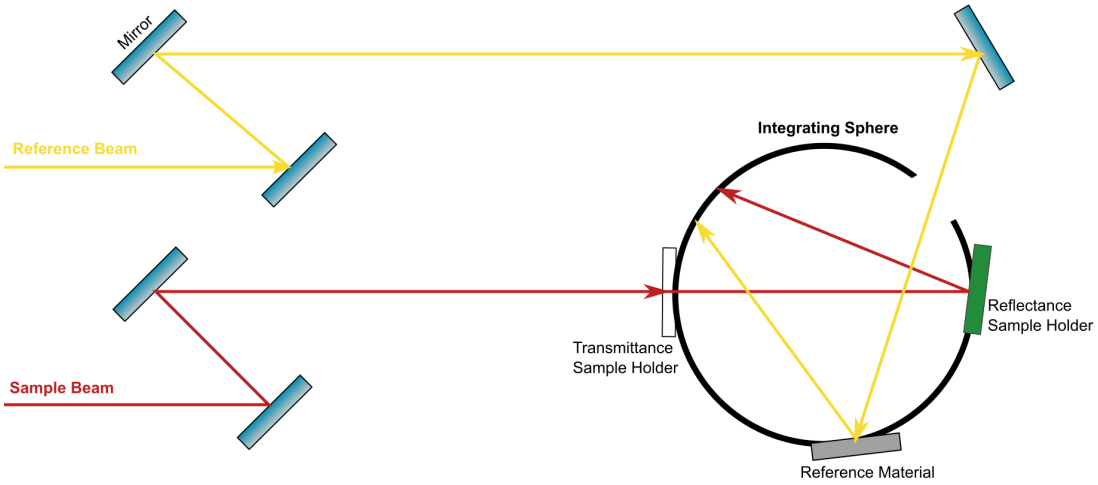

Figure 3.12: UV-Vis-NIR Spectrophotometry schematic with an integrating sphere detector. The reference material is made of spectralon (fluoropolymer with the highest diffuse reflectance).

After the measurements, it is necessary to convert the Ellipsometry or UV-Vis-NIR Spectrophotometry data so that they are comparable. Using the determined optical constants, n and k, as variables, it is possible to calculate the reflectance and transmittance. So, the comparison between the ellipsometer and spectrophotometer data will be done with the total reflectance and transmittance spectra (in nominal % values). A variation of the Fresnel Equations is used to determine the relative transmittance and reflectance. The transmittance (T) was calculated considering normal incidence, a transparent substrate ($k(\lambda) = 0$) [92, 93, 94]:

$$T = \frac{16n^2 \cdot n_s e^{-\alpha d}}{(n+1)^3(n+n_s^2) - 2(n^2-1)(n^2-n_s^2)e^{-\alpha d}cos(\frac{4\pi nd}{\lambda}) + (n-1)^3(n-n_s^2)e^{-2\alpha d}} \tag{3.15}$$

Where n_s is the substrate refractive index, n the refractive index of the film and its respective thickness d, α is the absorption coefficient which is related to the k by $\alpha = \frac{4\pi k}{\lambda}$, for each wavelength value. The reflectance (R) equation considers a complex structure of q layers and a substrate s, that describes the beam interaction at each layer's interface, and the calculation can be divided in two steps. First is necessary to solve a matrix equation [95]:

$$\begin{bmatrix} M \\ N \end{bmatrix} = \left(\prod_{j=1}^{q} \begin{bmatrix} cos(\tau_j) & \frac{isin(\tau_j)}{\eta_j} \\ i\eta_j sin(\tau_j) & cos(\tau_j) \end{bmatrix} \right) \begin{bmatrix} 1 \\ \eta_s \end{bmatrix} \tag{3.16}$$

$$with \quad \tau_j = \frac{2\pi n_j d_j cos(\omega_j)}{\lambda} \tag{3.17}$$

Where η_s is the substrate tilted admittance, and η is the tilted optical admittance, which can be defined for parallel (p) and perpendicular (s) light polarizations [95]:

$$\eta_p = \frac{n\vartheta}{cos\omega} = \frac{y}{cos\omega} \quad and \quad \eta_s = n\vartheta cos\omega = ycos\omega \tag{3.18}$$

where ϑ is the admittance of free space (equal to 2.6544×10^{-3} S) and y the optical admittance. Then, is necessary to calculate the total admittance (Y) of the q layers system [95]:

$$Y = \frac{N}{M} \tag{3.19}$$

which is introduced on the final equation with the initial medium tilted optical admittance (η_0) [95]:

$$R = \left| \frac{\eta_0 - Y}{\eta_0 + Y} \right| \tag{3.20}$$

When the calculation of transmittance and reflectance are finished, a conjoined plot of the measured and calculated reflectance or transmittance can be executed to verify that the optical constants, n and k, were determined through Ellipsometry with accuracy.

3.4.4 Photoelectron Spectroscopy

The main physical principle underlying the photoelectron spectroscopy is the photoelectric effect. To induce the photoelectric effect the sample is irradiated with X-rays or ultraviolet (UV). If the photon's energy of the incident beam is sufficient, an electron is ejected. Depending on the photon's energy, core level electrons or more superficial ones can be ejected, providing distinct information. Hence, a photoelectron spectroscopy technique is capable of determining the material's composition (Elemental Quantification), and allowing the discussion of the material's electronic structure.

Elemental Quantification

X-ray Photoelectron Spectroscopy (XPS) is a photoelectron technique that uses X-rays, photons with energy higher than 1 keV, which can reach the materials core levels. Thus, this technique can be used to quantify the sample's elemental composition.

Each element has a specific energetic transition that allows the identification its existence, and quantify the existing amount in the sample. Firstly, an acquisition is done in the transition energy range in order to study a particular element. The acquired spectrum represents the number of electrons counted per second (counts/s) at each binding energy (BE). This energy represents the energy lost in the interaction with the material. Knowing the initial and final energy, is possible to determine the binding energy by [96]:

$$KE = hv - \Phi_{XPS} - BE \tag{3.21}$$

$$BE = hv - KE - \Phi_S = hv - KE - \Phi_{XPS} \tag{3.22}$$

where KE the kinetic energy of the reflected electron, and Φ_{XPS} and Φ_S the equipment and sample work function. The latter two are considered equal.

After the spectrum acquisition, similar to the one represented in Fig. 3.13, it is fitted using a Voigt function. The area of the fitted peak (A_i) is used to do the quantification. Nonetheless, first a normalization is necessary, due to different elements having distinct X-ray interactions. Relative Sensing Factor (RSF) is used to normalize the peak areas and reflects such elements differences in a given equipment, since different types of equipments with different configurations may have distinct interactions. Hence, the element percentage (X_i) can be estimated by:

$$X_i = \frac{\frac{A_i}{RSF_i}}{\sum_{j=0}^{N} \frac{A_j}{RSF_j}} \times 100\% \tag{3.23}$$

Table 3.7 summarizes the Si, Zn, Ti, Hf, oxygen (O), and N required values to determine X_i.

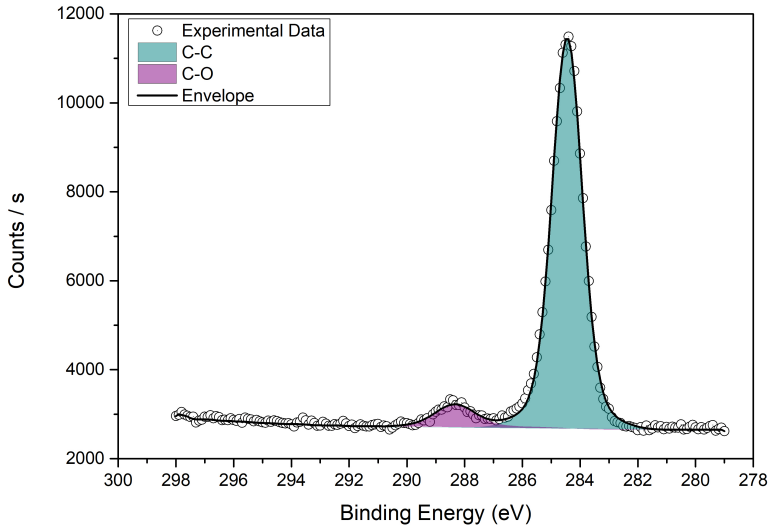

Figure 3.13: As measured surface carbon 1s (C 1s) spectrum of a 30 nm ZnO_x sample deposited on a SLG substrate. Without any fitting, it is clear the existence of two distinct peaks that correspond to different C bonds. The identification of the peaks was based on the XPS software database.

Table 3.7: Elements peaks and respective characteristics used to calculate sample's composition X_i. The BE and RSF values were obtained from the Avantage software database.

Element	Peak	BE (eV)	RSF
Oxygen	O 1s	529-530	2.881
Nitrogen	N 1s	397	1.676
Oxide Element	Peak	BE (eV)	RSF
Silicon	Si 2p	103.5	0.900
Zinc	Zn $2p_{3/2}$	1 022	21.391
Titanium	Ti $2p_{3/2}$	458.5	4.415
Hafnium	Hf $4f_{7/2}$	18.3	4.410

Electronic Properties

One important property in the design of selective contacts or any multilayered optoelectronic device is the electronic structure, which is represented by a band diagram with energy levels: conduction band minimum (E_C), Fermi Level (E_F), valence band maximum (E_V) and bandgap ($E_g = E_C - E_V$). To construct such band diagram, XPS, Ultraviolet Photoelectron Spectroscopy (UPS), and Reflection Electron Energy Loss Spectroscopy (REELS) were employed.

As XPS is able to reach core levels, it can be used to measure the difference between the E_V and Fermi level ($E_F - E_V$). UPS, another photoelectron spectroscopy technique, uses UV radiation to induce the photoelectric effect. The photon's energy is typically around dozens eV, which only allows reaching the valence band. Hence, UPS is used to determine the work function (ϕ) and, also, the $E_F - E_V$ value. In REELS, employed to determine the E_g energy value, the samples are analysed using a beam of electrons, instead of photons, and it is measured the energy loss of the scattered electrons. Hence, this method does not induce photoelectric effect. The electron's energy loss may be due to many causes, however as it is used to determine the E_g energy value, the transition of an electron from the E_V to the E_C is needed. To raise such transition, an inelastic collision of the incident electrons with the material's electron must occur, and the incident electron must have equal or higher energy than the bandgap energy value. The procedure executed to calculate these electronic parameters is described in Table 3.8.

Table 3.8: Graphical method to determine each electronic parameter from each different technique.

Technique	Determination Description
XPS	Around and at 0 eV BE the XPS spectrum has 0 counts/s, but when the BE increases, so do the counts/s. This region, has a linear behaviour where a linear regression has to be made. The BE axis interception of this linear function is the $E_F - E_V$ value.
UPS	The method to calculate $E_F - E_V$ value from the UPS spectrum is identical to the XPS one. To evaluate the ϕ value, the edges of the UPS spectrum must be analysed. At higher energies the spectrum has a steep descend called cut-off. In the beginning, at lower BEs, the counts/s are null and then start to rise onto a small plateau. The beginning of such plateau is the location of the E_F. The difference between the cut-off energy and the E_F is the spectrum width, and the subtraction of the spectrum width from incident photons energy, gives the ϕ value. ($\phi = h\nu - (E_{cut-off} - E_F)$)
REELS	The calculation of the E_g value is identical to the $E_F - E_V$ energy value. However, the REELS spectrum has a maximum counts/s peak at 0 eV, followed by the hydrogen (H) peak, at $\sim$ 2.5 eV. After the H peak, the spectrum has a minimum and starts to rise linearly. In this rising region the linear regression should be done and the interception of the BE axis gives the E_g energy value.

The system ESCALAB 250Xi, manufactured by Thermo Fisher Scientific, was used in this work and it is an XPS, UPS and REELS integrated equipment. The X-ray source is based on Al-Kα transition and emits photons with 1 487 eV, and the UV photons in UPS are based on He I with 21.2 eV of energy. The incident electrons in REELS are accelerated with a kinetic energy equal to 1 000 eV. The peak analysis was done using the Avantage 5.988 software also provided by Thermo Fisher Scientific.

3.4.5 Electrical Measurements

When a nanolaminate is incorporated into a device, its behaviour can be different from when is apart, because materials can exhibit different responses when working on load. Thus, electrical characterisation is crucial when incorporating a new material's concept into optoelectronic devices. To perform such characterisation, capacitance measurements and conventional current-voltage curves were carried out.

The capacitance analysis, measures the capacitance and resistance of the sample dependence with frequency and/or voltage. The equipment, E4980A LCR Meter from KEYIGHT, models the sample layer, as a capacitor in parallel with a resistor. Such model is used in the Conductance Method, on metal-insulator-semiconductor structure, to calculate the interface traps and fixed charge density. [97] The measurements were performed on a capacitor structure, as it will be discussed latter in Chapter 4. The current-voltage (IV) curves, extremely used in solar cells characterization, were done using the 2420 SourceMeter by KEITHLEY and serve to apply the TLM.

Transfer Length Method

Transfer Length Method (TLM), initially proposed by Shockley [98], allows calculating the contact resistivity (ρ_c) and the sheet resistance (R_{Sh}) of a material. A series of gradually spaced parallel contacts, with dimensions W and L, are placed on the sample (Fig. 3.14) and current-voltage curves between two adjacent contacts are measured.

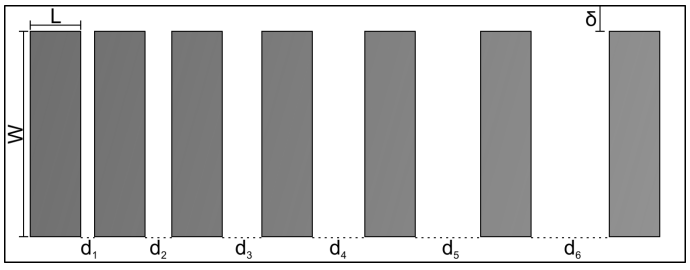

Figure 3.14: Contacts, with W x L dimensions, layout to perform the TLM measurements. The spacing d_i between contacts is increasing from left to right, and δ is the gap between the contact's and the sample layer edges.

From the linear current-voltage curve, assuming an ohmic behaviour, the total resistance (R_T) is calculated by applying Ohm's law. When all contacts have been measured, a R_T *vs* contact spacing (d_i) is obtained, as shown in Fig. 3.15, following a linear trend, corresponding to:

$$R_T = \frac{R_{Sh}}{W} d_i + 2R_c \tag{3.24}$$

here R_c is the contact resistance. Eq. 3.24 describes the total resistance as the sum of sheet resistance (R_{Sh}) between the contacts and R_c:

$$R_c = \frac{R_{Sh} L_T}{W} \coth\left(\frac{L}{L_T}\right) \tag{3.25}$$

R_{Sh} is part of the slope, since as the contact spacing increases, more material the current has to flow through through and more resistance it will fell. R_c is keep as a constant, since only two contacts are considered and their area is not changed. The transfer length (L_T) defines the distance required to transfer all the current from the metal to the material [99] and is defined as:

$$L_T = \sqrt{\frac{\rho_c}{R_{Sh}}} \tag{3.26}$$

Contact resistivity can be determined by two ways depending on the contact dimensions [100]:

(a) if $L_T \gg L$, then $\coth\left(\frac{L}{L_T}\right) \approx \frac{L_T}{L}$, so $R_c = \frac{R_{Sh} L_T^2}{WL}$ and $\rho_c = R_c W L$;

(b) if $L_T \ll L$, then $\coth\left(\frac{L}{L_T}\right) \approx 1$, so $R_c = \frac{R_{Sh} L_T}{W}$ and $\rho_c = R_c W L_T$.

To ensure accurate parameter determination, the gap between the contact's and the sample layer edges (δ) must be zero or negligible when compared to W. If this condition is not met, the Quasi Two-Dimensional TLM (QTD-TLM) correction must be employed because new resistance contribution appears due to current flow at the contact's top and bottom. [101] Figure 3.15 presents an example of the application of the TLM method.

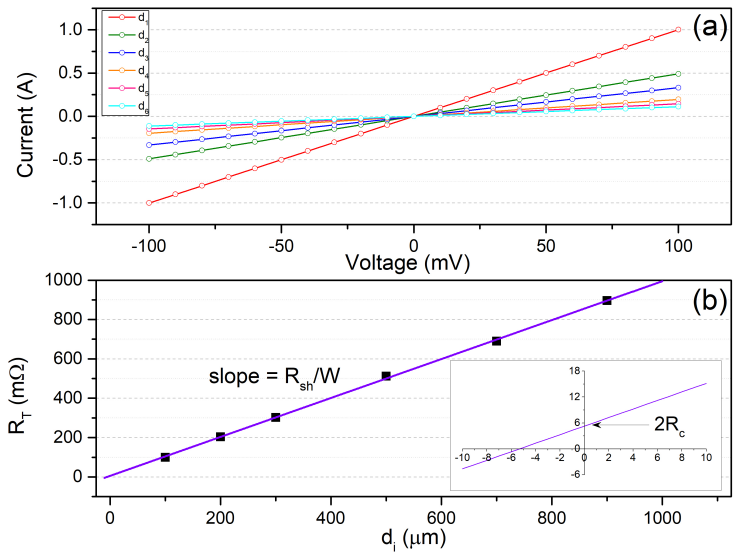

Figure 3.15: Hypothetical application of the TLM method on a sample sheet with 6, 1000 μm $\times$ 20 000 μm, contacts. (a) The IV curves clearly show the resistance increase with contact spacing. Linear regression in each curve, allows to calculate the total resistance (R_T). (b) R_T *vs.* d_i plot, corresponding to Eq. 3.24, and obtain the needed parameters. The purple linear regression gives an 0.990 mΩ/μm slope and 5.275 mΩ intercept, which corresponds to a R_{Sh} = 19.8 Ω and R_c = 2.638 mΩ. Considering $L_T \ll L$, L_T = 2.665 μm, proving the assumption true, and ρ_c = 1.4 Ω·mm^2.

3.4.6 Other Characterisation Techniques

Contact Profilometer

The contact profilometer, P-16+ manufactured by KLA Tencor, was used to measure the deposited film thickness values. This technique was mostly useful in the calculation of the deposition rates. The system uses a small stylus connected to a sensor that, in contact with the sample, register the transversal displacement while the stylus moves on a longitudinal direction which allows to perform a topographic analysis.

Optical Microscope

An optical microscope is a system constituted by stage, optical lenses and a digital camera or an observation window. Uses visible light focused on the sample to investigate its surface. In this work, a Nikon Eclipse L200N was used for inspection during the devices development process for surface and devices contacts characterisation.

4

Results and Discussion

The previous Chapters present the foundations and an overview of the developed work, which is to be discussed in more detail in this Chapter. Chapter 2 exploited the requirements, potential of nanolaminates and selective contacts. In Chapter 3 a detailed discussion of the experimental methods was presented, to assist the result's discussion. Therefore, in Chapter 4 the characterisation approach and results are presented. Starting with a structural characterisation, followed by a discussion on the materials elemental composition. Then, an optical, electronic, and electrical analysis will be presented.

4.1 Structural Characteristics

A structural characterisation is crucial, since provides information that can often justify the subsequent observed properties. A periodic or random atomic organization is related to the functional properties and, at a great extent, determines the materials optoelectronic properties. [87]

The samples were firstly studied by Raman spectroscopy, an optical non-destructive technique capable of analysing a sample's structure and chemical composition. [85] The measured spectra provided no valuable information, since the observe Raman peaks were identified as vibrational states of the Si substrate. Fig. B.1 in Appendix B, presents the Si substrate and sample SS0.1 Raman spectra. So, this approach was abandoned because, for all the samples, the substrate data would be predominant. If the further analysis were to be performed with Raman spectroscopy, the incident photon wavelength must be lower to a deep UV excitation range, so the penetration depth be decreased. [102] However, the measurements were performed at minimum wavelength setting, 532 nm incident photons, therefore no valuable study could be carried on with the available equipment. Therefore, XRD was carried out to characterize the structural properties. Similar to Raman, if XRD is performed without the appropriate configuration, in this case, if the incident angle is too high, the measurement resolution will be small and only substrate diffractogram peaks will be detected. Nevertheless, conventional XRD was used, as mentioned in Subsection 3.4.2, to test the possibility of eliminating the Si contribution with a simple sample rotation. Such possibility exists because the Si substrates used, are cut along a (100) crystal plane. However, substrates diffractogram peaks were always present, no matter the sample rotation. Hence, the Si contribution is

present in all GIXRD diffractograms, as shown in Fig. 4.1 by the highlighted grey dashed region between 47.5-57.5°. These Si contributions had been formerly reported [103].

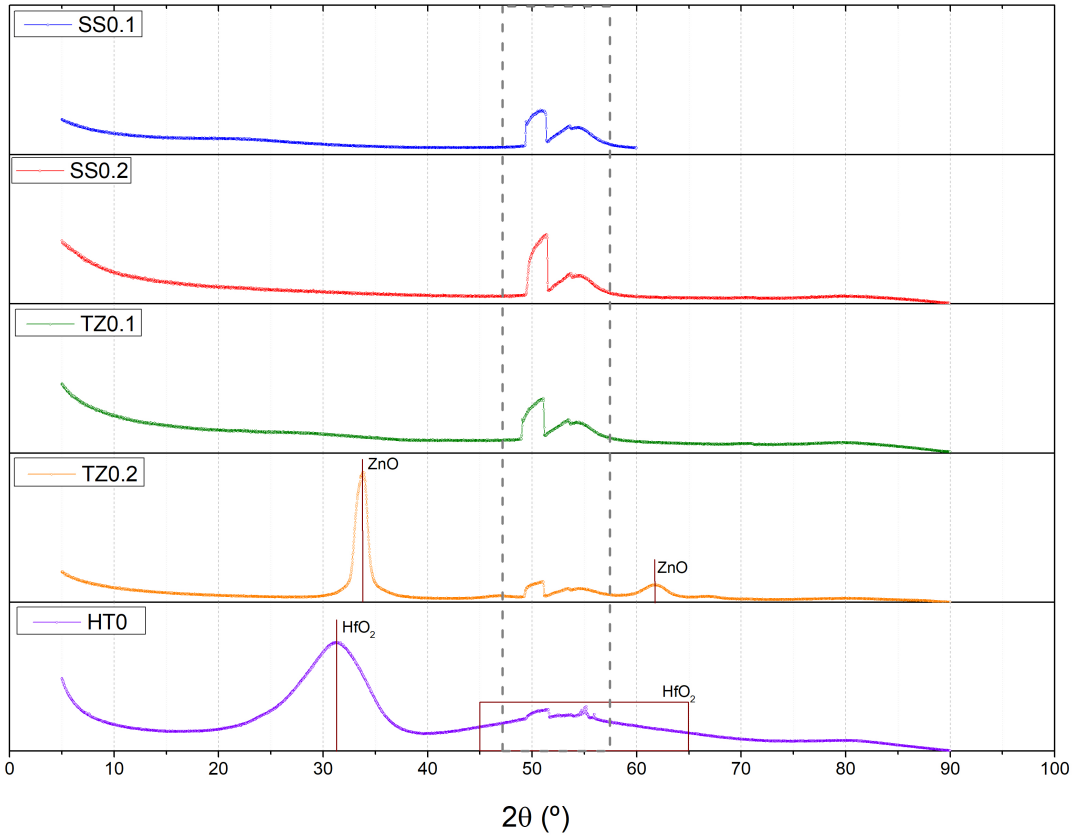

Figure 4.1: GIXRD diffractogram of samples SS10.1, SS10.2, TZ0.1, TZ0.2, and HT0. Vertical burgundy line or box guides to regions where might exist a ZnO_x or HfO_x diffractogram peak, while the grey dashed rectangle highlights the Si substrates diffractogram peaks found in all samples.

In Fig. 4.1 individual layers, SiO_x, SiN_x, TiO_x, ZnO_x, and HfO_x GIXRD diffractograms are presented. Besides the discussed Si contribution, only the samples TZ0.2 and HT0 clearly show characteristics diffractogram peaks in the 30-38° and 60-65°, and 20-40° and 45-65°, respectively. However, both present broad peaks, with low intensity when compared with the background. This indicates a predominance of amorphous states, with no periodic structure, for the latter discussed samples, and more significantly for the remaining ones. Such amorphous structure was expected, since both deposition methods, PECVD and Magnetron Sputtering, are not performed at high enough temperature (below 300°C and at Room Temperature (RT), respectively) to form long periodic structures. As an example, diffraction peaks may exist for Si deposited by PECVD at temperatures lower than 470°C, but the amorphous state is still predominant. [104] Similarly, for ZnO deposited by Magnetron Sputtering, a temperature higher than 200°C is needed for some crystal orientation to be predominant, although with small crystalline size. [105]

In order to carry out an in-depth discussion of the sample's structure, a closer look at the individual layers diffractograms was performed. The diffractogram acquisition of sample SS0.1 [1], SiO_x, was only undertaken from 5 to 60°, considering that literature only highlights a characteristic SiO_2 peak at around 25°. [106] In Fig. 4.2 is shown the SS0.1 diffractogram in the 10-35° range, where it was identified a SiO_x diffraction peak. This peak, centred at 22.1° and a Full Witdh at Half Maximum (FWHM) of 16° has a predominant Lorentzian shape, and can be ascribed to amorphous SiO_2. [106, 107] On the other hand, sample SS0.2, SiN_x, has no observable peaks, so no further analysis was performed.

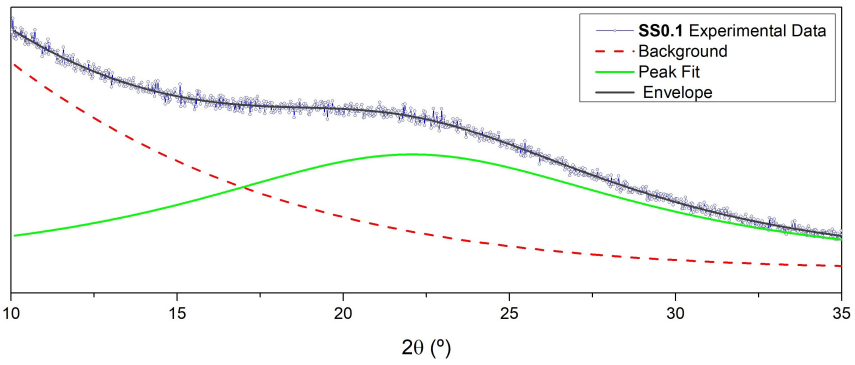

Figure 4.2: Sample SS0.1, SiO_x individual layer, GIXRD diffractogram of the selected range, 10-35°, and respective fitted peaks.

For samples TZ0.1, TiO_x individual layer, two ranges of interest were identified and depicted in Fig. 4.3 (a) and (b). In the 15-45° range, presented in Fig. 4.3 (a) was identified a diffraction peak at 28.45°, deconvoluted by a Gaussian predominant fit, with FWHM of 11.72° assigned to the rutile TiO_2 (110) plane. Considering the 65-75° region (Fig. 4.3 (b)), two peakS at 70.0° and 70.87° were deconvoluted by a Gaussian predominant model, with 1.9° and 0.3° FWHM, respectively. Nevertheless, almost negligible intensity compared to the background was obtained. These two peaks can be identified as rutile (301) and anatase (119) phases of TiO_2, respectively. The peaks identification was carried based on literature. [108]

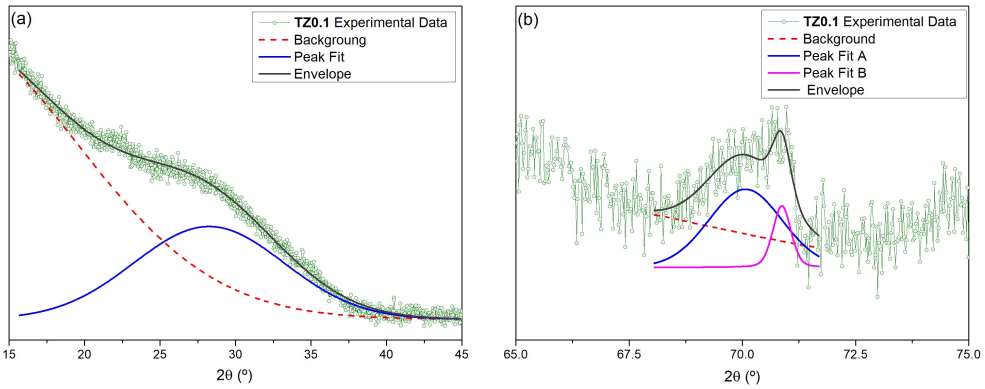

Figure 4.3: Sample TZ0.1, TiO_x individual layer, GIXRD diffractogram of the selected ranges: (a) 15-45° and (b) 65-75°, and respective fitted peaks.

[1] If necessary, the samples label and corresponding characteristics can be consulted in Table 3.3.

Sample TZ0.2, ZnO_x individual layer, shows two predominant Lorentzian peaks around the 34° region, shown in Fig. 4.4 (a), and predominant Gaussian peaks at ∼ 46°, 62°, and 67°, as can be seen in Fig. 4.4 (b), (c), and (d), respectively. The first peak at 33.36°, with 0.89° FWHM, was ascribed to the (002) plane, and for the 33.96° no match was found. Gaussian peaks at 46.7° (2.3° FWHM), 61.76° (2.5° FWHM), and at 66.9° (2.3° FWHM) are related to the ZnO (102), (103), and (112) planes, respectively. [109] The peaks experience a ∼-1° shift from the literature values, for which no justification was found, but can be speculated that a change in the lattice parameters has occurred [110], or this was due to an experimental constrain. All of the above assigned crystal planes, are associated with ZnO hexagonal wurtzite phase.[111]

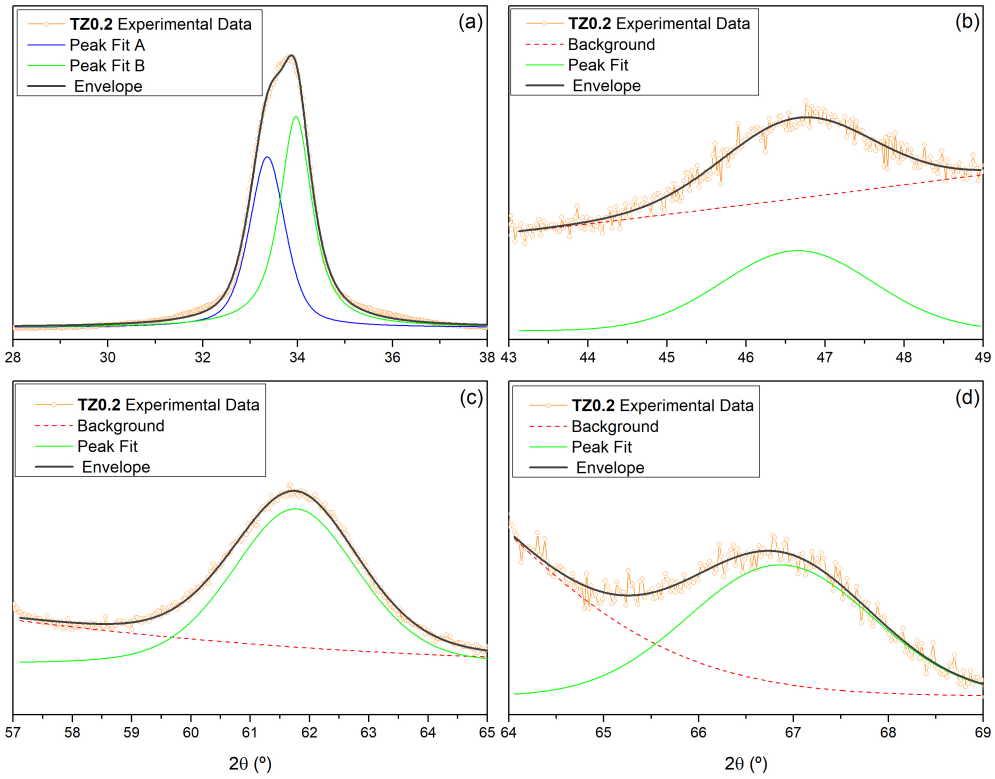

Figure 4.4: Sample TZ0.2, ZnO_x individual layer, GIXRD diffractogram of the selected ranges: (a) 28-38°, (b) 43-49°, (c) 57-65°, and (b) 64-69°, and respective fitted peaks.

In HT0 sample, HfO_x individual layer, a Gaussian preponderance was found for all peaks presented in Fig. 4.5. The ones in the 20-40° range (Fig. 4.5 (a)), were easily fitted, but the ones present in the 40-75° range (Fig. 4.5 (b)), the Si substrate peaks superposition lead to difficulties in the fitting process. The peak parameters had to be manually adjusted. Nevertheless, the Envelope curve follows the experimental data. The 20-40° region was deconvoluted in two diffraction peaks at 27.3° and 31.65°, with 7.2° and 5.84° FWHM, respectively. In the region presented in Fig. 4.5 (b), 3 peaks were found at 47.88°, 53.10° and 62.00° . Only the peaks at 31.65° and 62.00° were assigned to HfO_2 crystallographic planes: orthorhombic (111) and tetragonal (222), respectively. [112]

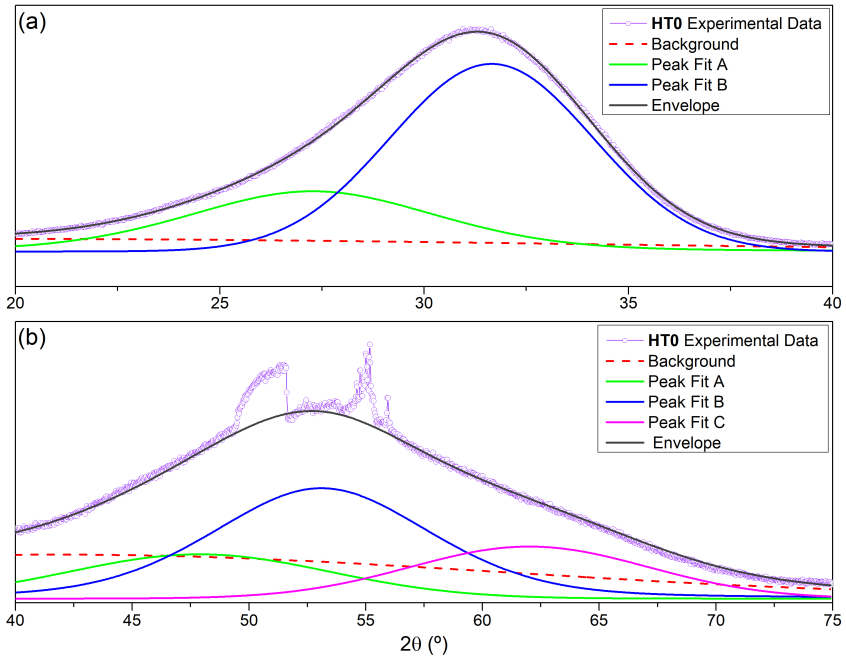

Figure 4.5: Sample HT0, HfO_x individual layer, GIXRD diffractogram of the selected ranges: (a) 20-40° and (b) 40-75°, and respective fitted peaks.

Even though it was possible to associate Miller indices and crystallographic phases to some samples, it does not imply an organized crystallographic structure. These peaks may correspond to local areas with an organized structure, since those are broad and of low intensity. Hence, the analysed samples are considered amorphous. Table 4.1 summarizes the peak information of the GIXRD analysis.

Table 4.1: Resume of the fitted diffractogram peaks, and respectively assign crystal structure, plane and material. Three final peaks of HT0 do not have an uncertainty due to the manual adjustment.

Sample	Peak Centre (°)	FWHM (°)	Crystal structure, plane and compound
SS0.1	22.1 ± 0.2	16 ± 3	amorphous SiO_2
TZ0.1	28.2 ± 0.4	11.7 ± 0.9	rutile (110) TiO_2
	70.1 ± 0.3	1.9 ± 0.3	rutile (301) TiO_2
	70.87 ± 0.06	0.5 ± 0.2	anatase (116) TiO_2
TZ0.2	33.36 ± 0.01	0.89 ± 0.01	hexagonal wurtzite (002) ZnO
	33.96 ± 0.01	0.88 ± 0.04	-
	46.65 ± 0.07	2.3 ± 0.9	hexagonal wurtzite (102) ZnO
	61.76 ± 0.01	2.50 ± 0.09	hexagonal wurtzite (103) ZnO
	66.9 ± 0.1	2.4 ± 0.4	hexagonal wurtzite (112) ZnO
HT0	27.3 ± 0.3	7.2 ± 0.7	orthorhombic (111) HfO_2
	31.65 ± 0.04	5.84 ± 0.06	-
	47.88	13.16	-
	53.10	11.00	-
	62.00	12.00	tetragonal (222) HfO_2

Besides the structure of the deposited films, the nanolaminate system needs to be analysed likewise. It is important to understand if the layers are parallel, individualized, and have the required periodicity. Simply, it is necessary to ensure that the developed multilayer systems are proper nanolaminates. To inspect this, a nanolaminated system with a total of 66 layers was specially designed and analysed through STEM. The bilayer is formed by 3 nm SiO_x and 3 nm SiN_x on top, and repeated 33 times. As discused in Chapter 3, this is a costly technique and the sample preparation is very time consuming, so only one sample was investigated. The PECVD was chosen to deposit such system due to the higher deposition rate and the higher deposition temperature (near 300° C) used in comparison to Magnetron Sputtering. If the layers do not fuse at this temperature, they should also keep its nanolaminate structure when deposited by Magnetron Sputtering (films deposited at RT).

The nanolaminate HAADF STEM image in Fig. 4.6, shows that the layers are separated and do not merge at $\sim$ 300° C. Moreover, the bottom layers display less roughness than the top layers. From the middle up is clear that some sublayers may have higher thickness than 3 nm and some un-homogeneity may occur during the deposition of the upper layers. However, this was observed for thickness higher than the ones considered in the studied nanolaminate systems.

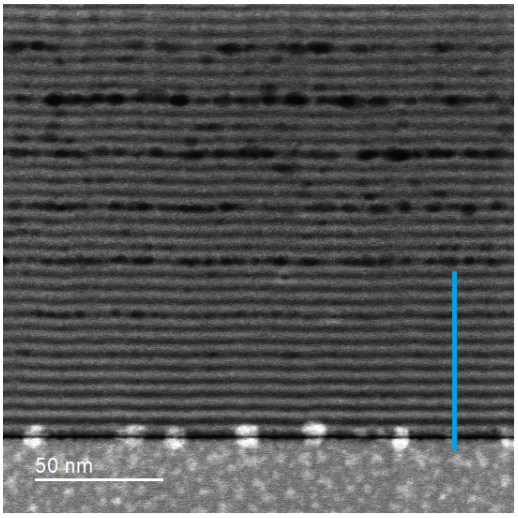

Figure 4.6: STEM-HAADF image of a 33x(3 nm SiO_x + 3 nm SiN_x) nanolaminate. The blue line highlights the region where the EDS linescan region was performed.

Additionally, a STEM analysis with EDS and HAADF was performed. An 80 nm line, perpendicular to the parallel layers, at the right bottom corner, as represented in Fig. 4.6 with a blue line, corresponds to the around 12 bilayers inspected. The HAADF intensity plotted in Fig. 4.7 shows a constant bilayer thickness of 5.2 nm, which reflects the average value of the distance between two consecutive maximums and with a standard deviation of 0.2 nm. Thus, was obtained a 13.6% deviation from nominal value of 6 nm. Note that, as no thickness control occurs during the PECVD and Magnetron Sputtering deposition, differences from the nominal values are expected in the final thicknesses.

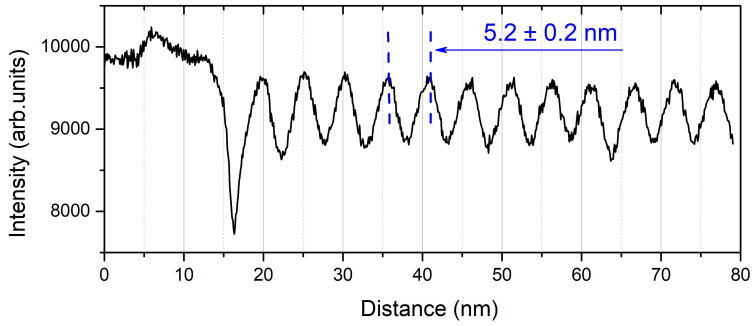

Figure 4.7: HAADF intensity line profile.

In order to understand the elemental distribution in the multilayer system, EDS was perfomed. The normalized O, N, and Si EDS line profiles, presented in Fig. 4.8, reveal the identification of these atomic elements. The EDS line profile was only executed in the $\sim$ 15-45 nm region of the HAADF line profile represented in Fig. 4.7. In the first analysed nanometres a high Si, and no O and N can be observed, which corresponds to the Si substrate of the nanolaminate system. It is clear that the Si content varies, but in general, it has a constant value. The N content has a periodic variation, with distinct maximums and minimums. The period of this variation can be estimated to be around 5 nm, which is in agreement with the value estimated with HAADF profile. Regarding the O content, the line profile should have a similar shape to the N one, with periodic maximums and minimums, although shifted $\sim$ 2.5 nm with respect to the N profile. Meaning that the O maximums correspond to the N minimums, and vice versa. This is expected, since the SiO_x layer should have a higher amount of O and none N, and a SiN_x layer none O and higher N. However, the O content does not have a minimum at $\sim$ 16 nm and 22 nm, where it is expected to exist one. So, these results indicate that the SiN_x may have a O content. This aspect needs to be tackled in more detail since the material may not have the expected composition, which will have an impact on the fundamental properties of the tailored systems containing nominal SiO_x.

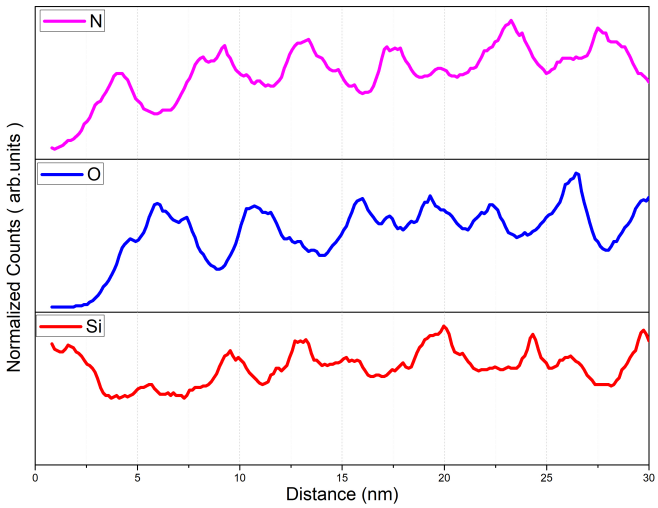

Figure 4.8: EDS line profile for N, O and Si elements for the 33×(3 nm SiO_x + 3 nm SiN_x) nanolaminate.

4.2 Elemental Quantification

The elemental composition of the samples was tentatively quantified through XPS quantification as it is described in Section 3.4.4. A XPS survey spectrum, from 0 to 1200 eV, was acquired for each individual layered sample and selected nanolaminates, to obtain an overview on the sample elemental composition. A representative survey spectrum of sample SS0.1 is presented in Fig. C.1, Appendix C. Then, the C 1s, O 1s, and other expected elements, according to the nominal composition, were acquired, in the respective ranges (see Table 3.7), with high energy resolution. Two sets of measurements were done in these ranges: (1) a Surface one, in which the sample is analysed as loaded in the equipment and (2) a Clean one, with the removal of surface impurities. The surface is cleaned with an Ar gun through sputtering. Afterwards, the obtained spectra were investigated and analysed as follows (using the Avantage 5.988 software):

1. The C 1s spectrum is analysed, in order to inspect the C-C and C-O bonds;

2. The O 1s spectrum information is cross-linked with the one obtained from the C 1s spectrum. If no C-O bond was found in the C 1s spectra, one should not be found in the O 1s range. If a C-O is found in the C 1s, this bond may also appear in the O 1s, and vice versa;

3. To finalize, the remaining spectra must be studied, always based on the latter information. [2]

One remaining aspect regarding the spectrum analysis needs to be considered. The measured spectra can be shifted by a certain energy value. This means that the fitted, and then assigned peaks, may not have the centre equal to the tabulated energy. To determine this constant shift throughout the spectrum, the C 1s spectrum region is fitted, and the deviation of the C-C bond peak centre in relation to the tabulated value, 284.4 eV, is determined. [113, 114] This shift is typically measured in the C 1s spectrum region because is an organic contamination, and is not influenced by the sample. [114] Although measured in C 1s spectrum region, it must be verified in all measured peaks. Such analysis is necessary for the peak identification, but is more important in electronic values determination, in order to avoid erroneous results.

Firstly, the individual layers SS0.1, SS0.2, TZ0.1, TZ0.2, and HT0 were measured, to study their composition. It is expected that SS0.1 and SS0.2 may experience some deviation from the planned stoichiometry, due to possible variations in the plasma reaction. However, samples TZ0.1, TZ0.2, and HT0 should maintain the target stoichiometry, since only an inert gas is inserted in the deposition chamber, and the only material on the chamber is the one removed from the target.

Primarily, the impact of the surface clean procedure on the samples element quantification was evaluated. For that purpose, SiO_x and SiN_x individual layers, on Si substrate, were studied before (Surface) and after the clean process (Clean). Fig. 4.9 (a) and (b) show for sample SS0.1, the O 1s spectrum for Surface and Clean, respectively. While Fig. 4.9 (c) and (d) show the corresponding Si 2p binding energy region. The main difference between the Surface and Clean spectra, when

[2] Note that this analysis strategy is simplest and based on the work developed. A more complex analysis may be necessary depending on the sample's composition and some peaks that may appear (such as oxidation states, Auger transitions, etc.)

looked at a glance, is an area increase observed in the Clean spectra. This occurs because when the surface is clean, a negligible part of the sample is removed trough sputtering. So, the X-rays penetrate with no barriers or contaminations, and the surface resolution is enhanced. Even through, the cleaning procedure was not able to completely remove the C-O bonds in this sample (4.9).

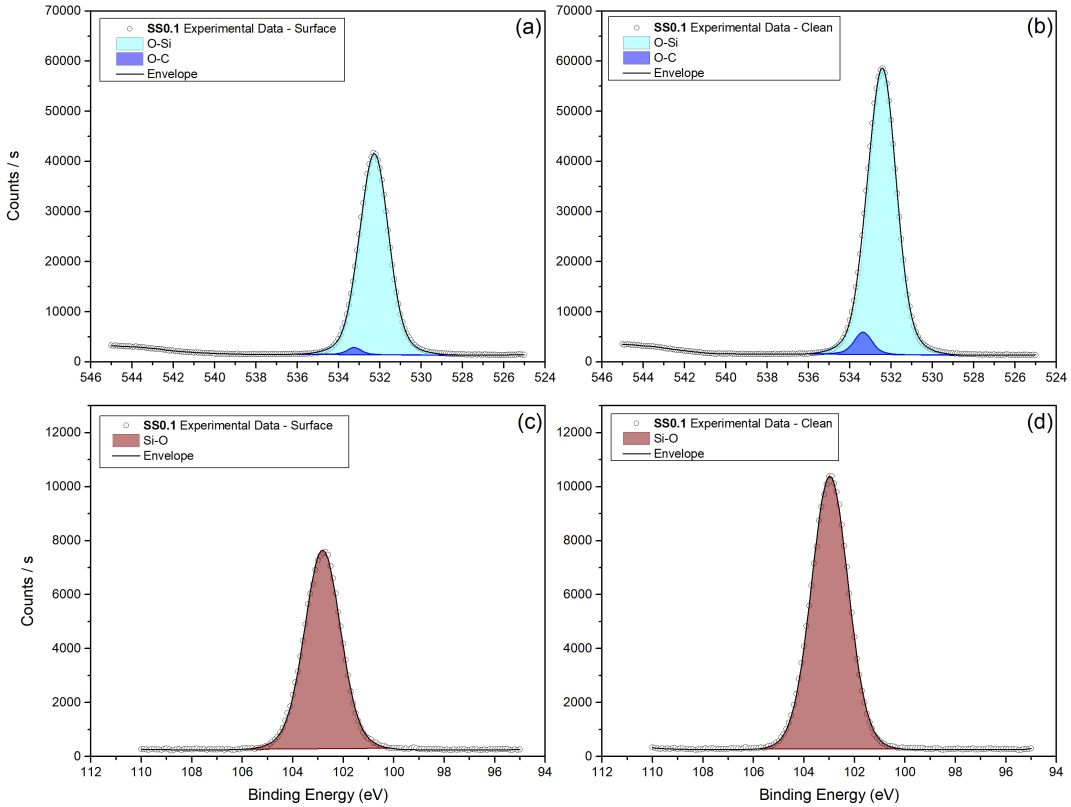

Figure 4.9: As measured XPS spectra of (a) and (b) O 1s, and (c) and (d) Si 2p binding energy regions for Surface and Clean analysis of sample SS0.1, respectively.

Table 4.2: Sample SS0.1, Surface and Clean, elemental quantification.

Element \Substrate	Surface	Clean
O	62.45%	62.36%
Si	37.55%	37.64%

After fitting, the quantification follows Eq. 3.23. Not all fitted peaks were considered, since some are contaminations. Only the O-Si bond peak on the O 1s spectrum, and Si-O for the Si 2p spectrum region were considered for the quantification of Si and O, respectively. The elemental content for sample SS0.1 is presented in Table 4.2. No substantial difference is seen in these values, since the O content is 62.45% and 62.36% for a Surface and Clean analysis, respectively, and the Si content is 37.55% for Surface and 37.64% for Clean analysis. Considering this quantification, the deposited layer is estimated to be $SiO_{1.7}$, when cleaned. Thus, O loss was obtained in comparison to the SiO_2 stoichiometry.

For sample SS0.2, Fig. 4.10 (a), (c), and (e) represent the O 1s, N 1s and Si 2p surface binding energy regions for a surface analysis, respectively, while Fig. 4.10 (b), (d), and (f) show the O 1s, N 1s and Si 2p clean binding energy regions. Comparing (a) and (b) it is noticeable the absent C-O peak after the cleaning and a decrease in O 1s area. From (c) to (d) a slight increase on the N-Si clean bond in comparison to the N-Si surface is observed, and from (e) to (f) no clear change is observed.

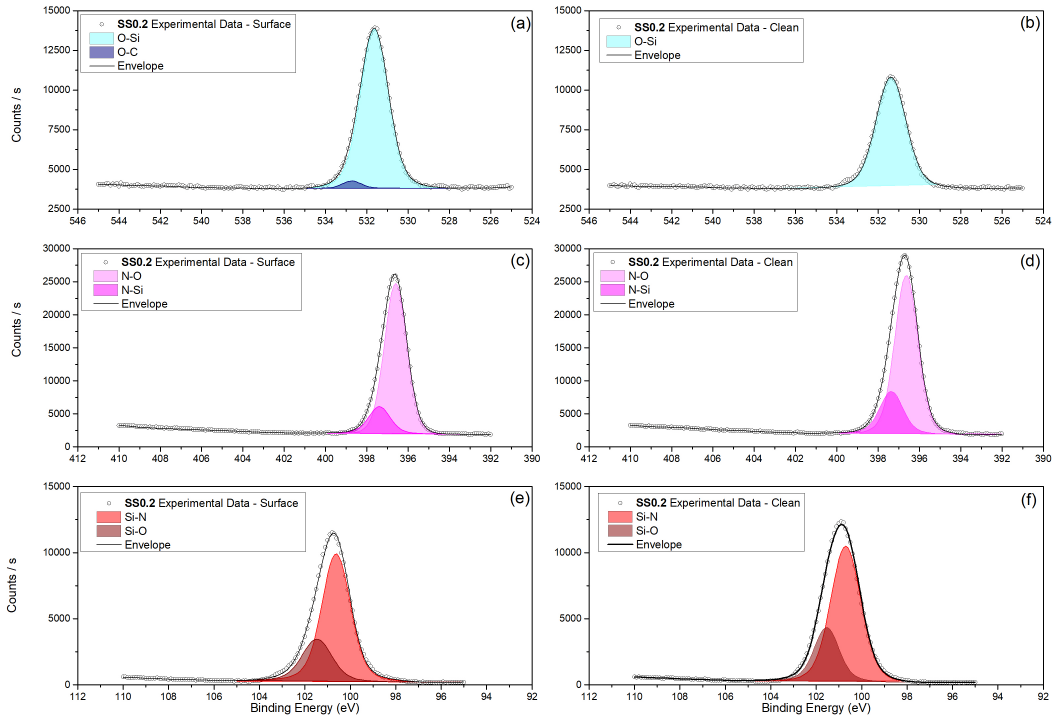

Figure 4.10: As measured XPS spectra of (a) and (b) O 1s, (c) and (d) N 1s, and (e) (f) Si 2p binding energy regions for Surface and Clean analysis of sample SS0.2, respectively.

Table 4.3: Sample SS0.2, Surface and Clean, element quantification.

Element \Substrate	Surface	Clean
O	11.78%	8.08%
N	41.82%	46.10%
Si	46.40%	45.82%

Doing the quantification estimation with O-Si of O 1s spectra, and all the observed peaks in N 1s and in Si 2p spectra, the values reported in Table 4.3 are obtained. It is observed a reduction on O, and an increased content of N, compatible with the observed trend in Fig. 4.10. An approximately 4% variation in the O and N content are noticed, highlighting the clean effect. Sample SS0.2 should be composed of Si and N, nothing else. However, as the sample has a large area O 1s peak, this element was introduced in the quantification. Thus, instead of SiN_x it is SiO_xN_y, where x value is estimated to be 0.2 and y to be 1.0, giving $SiO_{0.2}N_{1.0}$ for the Clean

spectrum. For a better understanding of the high O content and easy comparison with the Si_3N_4 stoichiometry, the x and y can be determined for $Si_3O_xN_y$, giving $Si_3O_{0.5}N_{3.0}$.

As realized with samples SS0.1 and SS0.2, the sample surface cleaning is necessary and has an influence in the quantification values. Another preliminary study was conducted for single layers of TiO_x, ZnO_x, and HfO_x to study the impact of different substrates, Si and SLG. No difference is expected since the deposition conditions are nominally the same. Fig. 4.11 (a) and (b) show sample TZ0.1 O 1s binding energy region in Si and SLG substrate, respectively, and Fig. 4.11 (c) and (d) the Ti 2p binding energy region in Si and SLG, respectively. Doing a simple comparison between (a) - (b), as well as (c) - (d), no clear differences are observed for the sample deposited on Si and SLG. Although, two artefacts were noticed: (1) in Fig. 4.11 (c), SLG substrate at ~472 eV a satellite is observed, which is associated to a charge transition from an O $2p_{eg}$ orbital to a Ti $3d_{eg}$ [115]; and (2) in both substrates, Fig. 4.11 (c) and (d), was identified as a Ti sub-oxide states at low energies. These sub-oxide states are not part of the film, they appear after the Ar gun cleaning. The Ar-TiO_x interaction excites the Ti atoms and produces different Ti-O bonds with lower energies. [116, 117]

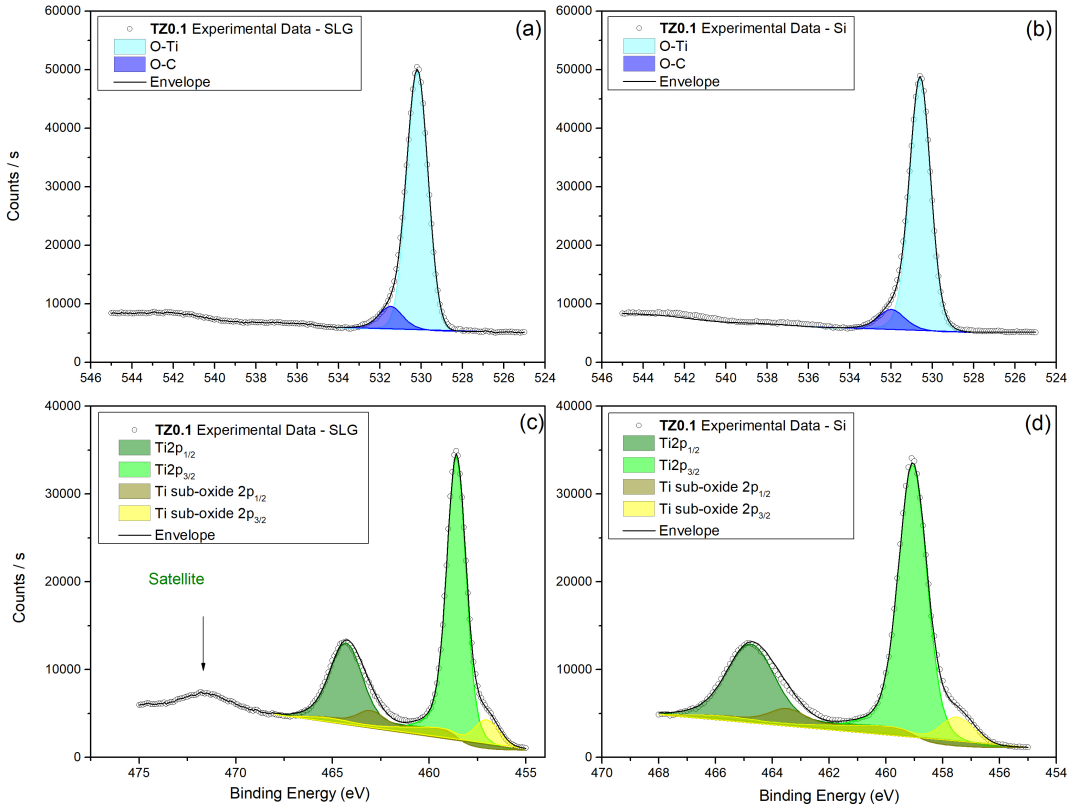

Figure 4.11: As measured XPS spectra of (a) and (b) O 1s and (c) and (d) Ti 2p binding energy regions for sample TZ0.1 on Si and SLG substrate, respectively.

Table 4.4: Element quantification sample TZ0.1, deposited on Si and SLG.

Element \Substrate	Si	SLG
O	67.53%	67.08%
Ti	32.44%	32.92 %

The quantification values, for sample TZ0.1, reported in Table 4.4, are performed with the O-Si peak of the O 1s spectrum and the Ti $2p_{3/2}$ of the Ti 2p spectrum. Only the Ti $2p_{3/2}$, of the Ti 2p spectrum, was considered since is better defined, and because the Ti $2p_{3/2}$ and Ti $2p_{1/2}$ provide similar information. The result shows that when the x value in TiO_x is determined, a small deviation is observed. For Si x = 2.1 and for SLG x = 2.0. This deviation appears to be significant due to round up, but the whole value difference is only $\sim 0.5\%$ on the elements quantities.

Sample TZ0.2 is analysed in Fig. 4.12, where (a) and (b) display the O 1s binding energy region for Si and SLG substrates, respectively. While Fig. 4.12 (c) and (d) displays the Zn 2p binding energy region for Si and SLG substrates, respectively. The most noticeable fact in TZ0.2 spectra, is the intensity of the Zn 2p peaks, in Fig. 4.12 (c) and (d), when compared with the other ones (O 1s, N 1s, Si 2p, Ti 2p or Hf 4f). The peak intensity is one order of magnitude higher, because the Zn $2p_{3/2}$ element RSF value is one order of magnitude higher then equivalent value for the other elements. Also, the Zn peaks in 1010-1055 eV region are much sharper and with a Lorentzian behaviour. For Fig. 4.12 (c) and (d), no clear difference is seen.

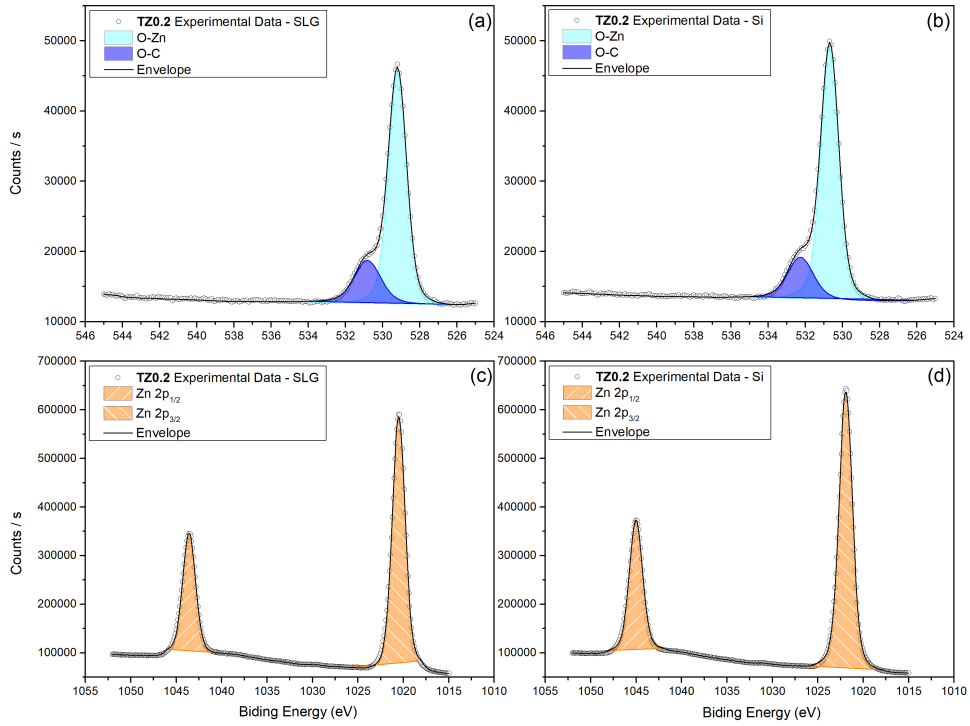

Figure 4.12: As measured XPS spectra of (a) and (b) O 1s and (c) and (d) Zn 2p binding energy regions for sample TZ0.2 on Si and SLG substrate, respectively.

Table 4.5: Elemental quantification sample TZ0.2, deposited on Si and SLG.

Element \Substrate	Si	SLG
O	40.32%	41.38 %
Zn	59.68%	58.62 %

Furthermore, the elemental percentage of sample TZ0.2, reported in Table 4.5, was preformed by fitting Zn2 $p_{3/2}$ on the Zn 2p spectrum, and the O-Zn peak on O 1s. The elemental percentage show mostly equivalent results for Si and SLG, and the x value, in ZnO_x, is determined to be equal to 0.7 for Si and SLG. The considered composition is $ZnO_{0.7}$ which shows lower O content then the nominal value, ZnO.

Finally, the sample HT0 is analysed. Fig. 4.13 (a) and (c) show the O 1s binding energy region for Si and SLG substrates, respectively, and (b) and (d) displays the Hf 4f binding energy region for Si and SLG substrates, respectively. Comparing Fig. 4.13 spectra, (a) with (c), and (b) with (d), no clear difference are noticed.

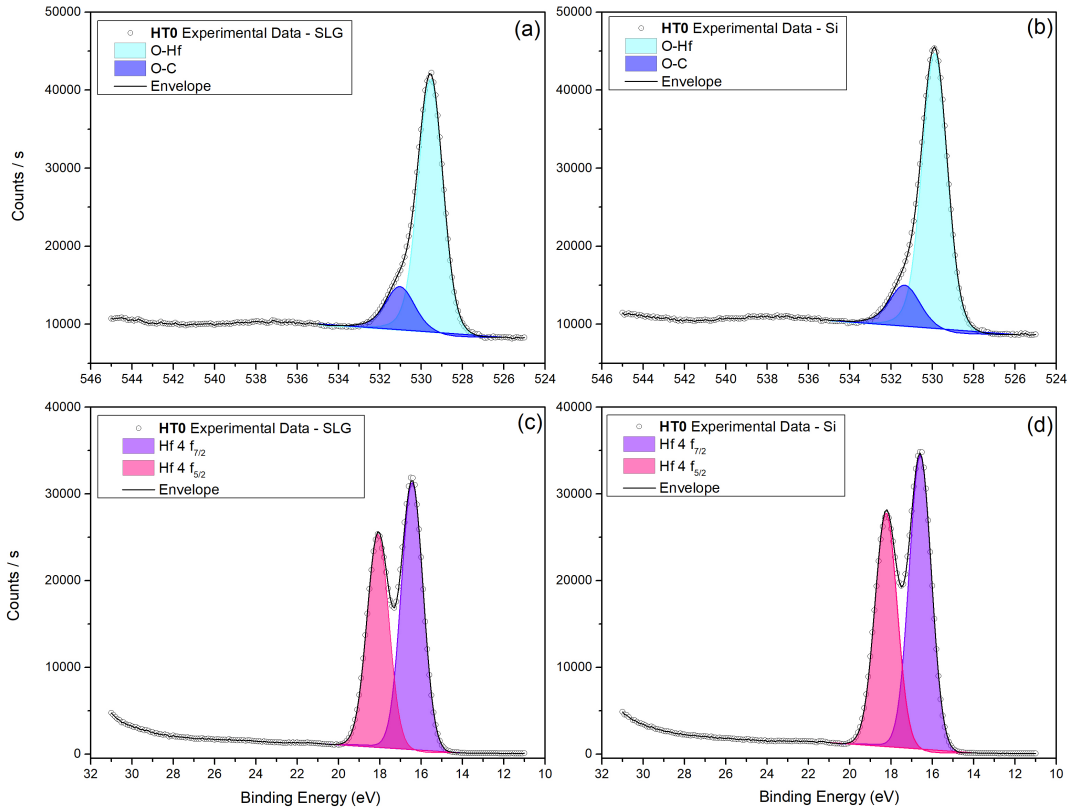

Figure 4.13: As measured XPS spectra of (a) and (b) O 1s and (c) and (d) Hf 4f binding energy regions for sample HT0 on Si and SLG substrate, respectively.

Table 4.6: Elemental quantification sample HT0, deposited on Si and SLG.

Element \Substrate	Si	SLG
O	64.82%	64.9%
Hf	35.18%	35.1%

The elemental quantification of sample HT0, shown in Table 4.6, was preformed with the O-Hf peak on O 1s spectrum and with the Hf $4f_{7/5}$ peak on Hf 4f spectrum. No clear difference is observed, as reported for samples TZ0.1 and TZ0.2, and the x value, in HfO_x, is determined to be equal to 1.8, where O content is lost when compared to the nominal values HfO_2.

From this XPS quantification and simple analogy, is possible to conclude that the cleaning procedure has an effect on the data, and no significant differences were observed when depositing films on Si or SLG. Only the sample TZ0.1, TiO_x, kept the nominal composition as TiO_2. It is important to highlight the importance to study the individual materials to better understand nanolaminate systems. These obtained deviations from the nominal compositions may have an important impact on the latter performance of the nanolaminated systems.

Following the individual layers quantification, it is possible to apply the same XPS approach to the nanolaminate systems, and evaluate their compositions in comparison to the individual layers. Based on the former results, expected values for the nanolaminate systems composition were estimated considering an X-ray average depth of 10 nm. [115] A schematic representation of the top 10 nm of each sample is presented in Fig. 4.14, to guide the interpretation of the nanolaminate systems quantification results.

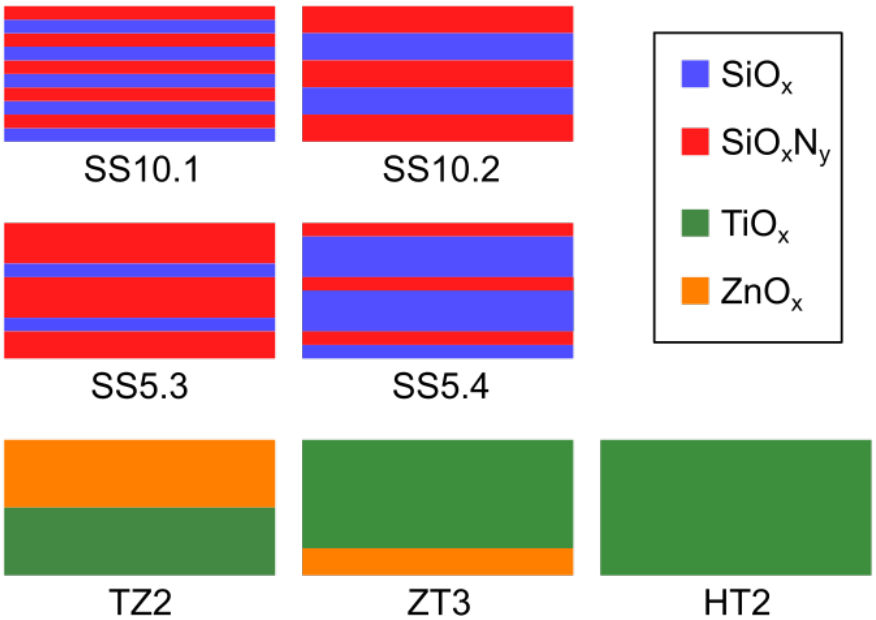

Figure 4.14: Representation of the top 10 nm of samples SS10.1, SS10.2, SS5.3, SS5.4, TZ2, ZT3, and HT2. Based on the existent, complete or incomplete, layers on the top 10 nm, a material percentages can be determine. For sample SS10.1, SS10.2, SS5.3 and SS5.4, the SiO_x/SiN_x are 50%/50%, 40%/60%, 20%/80% and 70%/30%, respectively. For sample TZ2 TiO_x/ZnO_x = 50%/50%, sample ZT3 ZnO_x/TiO_x = 20%/80%, and for sample HT2 HfO_x/TiO_x = 0%/100%.

The nanolaminated XPS spectra of samples SS10.1, SS10.2, SS5.3, SS5.4, TZ2, ZT3, and HT2[3] were analysed with the strategy described before. The SS10.1 spectra can be seen in Fig. 4.15, for (a) O 1s, (b) Si 2p and (c) N 1s binding energy regions. The remaining samples spectra in the regions of interest can be found in Appendix C. Note that for the nanolaminate systems more ranges of binding energy had to be analysed per sample, since each sample is composed of more elements. In SS10.1 O 1s spectra (Fig. 4.15 (a)), is clear the appearance of a new peak, when comparing the samples SiO_x and SiN_x O 1s spectra, corresponding to a C=O bond [118]. This bond was also observed on the C 1s (not displayed). The Si 2p and N 1s spectra (Fig. 4.15 (b) and (c)) show similar peaks as observed in both single layers of the materials that compose this nanolaminate. An equivalent qualitative analysis of the reaming nanolaminated systems XPS spectra can be seen in Appendix C.

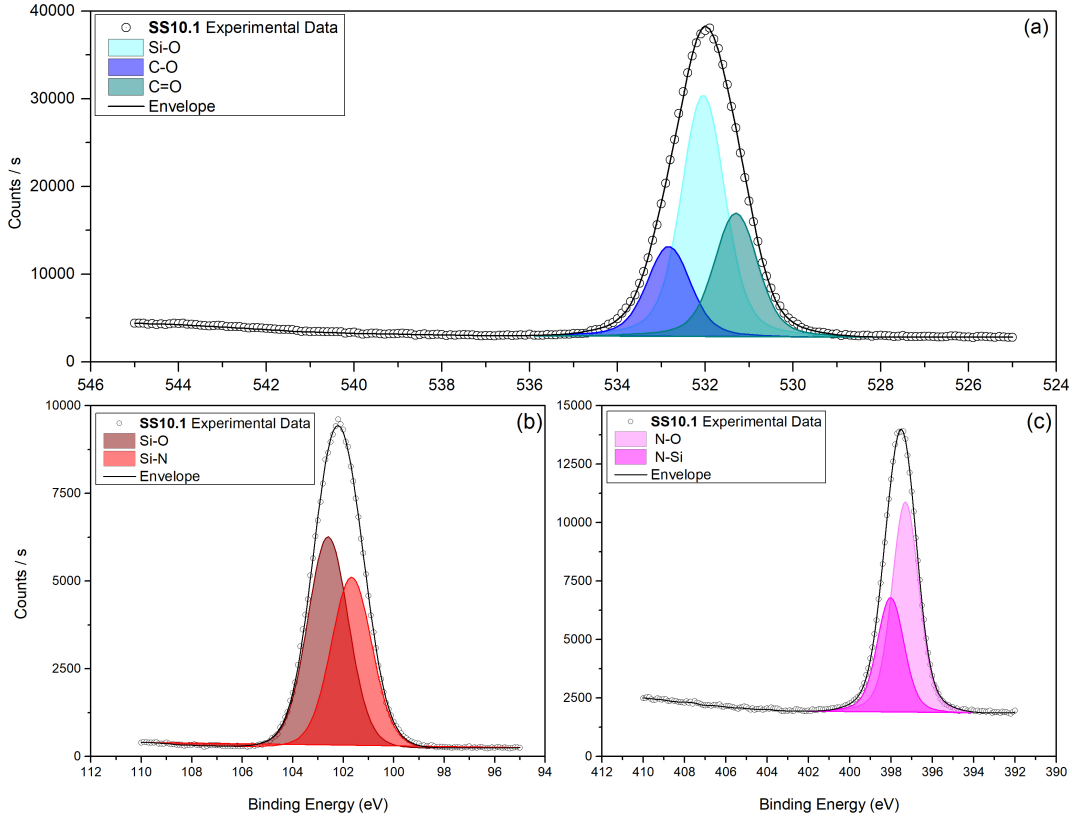

Figure 4.15: As measured XPS spectra of (a) O 1s, (b) Si 2p, (c) Ni 1s binding energy regions for Clean analysis of sample SS10.1, respectively.

[3]The spectra presented correspond to samples in Si substrate and after cleaning with the Ar gun.

Table 4.7: Measured and expected elemental quantification of samples SS10.1, SS10.2, SS5.3, and SS5.4.

Sample	SS10.1		SS10.2	
Element	Measured	Expected	Measured	Expected
Si	47.87 %	41.73 %	47.95 %	42.55%
N	27.44 %	23.05 %	24.62 %	27.66%
O	24.69 %	35.22 %	27.44 %	29.79 %

Sample	SS5.3		SS5.4	
Element	Measured	Expected	Measured	Expected
Si	46.41 %	44.19 %	44.50 %	40.10 %
N	43.51 %	36.88 %	17.80 %	13.83 %
O	10.04 %	18.94 %	37.70 %	46.08 %

Table 4.7 list the experimentally obtained and expected values for the analysed SiO_x and SiN_x based nanolaminates. For all samples, the Si percentage is higher than expected. This may suggest that the X-ray penetration depth is higher than the stated 10 nm. In this case, more layers are scrutinized and the Si percentage increases, since it is the common element in the two compounds. In samples SS10.1, SS5.3, and SS5.4, the N amount is higher and the O is lower then the estimated values. If assumed the above discussed X-ray penetration depth higher than 10 nm, this may explain the composition obtained for samples SS10.1 and SS5.3. However, the SS5.4 composition cannot be explained by this hypothesis, since the following layer to be analysed should be SiO_x. Thus, a lack of control in the thickness value of the sublayers during deposition may explain the aforementioned results.

On the other hand, for sample SS10.2 it is observed a decrease in N and O. Comparing the N and O variations from the excepted values, it may be assumed a competition between N and O during the film deposition, since a N increase leads to a O substantial decrease, but when N decreases, O also decreases by an equal amount. This deficient control over the element composition, in the PECVD deposition, is the most probable cause for the observed deviations. The lower O content on the individual layer of SiO_x, and low N content and high O content on the individual layer of SiN_x corroborate this cause. Also, some NOA's previous studies found an SiO_x film with $x = 1.8$, and a relative high H content, seen in the REELS spectrum, which further confirms this hypothesis.

Table 4.8: Measured and expected elemental quantification of sample TZ2, ZT3, and HT2.

Sample	TZ2		ZT3		Sample	HT2	
Element	Measured	Expected	Measured	Expected	Element	Measured	Expected
Zn	26.65 %	29.84 %	6.00 %	11.94 %	Hf	4.76 %	0.00 %
Ti	10.75 %	16.22 %	29.90 %	25.95 %	Ti	32.94 %	32.43 %
O	62.60 %	53.94 %	64.10 %	62.12 %	O	62.30 %	67.57 %

Table 4.8 presents the elemental quantification of ZnO_x, TiO_2, and HfO_x based nanolaminates. The composition obtained for the TZ2 samples is not explained by considering a sublayer thickness variation in the structure of the nanolaminate or a change in the penetration depth. So, it is considered that the sublayers composition are different from the single layers that compose

this nanolaminate, studied previously. For sample ZT3, the increase in Ti and O, and decrease of Zn can be justified with a decrease of the penetration depth or a higher TiO_x sublayer thickness. Finally, the HT2 shows a reasonable amount of Hf while none should be detected. This can be accounted by the increase of the penetration depth or smaller TiO_x sublayer thickness, when compared with the nominal value. These XPS results show a higher control in the composition when the films are deposited by Magnetron Sputtering, when compared to PECVD, although the results are compatible with sublayer thickness variations from the nominal value, also observed in TEM results for a nanolaminate deposited by PECVD.

4.3 Optical Properties

Succeeding the structure and composition characterisation, the optical properties were studied. This is an important aspect since it is the core property of an optoelectronic device. Regarding CIGS solar cells, the major optical losses are due to light reflection, parasitic absorption and incomplete absorption in the NIR range. To overcome these problems, light management like ARC and texturization, or the introduction of nanostructures can be employed. [46] A simple analysis of the layers and incoming light interaction with Fresnel equations can be performed. [119] It is observed that to minimize the total solar cell reflectance, the designed electron selective contact should have a refractive index of about 2-2.5 at 600 nm, depending on the thickness (30 to 50 nm). For a hole selective contact at the rear, the minimum possible refractive index value at 600 nm should be searched for, to provide high reflectance and minimize the incomplete NIR absorption. These calculations were based on measured optical constants for the CIGS solar cell layers [120, 121, 122], and serve as a base for the refractive index value goal. The extinction coefficient was not considered since the materials used are almost transparent, only exhibiting small absorbance below 400 nm.

The starting point was the optical constants definition of the substrates, Si and SLG. A 725 nm Si and a 2 mm SLG substrate were characterized, to latter being introduced in the samples optical model. The Si layer was successfully modelled by two Lorentz dielectric functions, and the SLG by the Cauchy model, resulting in refractive index of 3.93 and 1.53, at 600nm, with 1.037 and 2.484 MSE values, respectively. The obtained optical constants are shown in Fig. 4.16, side by side with reference values[4]. [123, 124] Since Si is an opaque material, no light is reflected in the back. Thus, no interference occurs in the reflected beam, and no thickness information can be retrieved. Regarding SLG, the material is fully transparent so, many reflections occur and the model becomes complex. Hence, for simplicity and easy fitting, the substrate thickness was also introduced. The determined n values have a small deviation from the theoretical ones. On Si, the major deviation is observed on the extinction coefficient (k) and near the 400 nm value for n. The latter deviation occurs because the ellipsometer is capable of only measuring from $\sim$ 370 nm to 1000 nm. Since, Si has high absorbance in $\sim$ 375 nm and only part of the spectral region is analysed, the software struggles to fit accurately this spectral region. The SLG determined

[4]The optical constants reference values were selected from the available literature to further confirm the optical modelling, and aid the results discussion and data correlation.

optical constant exhibits a difference of approximately 0.02, which suggests good modelling. This difference, although small, can be explained by the different and varied contaminations or element contents that may occur in SLGs.

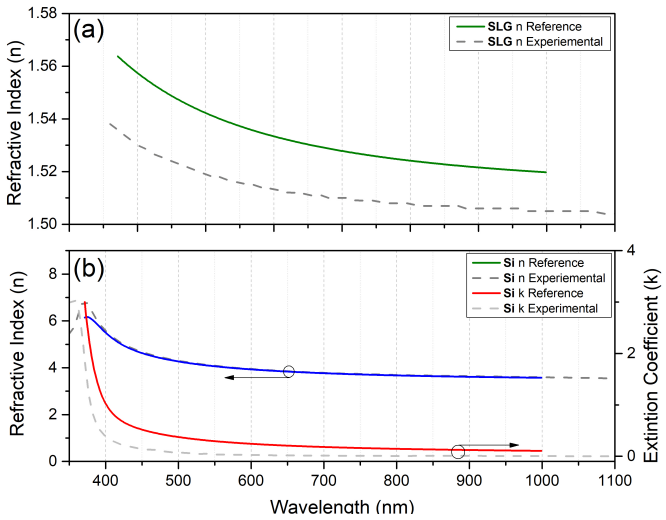

Figure 4.16: Optical constants of (a) SLG and (b) Si substrates, and respective reference values. [125,126]

Subsequently to the substrate's analysis, the individual layers are analysed, providing a basis for the optical properties study in nanolaminates. Fig. 4.17 presents the *n* of sample SS0.1 and SS0.2, individual layers of SiO_x and SiN_x, with reference optical constants for SiO_2 [125] and Si_3N_4 [126]. Samples SS0.1 and SS0.2 were modelled by the Cauchy model, and resulting in a refractive index of 1.95 and 1.48 at 600 nm with MSE values of 2.387 and 4.597, respectively. The measured SS0.1 refractive index dependence on wavelength follows the trend observed for the SiO_2 reference, which is in concordance with the composition result of $SiO_{1.8}$. For SS0.2, the measured and reference Si_3N_4 curves do not match, since the studied sample has a lower N amount and a significant O content. Although, the observed trend suffers an overall decrease in the *n* value due to the higher O content. It is not the clear N content effect the on the refractive index. [127]

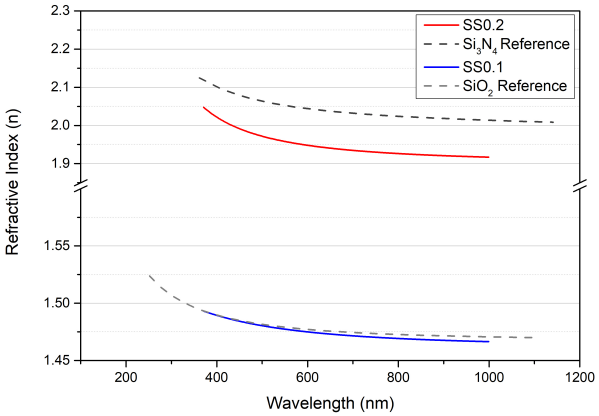

Figure 4.17: Samples SS0.1 and SS0.2, and SiO_2 and Si_3N_4 reference refractive index. [127,128]

Next, samples TZ0.1 and TZ0.2, individual layers of TiO_x and ZnO_x, were also modelled by the Cauchy model, which resulted in refractive index values of 1.91 and 1.87, at 600 nm, with MSE value of 3.031 and 3.660. Despite both materials presenting some absorbance for wavelength values lower than 400 nm, a transparent model was implemented. The chosen model is supported by previous studies present in the literature. [128, 129] Fig. 4.18 shows the obtained optical constants for samples TZ0.1 and TZ0.2, and reference values for TiO_x [130] and ZnO [131]. The experimental *n* curves in Fig. 4.18 show deviations from the reference ones, lower values for TZ0.1 and higher for TZ0.2. The *n* TZ0.1 deviation, from the reference counterparts, it is not expected, since the individual layer characterisation shows a TiO_x stoichiometry. It is known that the deposition conditions determines the materials properties, and in the case of optical properties, the final film density has a big impact. Studies for TiO_x show that changes in the deposition conditions, such as power and gas flow, can lead to different optical constants. [132, 133] Similar to the deposition conditions, different methods can also originate different properties. The reference values correspond to a TiO_2 film deposited by electron beam evaporation, which may lead to a different *n* values. For sample TZ0.2, the *n* deviation corroborates the composition results, since a lower O content was observed.

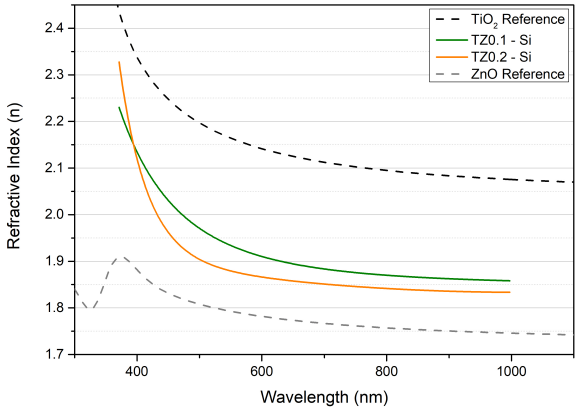

Figure 4.18: Samples TZ0.1 and TZ0.2, and ZnO and TiO_2 reference refractive index. [132,133]

The last individual layer is of HfO_x, sample HT0, which was also characterized by the Cauchy model. Fig. 4.19 shows the final optical constants with a refractive index value of 1.74 at 600 nm and an 8.001 MSE value, and reference refractive index of HfO_2. [134] The MSE value is higher than the ones presented before but acceptable. Recall that for the fitting process, the software generates ψ^* and Δ^* values, based on the input or last interaction determined values, and tries to match the measured ψ and Δ [5]. Besides this higher MSE value, the generated ψ^* and Δ^* values were overlapped with the measured ψ and Δ. From the graphic in Fig. 4.19, it is possible to see that the optical constants of sample HT0 have an approximately 0.2 down shift from the reference data. This deviation was not expected, since, from the XPS results, the samples have a lower than expected O content, which means the *n* should increase and not decrease as it is observed. Although, as mentioned before the different depositions conditions and methods can

[5] If necessary, recall the analysis procedure described in Section 3.4.3

lead to different properties, which was also observed for HfO_2 [135, 136]. Moreover, the reference values used arrived from a film deposited by electron beam evaporation.

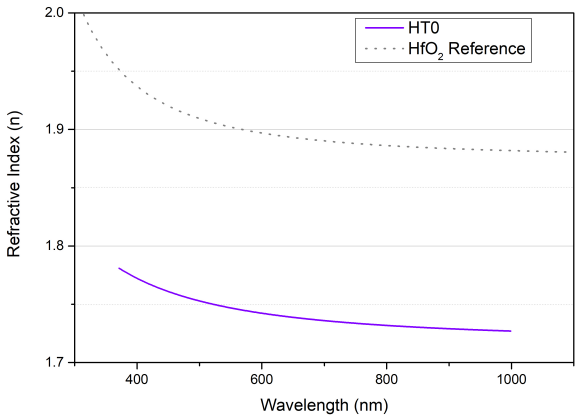

Figure 4.19: Samples HT0 and HfO_2 reference refractive index. [132,136]

The fact that the individual layers do not match the found reference values, reinforces the importance of an initial bulk properties characterisation, before any design or tailoring. Since this step is finished for optical properties, it is now possible to see how the nanolaminated properties vary and how they relate to the individual layers. To determine the nanolaminate optical properties, it was applied the effective medium approximation, where the multilayer periodic system is described as a single layer, in which the effective optical constants can de determined by an weight average, resulting from sublayer thickness times the sublayer repetition. [137, 138, 139] A representation of the effective medium approximation can be seen in Fig. 4.20. The application of the effective medium approximation, allows the ellipsometry optical model to consider one single layer on top of a substrate. For nanolaminates, the Tauc-Lorentz and Cauchy models were used in the optical model. The first one is for nanolaminate samples of SiO_x-SiN_x, and the second one for the remaining samples. As the Cauchy model has the lower degree of complexity it was used to model the individual layers, and the first one to be considered to describe the optical properties the nanolaminate samples. Although, the nanolaminate systems of SiO_x-SiN_x showed high MSE values with this model, so the Tauc-Lorentz was the one considered.

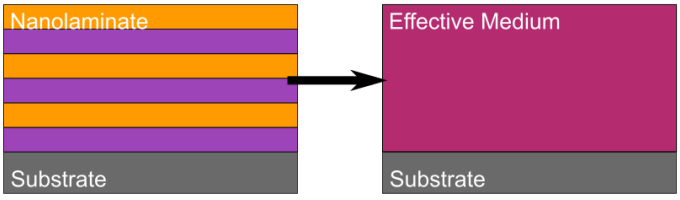

Figure 4.20: Graphical representation of the effective medium approximation, in which a multilayer system can be considered as a single layer.

The first set to be analysed is SiO_x-SiN_x with a 10 times bilayer repetition with different sublayer thicknesses. [6] The optical constants of these samples are represented in Fig. 4.21,

[6] Also, Table D.1, in Appendix D, lists the refractive index, at 600 nm, for all samples, to aid the analysis.

alongside the values obtained for the individual layers. The *n* curves of SS10.1 and SS10.2 show different *n* values, although being design with equal SiO_x and SiN_x ratio. Looking at the XPS quantification results, it was expected that the *n* value of the sample SS10.1 increased since it has a lower O content, than the sample SS10.2. However, this is not what is observed since the SS10.2 refractive index is higher than SS10.1. This may be due to the difference in the N content. For the samples SS10.3 and SS10.4 the one with higher SiN_x, SS10.3, has higher *n* value, and one with the higher SiO_x, SS10.4, has a lower *n* value, compatible with the individual layers trend. Besides some samples do not behave as expected, the MSE values show good fittings.

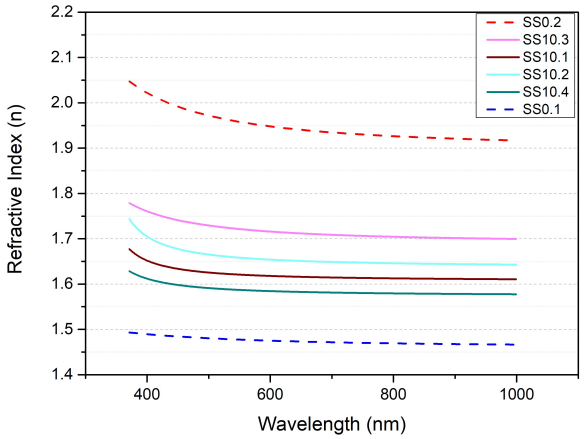

Figure 4.21: Refractive index of the nanolaminates of SiO_x and SiN_x with a 10 bilayer repetition, alongside the individual layers (SS0.1 and SS0.2).

The next set analysed, also of SiO_x-SiN_x, with a 5 times bilayer repetition is shown is Fig. 4.22. The *n* Curve SS5.2 and SS5.4 are overlapped, besides being designed with different SiO_x/SiN_x ratios (2 and 3). This trend meets the XPS composition that shows a low O content in sample SS5.4, which lead to a *n* increase. Similar, the sample SS5.3 *n* value may be more separated from the sample SS5.1 *n* than nominally expected, due to the lower O content experimentally obtained. The MSE values obtained are very close to the unit for all studied samples in this 5 times repetition set.

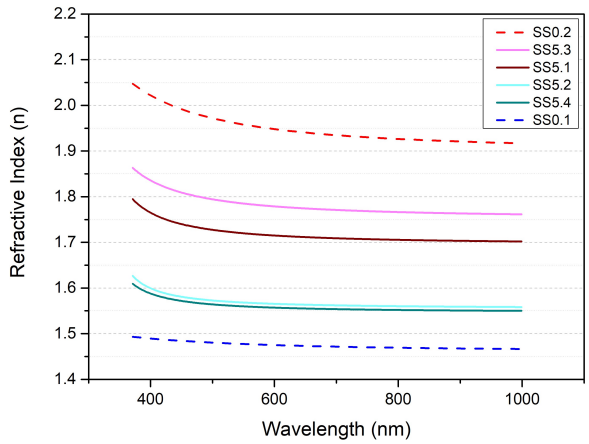

Figure 4.22: Refractive index of the nanolaminates of SiO_x and SiN_x with a 5 bilayer repetition, alongside the individual layers (SS0.1 and SS0.2).

For the TiO_x-ZnO_x nanolaminates portfolio, two sets were studied: (1) nanolaminates in which the bottom layer is TiO_x and the top ZnO_x and (2) nanolaminates with the reverse bilayer order. In both, the sublayer's thickness was varied, but having TiO_x/ZnO_x ratio equal to one or higher. The bilayer order was changed to see which architecture provide the best results since both materials have relatively high conductivity, transparency, and may provide electron selectivity. Fig. 4.23 shows the obtained *n* value for samples TZ3, TZ2, TZ1.1, and TZ1.2, in which the MSE values indicate a good fitting model. A major and important observation is that there are *n* values for the nanolaminates that surpass the values obtained for the individual layers, that compose those systems. While up to now, all sample's optical constants were between the individual layers values.

Firstly, the sample TZ3 has the lowest *n* despite having the higher TiO_x/ZnO_x ratio. Nevertheless, considering the 80% TiO_x nominally in its composition, the *n* is close to the TiO_x individual layer mostly for wavelength values higher than 600 nm. Second, samples TZ2 and TZ1.2, which have equal TiO_x/ZnO_x nominal ratio (equal to 2), have close *n* values and trends. This high *n* value is not expected since the XPS results of sample TZ2 show a lower metal composition, and high O content. The sample TZ1.1, with TiO_x/ZnO_x equal to 1, has an *n* curve almost overlapped with the TiO_x which was not expected considering the effective medium approximation.

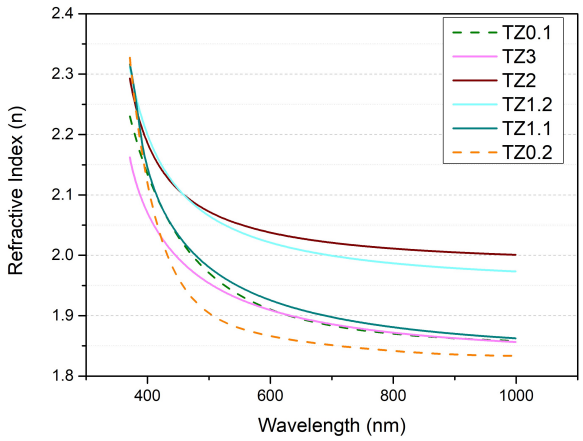

Figure 4.23: Refractive index of the nanolaminates of TiO_x and ZnO_x, alongside the individual layers (TZ0.1 and TZ0.2).

Fig. 4.24, shows the *n* values for the ZT nanolaminates set, of ZT3, ZT2, ZT1.2, and ZT1.1 nanolaminates. The MSE values for these curves are higher than the latter ones, but still show good fittings. Contrary to sample TZ3, ZT3, which has the same TiO_x/ZnO_x ratio, has the highest *n* value, which is compatible with the highest TiO_x nominal content. Moreover, in XPS analysis, its observed a significant loss of Zn and high Ti content, which further justify the high *n* value. Next, the *n* values for ZT2 and ZT1.2 samples should be overlapped. However, its observed a deviation of sample ZT1.2 for lower *n* values in comparison to ones obtained for ZT2, and equivalent nominal ratio TZ2 and TZ1.2 samples, that have close values with a deviation of 0.03. Sample ZT1.1 has equal TiO_x/ZnO_x ratio of samples TZ1.1, and also its observed the same *n* value at 600 nm, 1.94 and 1.93, respectively.

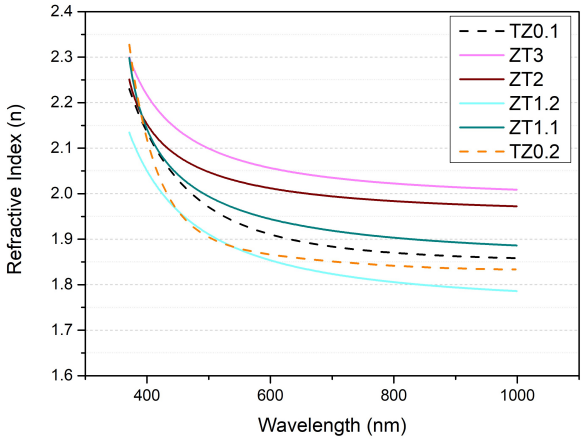

Figure 4.24: Refractive index of the nanolaminates of ZnO_x and TiO_x, alongside the individual layers (TZ0.1 and TZ0.2).

The last set is composed of HfO_x and TiO_x layers. The two nanolaminate systems created have the same HfO_x/TiO_x, equal to 2, and the corresponding *n* curves are presented in Fig. 4.25. The values were obtained with good MSE, 3.83 and 2.73 for sample HT1 and HT2, respectively. For this sample's set, the nanolaminate systems *n* values stay between the individual layer's values. Since sample HT1 and HT2 have the same HfO_x/TiO_x ratio, they should be overlapped. Nevertheless, the difference between the two is small, about 0.03.

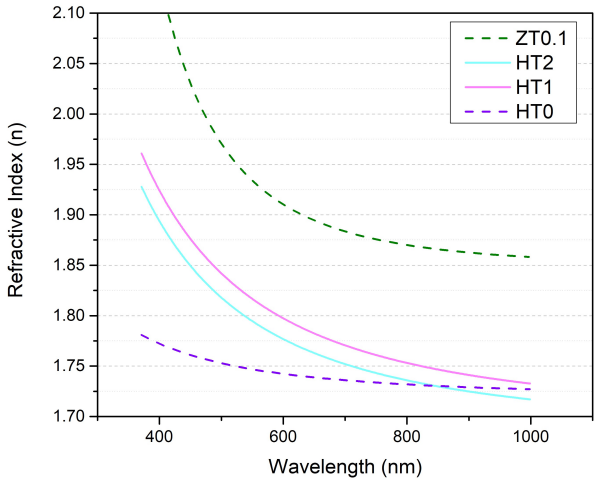

Figure 4.25: Refractive index of the nanolaminates of HfO_x and TiO_x, alongside the individual layers (TZ0.1 and HT0).

As mentioned in Section 3.4.3, to corroborate the optical constants obtained by ellipsometry, UV-Vis-NIR spectrophotometer was used. With the optical constants, obtained by Ellipsometry, the reflectance was determined, and then compared with the curves measured with the spectrophotometer. Fig. 4.26 shows the reflectance values, measured and determined, for six samples with optical constants that do not fit the expected behaviour: SS10.1, SS10.2, ZT1.2, TZ0.1, TZ0.2 and TZ3. Similarly, plots of the reflectance values, measured and determined, for the individual layer samples are presented in Appendix D. It is clear that the measured and determined curves have discrepancies, the fits present an underestimation of the *n* value for all the studied samples. However,

the experimental and modelled curves have an identical trend. Thus, the closer behaviour can be indicative that the model used, described the overall behaviour for all the samples. Regarding the observed discrepancies, two points can be discussed: the sample's thickness and the n value. The thickness used in these calculations was determined by ellipsometry, alongside the optical constants. Although with small uncertainness, those values can be incorrectly obtained if the optical model is not the most suitable. Nevertheless, there is no evidence to support that. Appendix D lists the nominal samples thickness alongside the measured values with the ellipsometer and profilometer. Moreover, the trend and the small deviation between experimental values and the modelled ones, supports the overcome of several nanolaminates n values regarding their individual layers values. Only, these six samples are presented in the scope of justifying the observed misbehaving of some optical constants samples. However, this reflectance and transmittance analysis were performed for all samples, and the major deviation from experimental and modelled values was of 5%, which validates the accurate determination of the optical constants. It can be seen, in all graphics, a small reflectance drop on $\sim$ 900 nm. This artefact, corresponds to the detector swap inside the spectrophotometer.

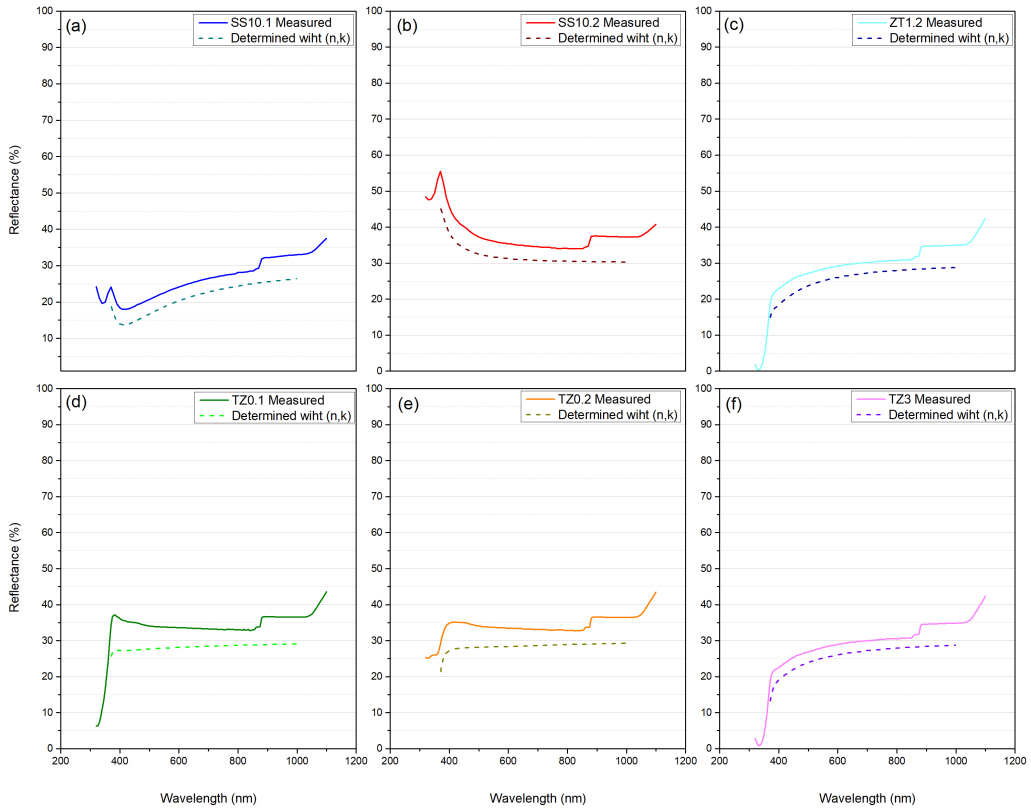

Figure 4.26: Measured and determined reflectance plots, with the measured and determined with optical constants (n, k), for samples (a) SS10.1, (b) SS10.1, (c) ZT1.2, (d) TZ0.1, (e) TZ0.2, and (f) TZ3.

To conclude the optical properties study, it can be said that these vary upon changing the nanolaminate architecture, and that a system can be thoroughly designed to exhibit a specific optical constant value. Although, lack of control in the nanolaminate deposition process may, along with the experimental constraints to obtain the overall nanolaminates composition, lead to the failure of the effective medium optical constant dependence. Considering the integration of the developed nanolaminates as electron selective contacts in CIGS solar cells, several TiO_x and ZnO_x based nanolaminates present n values in the required range.

4.4 Electronic Properties

Knowing the electronic properties is fundamental when designing of selective contacts. As mentioned in Section 2.3.2, is the band offsets between the selective contact and absorber/emitter that block or allow to pass the charge carriers. Hence, an electronic characterisation of the samples created is necessary, to uncover if the chosen materials have an electron or hole selective contact profile, or even neither. The techniques used, XPS, UPS and REELS, were detailed in Section 3.4.4, and the graphical methods used to determine the electronic values are described in Table 3.8.

Fig. 4.27 describes how to outline the samples band diagram with the calculated values. There are no order for the execution of this determination, but Fig. 4.27 shows the process flow of this work, which starts with the E_g determination through REELS, which allows to know the E_V and E_C separation. Then, its determined the $E_F - E_V$ value, by XPS or UPS, to locate the E_F. To finalise, the work function value ($W_F \equiv \phi$) is determined by UPS, which translates the separation of the E_F and the vacuum energy (E_{Vac}) - energy of a free electron.

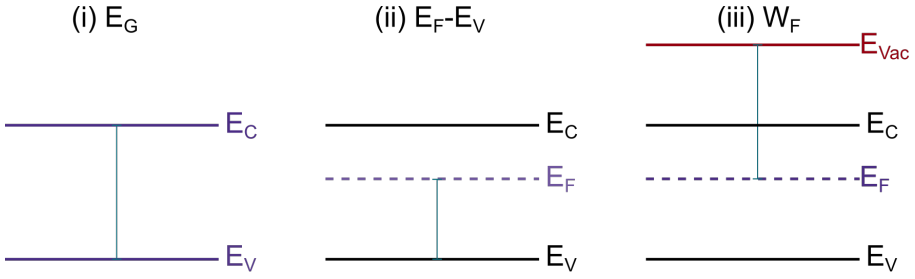

Figure 4.27: Representation of the construction of the band diagram with the measured values. First with (i) the bandgap (E_g) from REELS, then (ii) $E_F - E_V$ from XPS or UPS, and, to conclude, (iii) the work function (W_F) from UPS.

Before presenting or discussing the electronic structure of the studied samples, the graphic methods described in Table 3.8 are exemplified. Fig. 4.28 shows the E_g and $E_F - E_V$ calculation for samples SS0.2 and HT0. Fig. 4.28 (a) and (b) show the E_g determination through the REELS spectra. The complete REELS spectrum is not presented, but it is clear the existence of a maximum at 0 eV. Going to higher binding energies, a small and broad peak can be seen, highlighted with a circle in both spectra, which indicates H in the films. Then, a minimum occurs and afterwards a linear increase in the counts/s is observed, where the linear regression is done and the interception of this fit with the abscissa value corresponds the E_g value. Fig. 4.28 (c)-(d), and (e)-(f) show

the $E_F - E_V$ determination with XPS and UPS, respectively. On these plots, at minimum energies around 0 eV, the counts/s is null. Then, for higher energies, the values of counts/s start to increase, followed by linear behaviour. From the linear regression abscissa value interception, the $E_F - E_V$ value is determined. Moreover, for the XPS $E_F - E_V$ determination, the spectrum energy shift, discussed in Section 4.2, needs to be taken into count. The abscissa interception value must oppositely shifted to provide accurate results. Although with the same information and corresponding to the same band diagram region, the XPS ((c) and (d)) and UPS ((e) and (f)) spectra have different resolutions with may be due to the different incident photons energy.

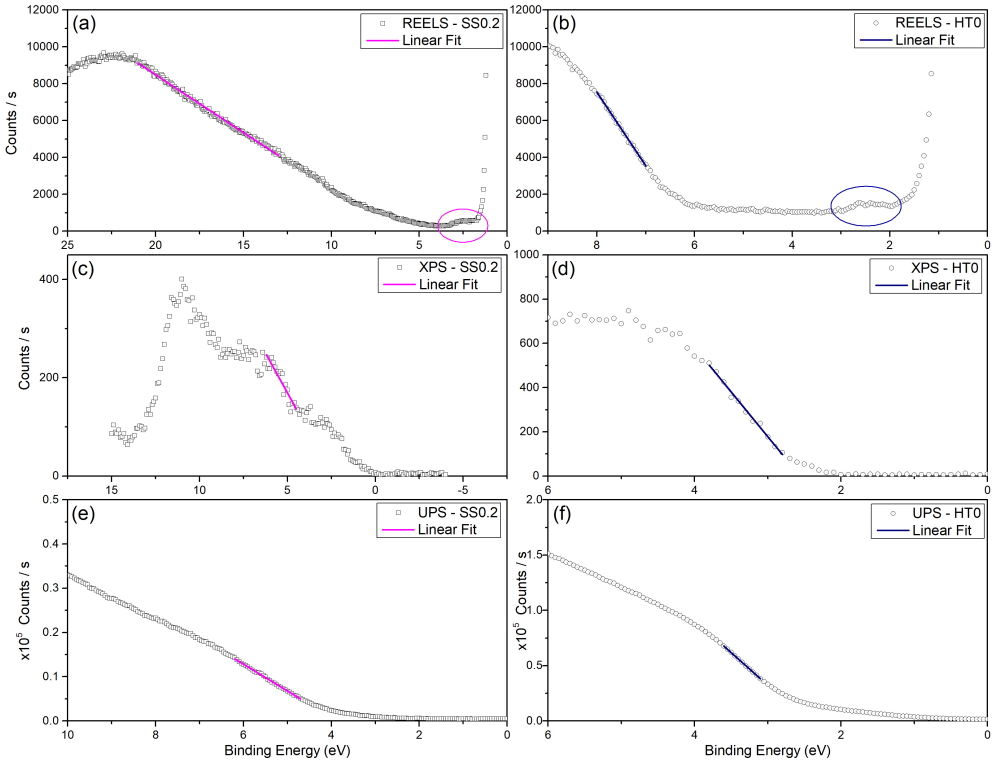

Figure 4.28: Graphical methods to obtain the electronic structure. (a) and (b) are the REELS spectra, (c) and (d) the XPS spectra, and (e) and (f) the UPS spectra of samples SS0.2 and HT0, respectively.

The exemplified determination of $E_F - E_V$ in samples SS0.2 and HT0, with XPS and UPS, shows null counts/s at energies close to 0 eV. Although, this is not observed for all measured spectra as shown by the UPS SS0.1 presented in Fig. 4.29. In these cases, in the determination of $E_F - E_V$ value, this minimum counts/s value, different from 0, needs to be considered. Two step process needs to be tackled: (1) the linear region with zero slope values is fitted in order to determine minimum average value; (2) the $E_F - E_V$ determination follows the mentioned procedure, however the interception is done with the minimum average value, instead, as previously, with the abscissa. In the case sample SS0.1 UPS spectrum presented in Fig. 4.29, it was considered the interception of the linear fit with the 4.78×10^3 value.

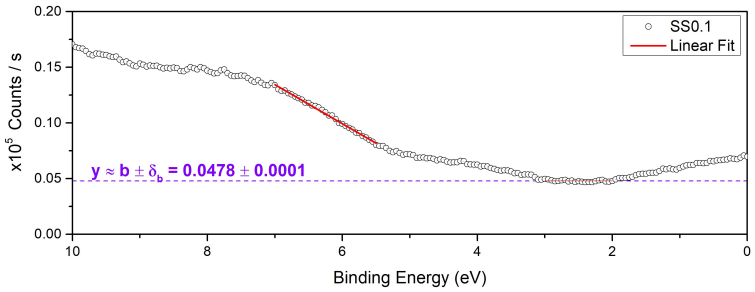

Figure 4.29: UPS spectra of sample SS0.1, where the linear regression interception was not done on 0 counts/s value but on 0.0487 counts/s.

The results of the samples E_g and $E_F - E_V$ values, obtained by REELS, and XPS and UPS, are presented in Table 4.9. To guide the electronic discussion through, reference values for SiO_2, Si_3N_4, ZnO, TiO_2, and HfO_2 from literature are used, and presented in Table 4.10.

Table 4.9: Electronic values (E_g and $E_F - E_V$) and associated uncertainty, calculated by error propagation, determined by REELS, and XPS ans UPS, respectively.

Sample	E_g (eV)	δ_{E_g} (eV)	$E_F - E_V$ (eV)			
			UPS	δ	XPS	δ
SS0.1	8.2	0.8	4.53	0.01	4.9	0.2
SS0.2	6.5	0.1	3.88	0.05	3.4	0.6
SS10.1	5.14	0.09	[7]	[6]	[6]	[6]
SS10.2	5.09	0.07	5.09	0.05	4.9	0.3
SS5.3	5.38	0.08	[6]	[6]	[6]	[6]
SS5.4	7.8	0.2	[6]	[6]	[6]	[6]
TZ0.1	3.98	0.08	3.21	0.05	3.5	0.2
TZ0.2	3.4	0.1	3.02	0.02	3.12	0.09
TZ2	3.47	0.07	3.08	0.03	2.0	0.2
ZT3	4.0	0.1	2.73	0.03	2.6	0.1
HT0	6.1	0.1	2.46	0.02	3.2	0.1
HT2	3.9	0.1	2.36	0.03	2.4	0.2

Table 4.10: Materials reference electronic values, and respective articles from where the values were retrieved.

Material	E_g (eV)	ϕ (eV)	$E_F - E_V$ (eV)	Article(s)
SiO_2	8.00	5.15	3.75	[140]
Si_3N_4	5.30	4.80	2.30	[141]
TiO_2	3.20	5.40	2.00	[142, 143, 144]
ZnO	3.20	4.10	3.00	[145]
HfO_2	5.70	5.00	2.58	[146, 147]

The E_g values for the individual layers, SS0.1, TZ0.2, and HT0, have a value close to what was expected considering the references value from Table 4.10. Sample SS0.2 was expected to have a E_g close to 5.3 eV, if it is consider the Si_3N_4 nominal composition, although the determined values is compatible with the XPS estimated composition of reference $SiO_{0.2}N_{1.0}$. [148] Samples TZ0.1

[7] For this sample was not possible to determine $E_F - E_V$ with UPS or XPS, since no linear behaviour was found.

and HT0 also have a higher bandgap values than the references considered, however lower than 0.8 eV. REELS has a penetration depth of about 2-3 nm, which means for most nanolaminate systems, only the top layer will be analysed. On nanolaminates SS10.1, SS10.2, SS5.3, and SS5.4, the sublayer thickness is less or equal to 3 nm which may justify the obtained results of lower and in between E_g values when compared with the individual layers. In order to understand the obtained E_g values, the effective medium approximation was considered in this samples set. For the E_g values of samples SS10.1, SS10.2, and SS5.3, below the ones of the individual layer values, cannot be explained by the effective medium approximation. On the other hand, for sample SS5.4 with ratio SiO_x/SiN_x equal to 1/3, the effective medium appropriation leads to a 7.8 eV E_g value, which matches the experimental value. In order to understand if the effective medium approximation can describe the REELS E_g values, a special sample of TiO_x and ZnO_x with 1 nm thick sublayer was created (15×(1 nm ZnO_x + 1 nm TiO_x)). It was obtained an E_g of 4.1 ± 0.1 eV, which it is not explained by the effective medium approximation, being closes to the TiO_x E_g value, which is the top layer. Once again, this may suggest a lack of control on the sublayer thickness. For the remaining nanolaminates, the obtained E_g values are close to the one of the top individual layer.

Closer $E_F - E_V$ values were determined by UPS and XPS, excluding TZ2 with a 1 eV deviation. Nevertheless, only XPS will be analysed, due to UPS experimental constraints, discussed later in the text. Looking at the individual layers E_g and $E_F - E_V$, it is possible to establish the materials type conductivity. Since samples SS0.1, SS0.2 and HT0 present a middle gap $E_F - E_V$ value, thus are considered insulators. However, the results of samples SS10.2 points to n-type conductivity. Sample TZ0.1 and TZ0.2 have a $E_F - E_V$ value close to E_g value, translating a n-type semiconductor behaviour. Results of samples TZ2 and ZT3 points a significant loss in the n-type conductivity. Regarding sample HT2, which combines a n-type and an insulator materials, a weak n-type conductivity was achieved. Results of samples TZ2 and ZT3 conductivity are compatible with the lower density of O vacancies in the lattice.[149] On the other hand, samples HT2 gained some n-type conductivity, probably due to the increase of O vacancies, accordingly to XPS results.

At this point, the work function (ϕ) determination is missing. In this regard, two key values are required in order to establish the spectrum region of interest, that goes the Fermi level (E_F) to the cut-off energy. The determination of these regions is not straightforward. Fig. 4.30 (a) shows the UPS spectra of samples SS0.1 and SS0.2, and Fig. 4.30 (b) for samples TZ0.1, TZ0.2 and HT0. Starting with an analysis the cut-off energy, which is characterized by a sharp decrease in the counts/s. Looking to sample SS0.1 and SS.02 spectra in Fig. 4.30 (a), no clear cut-off energy is observed. Nevertheless, if cut-off energy exists, it will be close to 16 eV. Regarding samples TZ0.1, TZ0.2, and HT0 spectra in Fig. 4.30 (b), these may have a cut-off energy at approximately 16.2 eV, for all samples. Regarding the Fermi level values, those should be located at the start of a small plateau at low energies close to 0 eV. Notwithstanding, this plateau was not found in any sample, as seen by the insets figures. The only region that was identified corresponds to the valence band region, where it was determined the $E_F - E_V$ value. Since no Fermi level energy can be found, it is a common procedure to consider 0 eV as the Fermi level, to obtain the work function value. [150] However, by considering the E_F value as 0 eV, the work functions will the same for all samples since the considered cut-off energy are approximately the same for all samples,

which is not compatible with the previously analysed electronic structure. Considering that the cut-off energy is a sharp drop in the counts/s, none of the samples present clearly this behaviour, due to of the small kinetic energy of the electrons, which make its detection very difficult. In order to overcome this difficulty, a small negative voltage on the sample/holder system can be applied to allow the electron sufficient kinetic energy to escape this system. [151] Regarding the Fermi level, its energy value is located between the conduction and valence band in insulators and semiconductors, classes where the samples are included, which is a much difficult procedure when compared to metals. So a metal contact between the sample and the holder must be introduced, in order to facilitate the samples and holder Fermi lever alignment. [151]

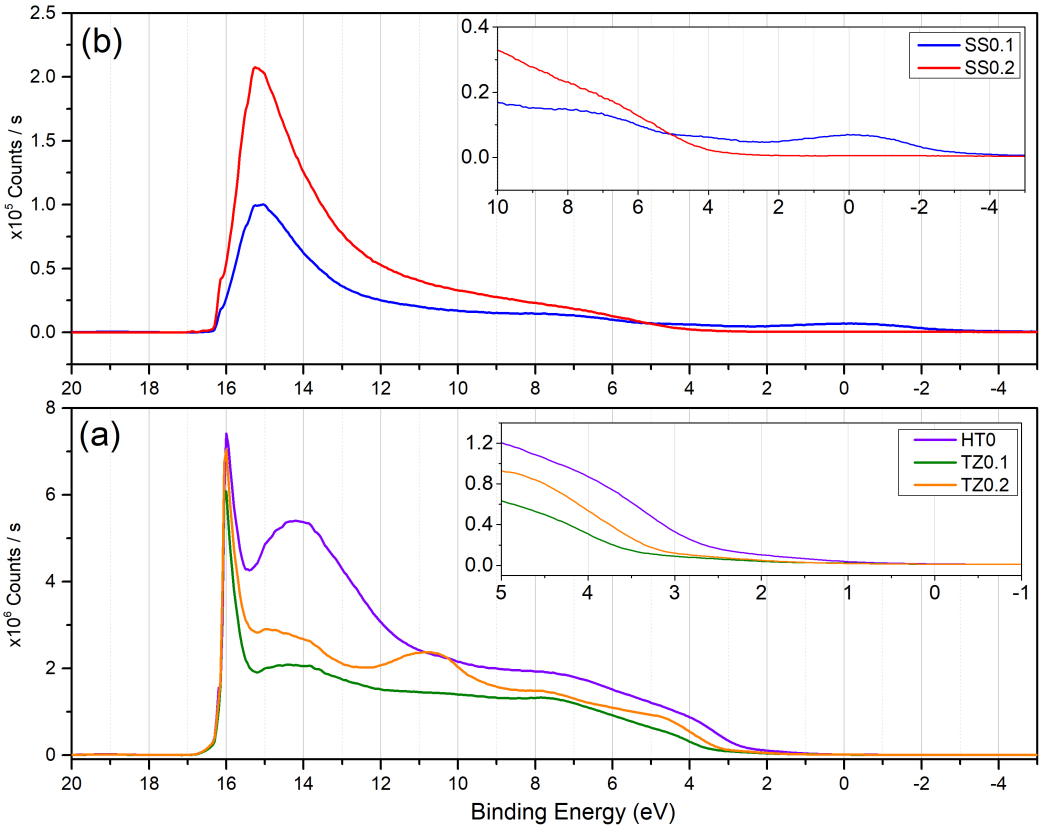

Figure 4.30: Complete UPS spectra of samples (a) SS0.1 and SS0.2, and (b) TZ0.1, TZ0.2 and HT0. The insets represent a zooming in on the binding energy region where the Fermi level plateau should exist.

Thus, an experimental design to study the bias and contact effect on the measurement was implemented: (1) bias dependent measurements with a carbon (C) sampler-holder contact; (2) bias dependent measurements with a copper (Cu) sampler-holder contact. For these experiments the sample ZT2 UPS spectrum was measured at 0, -1, -2, -3. -4 and -5 V. The REELS spectrum was also measured, at 0 eV, allowing a complete electronic structure discussion.

Carbon Contact

On C contact configuration, it was estimated a 4.1 $\pm$ 0.2 eV bandgap value, which is consistent, since it is close to the TiO_x E_g value. The REELS spectrum of sample TZ0.1, not shown, is similar to the ones discussed before. Following, the UPS spectrum was measured at different bias voltages. Fig. 4.31 (a) to (f) show the sample ZT2 for 0 to -5 bias voltage, in -1 increases, respectively. In Fig. 4.31 (a), (b), and (c) no major changes were observed between the spectra. A small redshift with increase of the bias voltage values is seen in the possible cut-off energy region, represented by a vertical line. However, for bias voltages equal to -3 V or higher (Fig. 4.31 (c), (d) and (f)), the cut-off shape clearly appears. Additionally, the cut-off energy redshift between different applied voltages is more significant, and is equal to the difference between bias voltages. Another important point is the increase in counts/s with the bias voltage increase. Since higher bias voltage provides more kinetic energy for escaping electrons, then more electrons are able to be detected.

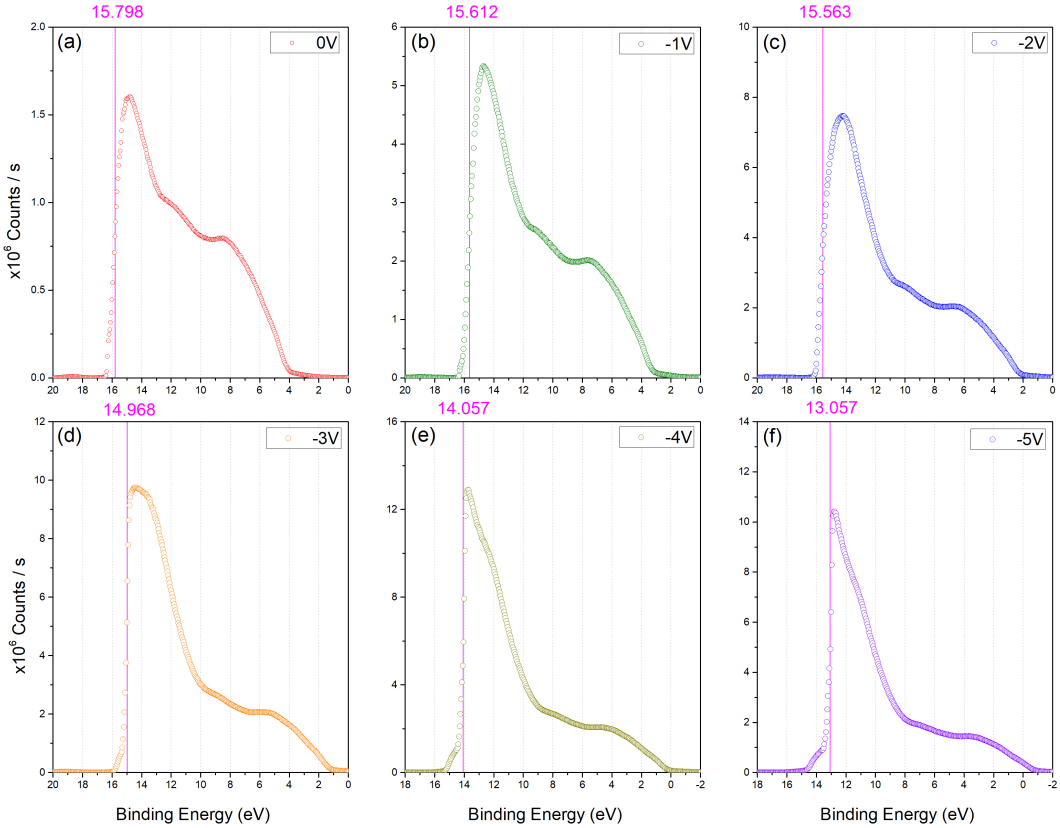

Figure 4.31: Complete UPS spectra of sample ZT2, with the C tape contact,at (a) 0 V, (b) -1 V, (b) -2 V, (b) -3 V, (b) -4 V, and (b) -5 V of bias voltage.

Fig. 4.32 display the valence band UPS region, for all samples spectra in Fig. 4.31, where the $E_F - E_V$ value can be estimated as previously discussed. With increase bias voltage, is once again clear a redshift in the spectra region, and a counts/s increase.

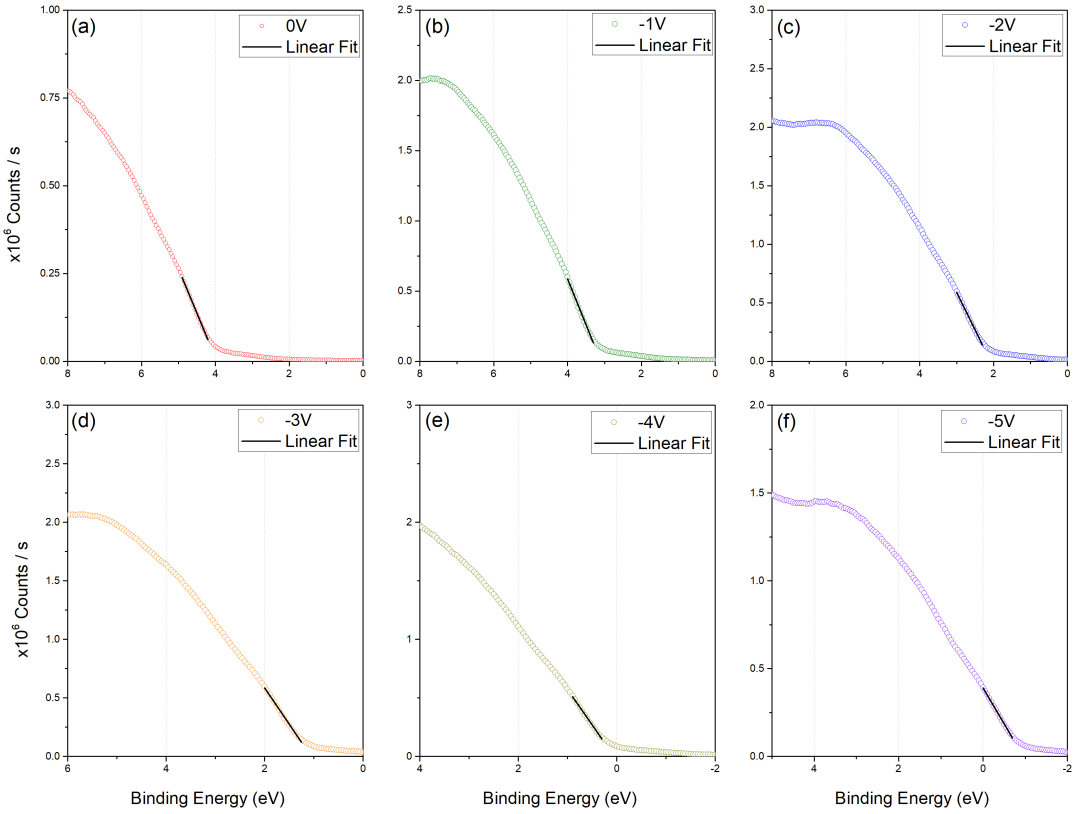

Figure 4.32: Valence band region of the UPS spectra of sample ZT2, with the C tape contact, at (a) 0 V, (b) -1 V, (b) -2 V, (b) -3 V, (b) -4 V, and (b) -5 V of bias voltage.

To determine the work function (ϕ) and the $E_F - E_V$, the applied voltage needs to be taken in account to correct the experienced shift:

$$\phi = h\nu - (E_{cut-off} - Bias) \tag{4.1}$$

$$E_F - E_V = E_0 - Bias \tag{4.2}$$

Here, $E_{cut-off}$ is the cut-off energy, and E_0 it the linear regression abscissa interception. Note that in the ϕ equation the E_F is considered to be at 0 eV.

Table 4.11: Work function ϕ and $E_F - E_v$ and associated uncertainties, calculated by error propagation, determined for the C tape contact at different bias voltages values.

Bias (V)	0	-1	-2	-3	-4	-5
ϕ (eV)	5.40	4.59	3.64	3.32	3.14	3.14
$E_F - E_V$ (eV)	3.96	4.1	4.08	4.06	4.05	4.04
$\delta_{E_F - E_V}$ (eV)	0.08	0.1	0.05	0.04	0.01	0.01

Table 4.11 lists the determined values of ϕ and $E_F - E_V$, for the C tape contact, at different bias voltages. As the applied voltage increases, the ϕ value decreases down to 3.14 eV where it stabilises. This value is considered to be the accurate value. So, for the structural analysis it was considered an E_g of 4.1 $\pm$ 0.2 eV bandgap, $E_F - E_V$ 4.04 $\pm$ 0.01 eV , and ϕ 3.14 eV .

Copper Contact

Following the same procedure for the Cu tape contact, the UPS spectra are presented in Fig. 4.33 (a) to (f) for 0 to -5 bias voltage, respectively. The REELS spectra analysis lead to a E_g of 4.05 $\pm$ 0.09 eV. As observed for the C tape, as the bias increased the overall UPS spectra are redshifted, while the counts/s maximum remains mostly the same, which can be explained by a better contact with the Cu tape.

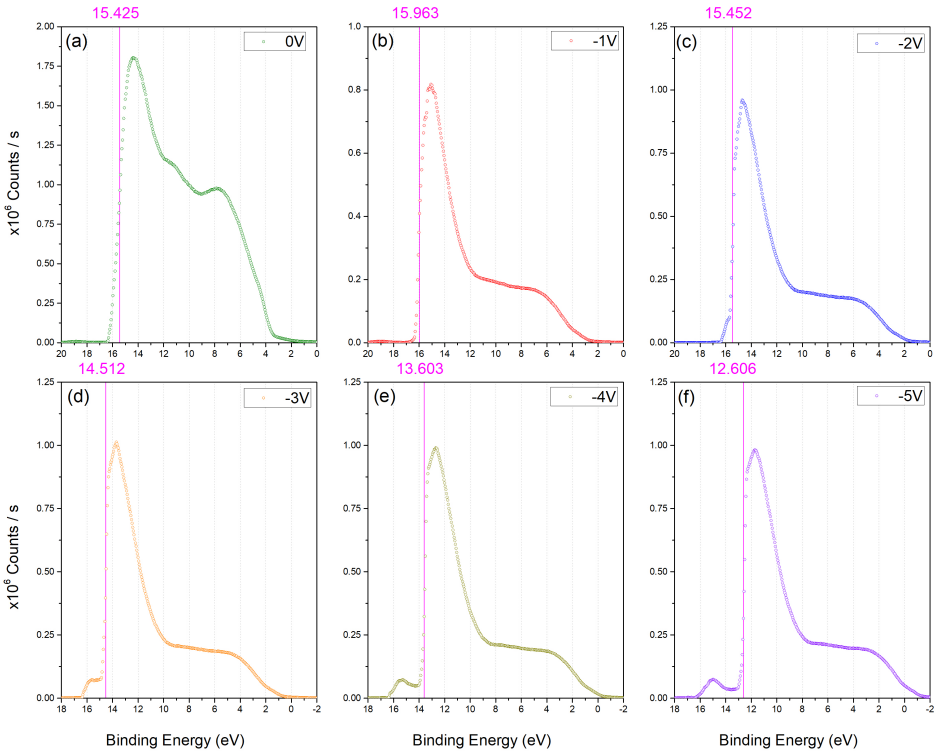

Figure 4.33: Complete UPS spectra of sample ZT2, with the Cu tape contact, at (a) 0 V, (b) -1 V, (b) -2 V, (b) -3 V, (b) -4 V, and (b) -5 V of bias voltage.

Table 4.12: Work function (ϕ) and $E_F - E_v$ and associated uncertainties, calculated by error propagation, determined for the Cu tape contact at different bias voltages values.

Bias (V)	0	-1	-2	-3	-4	-5
ϕ (eV)	5.78	4.24	3.75	3.69	3.60	3.60
$E_F - E_V$ (eV)	3.4	3.52	3.48	3.51	3.48	3.50
$\delta_{E_F - E_V}$ (eV)	0.1	0.04	0.02	0.01	0.01	0.01

Table 4.12 reports the E_g and $E_F - E_V$ determined values with Equations 4.1 and 4.2, respec-

tively, for a Cu tape contact. For this configuration, a ϕ value of 3.60 eV, and 3.50 eV for $E_F - E_V$ value were considered. The final values are different for the configuration with C or Cu tape, but describing a very similar electronic structure, the only difference being the Fermi level energy. All values determined, both in the C and in the Cu configuration, are compatible with sample ZT2 structure since they are close to the estimated values for the individual TiO_x top layer. Regarding the bias voltage, such application it is necessary to determine the end of the UPS spectrum, and then calculate the work function.

Despite the experimental limitations, the electronic structure for a TiO_x and ZnO_x n-type nanolaminate was obtained. Fig. 4.34 compares the band structure from the ZT2 and a CIGS with a bandgap of 1.15 eV [152, 153, 154]. A 1.2 eV conduction band offset was obtained for CIGS with ZT2, which is higher than the aimed value of $\sim$ 0.4 eV, considering the conduction band offset for CIGS with the common buffer CdS layer. [155, 156] On the other hand, a valence band offset of 1.7 eV for CIGS with ZT2 was observed, which meets the goal to block holes.

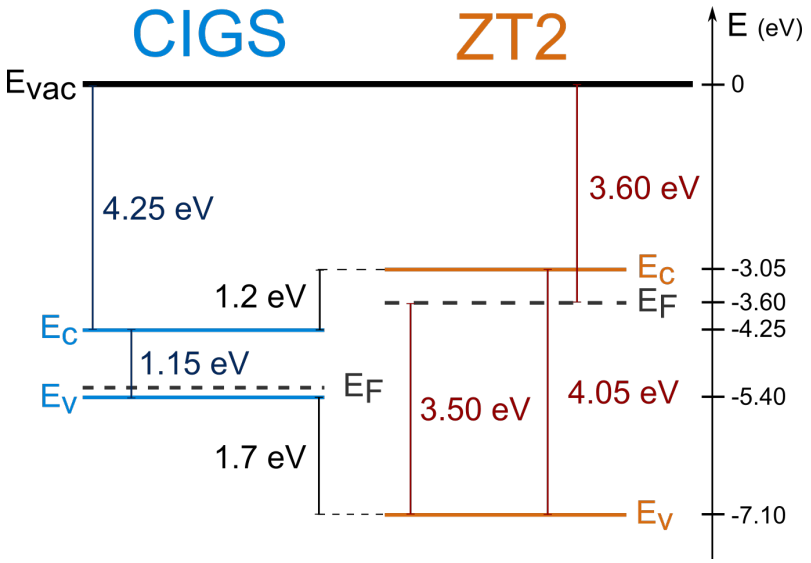

Figure 4.34: Schematic of the band alignment between a CIGS absorber and the sample ZT2. The CIGS Fermi level is considered to be near the valence band since the absorber is heavily doped. CIGS bandgap was taken from [155] and the electron affinity from [156].

4.5 Electrical characterisation

The final characterisation, had the objective of studying how the developed nanolaminates behave under load, and understanding how their integration in a optoelectronic device affects the working standards of the device. Firstly, an analysis was done on metal-insulator-metal (MIM) structures, or simply capacitors, with three different planar contacts: two circular areas and one rectangular, as represented in Fig. 3.4 (c). Through such structure it was possible to observe the samples response to frequency and voltage, and to determine the dielectric constant (k) or relative permittivity (ε_r). Secondly, TLM was employed to determine the samples contact resistance, since when introduced in an optoelectronic device this property will contribute to the device series resistance. At the end, preliminary Admittance spectroscopy studies were done on metal-oxide-semiconductor (MOS) structures to determine the interface passivation capabilities of the developed samples.

4.5.1 Capacitors

The developed plane capacitors had approximately π and $\pi/4$ mm^2 for the circular contacts, and 1.5 $\times$ 20 mm^2 for the rectangular ones, and were done with SiO_x, SiN_x, TiO_x, and ZnO_x single layer and nanolaminate based. The front contacts dimensions match the previous fabricated shadow masks. To study the fabricated capacitors, capacitance analysis was performed. The first part of this capacitors analysis, was focused on capacitance-frequency (Cf) measurements to understand how the materials respond to different frequencies. To measure the capacitance and resistance, a 25 mV amplitude, centred on 0 V and with a frequency f sinusoidal voltage was applied on the capacitor's terminals. Two parameters are measured, since the material is modelled, by the system, as a capacitance in parallel with a resistance. This model can be altered if needed. Fig. 4.35 (a) and (b) show a selected curve for each sample set of, SiO_x-SiN_x, and ZnO_x-TiO_x, respectively. About 36 measurements were done on each sample, to provide good statistics, so a representative curve was selected for each sample. The measurement starts at 10^4 Hz due to the low signal-to-noise ratio (SNR) for lower frequencies, and no tendency can be accurately observed. Also, the capacitance values are presented as capacitance per area (F/m^2), so the different capacitors architecture could be comparable. Regarding the obtained results, all the measured samples have the expected behaviour, in which the capacitance has a constant value until a certain frequency, when it starts to decrease. [157] This observed decrease is related to dielectric losses, and multilayer structures can present increased losses due to charge accumulation on the interfaces. [158] Thus, it may be expected that samples with more sublayers, hence more interfaces, would experience a strong capacitance decrease. However, the nanolaminates capacitance dependence on frequency is not straightforward. Nevertheless, some trend is observed in Fig. 4.35 (a), for frequencies higher than $\sim 5\times10^5$ Hz, the nanolaminates capacity values are lower than the single layers values. Another important observation is that when the nanolaminate presents higher capacitance for low frequencies than the single layers ones, those witnesses a sharp decrease in the capacitance for lower frequency values ($\sim10^5$ Hz). Fig. 4.35 (b) shows the capacitance for

the TiO_x and ZnO_x samples. In this set, samples with only two layers experience the decreasing at $\sim 10^6$ Hz, and the samples with 4 and 6 layer at $\sim 2\times10^5$ Hz. So, it seems that as the number of layers increase, the frequency at which the dielectric losses start to have an impact is lowered. This can be related to the sublayers thickness, since the total thickness was constant at 30 nm. The capacitance values in the constant regime of the Cf curve, will be crosslinked with the capacitance-voltage (CV) analysis, although both results are in concordance.

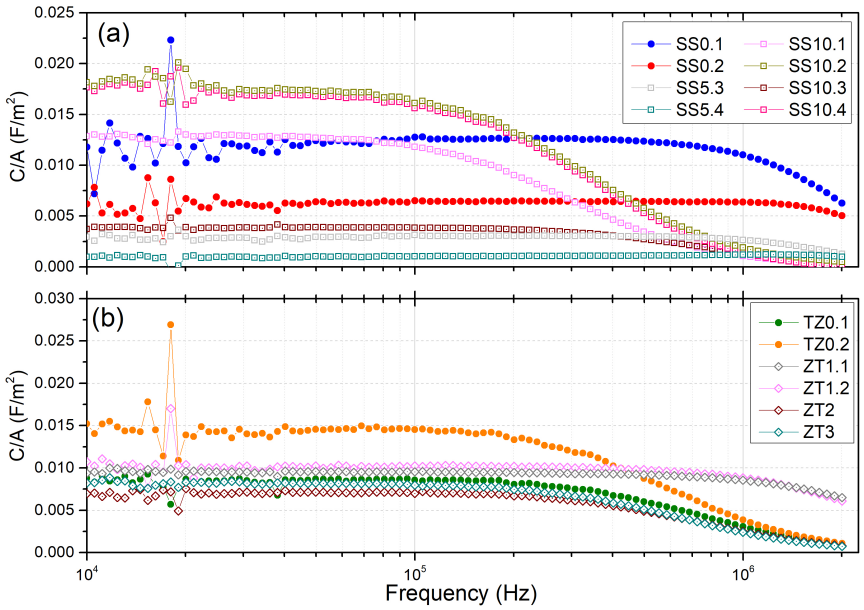

Figure 4.35: Capacitance curves dependence with frequency of (a) SiO_x-SiN_x, and (b) ZnO_x-TiO_x samples set.

Right after each Cf measurement, the CV was carried out, so that both would be done on the same regime. Is expected to observe no capacitance dependence with voltage, since the measurement is done at a constant frequency of 1010^{-5} Hz. [159, 157] Fig. 4.36 presents the CV data of sample TZ0.1, measured on a rectangular contact. As can be seen, no voltage dependence exists since the linear regression as a slope value of $3.814\times10^{-5} \pm 4.5\times10^{-5}$ F/m^2·V, and the sample capacitance per area (C/A) is given by the linear regression intercept value (b) equal to $0.01200\pm 3\times10^{-5}$ F/m^2. Then, the relative dielectric permittivity (ε_r) is determined through the capacitance equation: $C/A = \frac{\varepsilon_r \varepsilon_0}{d}$, where ε_0 is the vacuum permittivity, and d the capacitor/sample thickness. The calculated average values of C/A and dielectric constant are presented in the following Table 4.13 and 4.14.

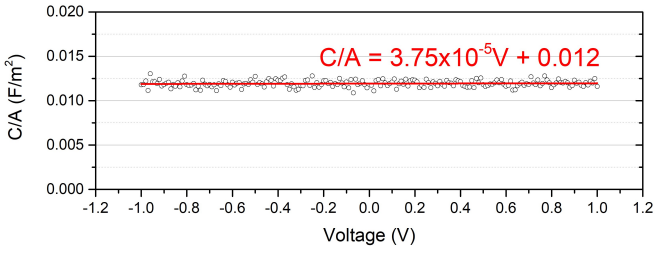

Figure 4.36: Representative capacitance-Voltage curve of sample TZ0.1, for a rectangular contact.

Table 4.13: Capacitance per area (C/A) and relative dielectric permittivity ε_r average values and respective standard deviation, σ_C and σ_{ε_r} respectively, of SiO_x-SiN_x samples set.

Sample	SS0.1	SS0.2	SS10.1	SS10.2	SS10.3	SS10.4	SS5.3	SS5.4
C (A/m^2)	0.0064	0.011	0.006	0.019	0.005	0.018	0.0030	0.0012
σ_C (A/m^2)	0.0007	0.005	0.002	0.007	0.002	0.007	0.0006	0.0002
ε_r	21.8	38.3	19.7	65.6	17.7	59.8	10.4	4.0
σ_{ε_r}	2.2	17.4	7.3	22.6	5.8	24.1	2.1	0.7

Table 4.13 presents the C/A and ε_r for SiO_x-SiN_x samples set. The determined ε_r values of the individual layer samples, SS0.1 and SS0.2, 21.82 and 38.25, respectively, are sufficient differently to what was expected, 3.9 for SiO_2 [17] and 6-7.5 for Si_3N_4 [160]. Although, since the materials do not have the nominal composition, the variation may be justified. Experimental results for SiO_xN_y show a ε_r value between 5-34. [161] Considering the dielectric constant enhancement mentioned in Section 2.2, high ε_r values were expected for the nanolaminate samples when compared with the individual layer. Nevertheless, this is not observed. Almost all nanolaminate samples suffer a decrease in ε_r. The ones that do not, have a high standard deviation which makes a doubtable value. Also, if the sublayers are considered as individual capacitors, and the multilayer system as a series capacitors, is possible to determine the capacitance of the system, knowing the individual layer dielectric constant. However, performing this calculation leads to values between the individual layers ε_r and not to the lower ones measured. This can be justified by the lack of control in the materials composition, shown by XPS, or problems with the measuring approach.

Table 4.14: Capacitance per area (C/A) and relative dielectric permittivity ε_r average values and respective standard deviation, σ_C and σ_{ε_r} respectively, of ZnO_x-TiO_x samples set.

Sample	TZ0.1	TZ0.2	TZ1.1	TZ1.2	TZ2	TZ3
C (A/m^2)	0.010	0.015	0.008	0.010	0.006	0.0069
σ_C(A/m^2)	0.002	0.009	0.004	0.002	0.001	0.0006
ε_r	34.2	50.12	28.7	34.2	21.4	23.4
σ_{ε_r}	7.3	31.03	12.8	5.9	3.3	2.0

For samples based on TiO_x and ZnO_x, Table 4.14 lists the obtained values. Once again, individual layers, TZ0.1 and TZ0.2, with 50.1 and 34.2, respectively, do not have the expected values, 10.4 for ZnO [162] and 95 for TiO_x [17]. Also for these samples, if the series capacitors consideration is applied, the calculated do not lead to the measured values.

High standard deviation values for the capacitance and ε_r were obtained. Several measurements were done, for each sample, and the discrepancy between the measured values was high. Although, the curves had the expected and similar behaviour between devices in the same samples, the measured capacitance values were significantly different. It was also observed that the values are more stable on the rectangular contacts. Theses overall results may be attributed to the difference in the contact areas, since the circular contacts are much smaller than the rectangular one, and non homogeneities in the film could have a bigger impact, when analysed by smaller contacts, which makes the circular capacitors mores unstable. Also, the current may not have the desired vertical flow below the contact, and having also some lateral flow, which may lead to less accurate

values due to differences in the capacitors area. One new approach could be the development of capacitors with the same contact structure, with an additional lithographic process to shape the samples to the contact area. This way the capacitors have the desirable area, and there is no lateral current flow.

Furthermore, the leakage current can be obtained from the CV measurements, since the parallel resistance of the material is also measured alongside the capacitance. By simply applying the Ohms law, the leakage current with voltage can be determined. Fig. 4.37 (a) and (b) represents the leakage current for samples based on SiO_x-SiN_x, and TiO_x-ZnO_x, respectively. The results show lower leakage current for the nanolaminate sample than the individual layer, with the exception of sample ZT1.2. In Fig. 4.37 (b), it is shown that the samples with more TiO_x content have lower leakage current. In Fig. 4.37 (a) no similar correlation could be found. This lower leakage current indicates an increased resistance, which is compatible with more interfaces. Nevertheless, these correlation between the number an interfaces and leakage current could not be studied through these simple analysis. Hence, the TLM method was used.

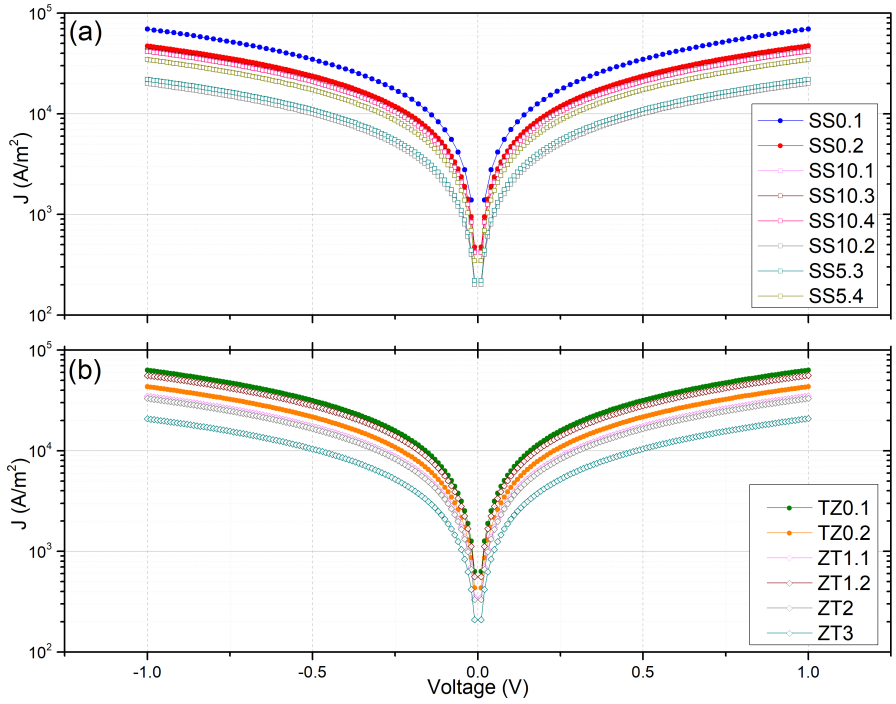

Figure 4.37: Leakage curves, obtain with the capacitance and resistance in parallel model, of samples (a) SiO_x and SiN_x samples, and (b) ZnO_x and TiO_x.

4.5.2 Transfer Length Method Devices

Single layers TiO_x and ZnO_x TLM devices were first fabricated on SLG substrate, so that they be electrically isolated, following the architecture represented in the Fig. 3.4 (a). The measured current-voltage (IV) curves for TiO_x did not behave as expected. No tendency was observed, as the curves for all two adjacent contacts have a linear slope close to zero. Also, the current measured had a significantly low value that may be influenced by the electric circuit noise current. On the other hand, for the ZnO_x film it was possible to perform meaningful IV curves. Fig. 4.38 shows

the obtained IV curves for the four different layouts described in Table 3.4. These measured curves have the expected behaviour, since they are linear and the contact spacing increase leads to a slope decrease. Also, between the four different configurations, the IV curves for the same contact spacing seem to present identical linear slope values. Throughout Ohms law, the total resistance for each curve (R_T) over contact distance (d_i), for each configuration, can be done to retrieve the electrical parameters.

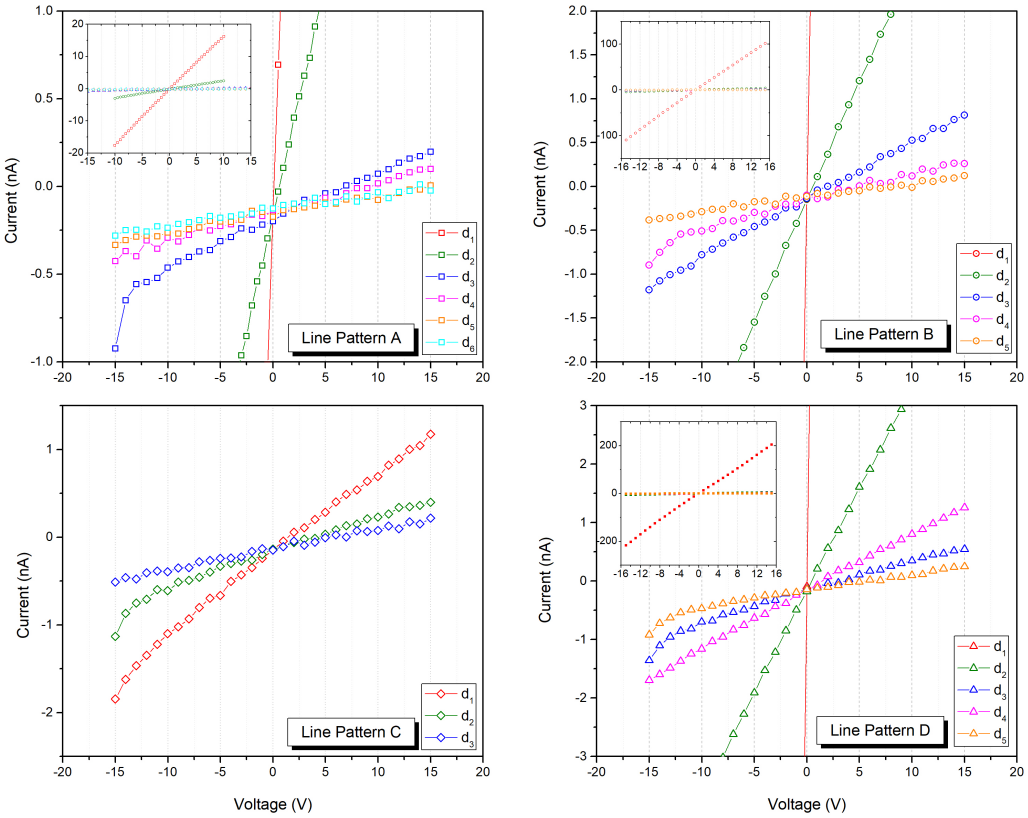

Figure 4.38: TLM IV curves for ZnO_x, for all four configurations: line pattern A, B, C, and D.

Fig. 4.39 shows the obtained R_T *vs* d_i curves for the ZnO_x individual layer, and although they present approximate abscissa interceptions, the slope values are significantly different. Moreover, the ordinate (R_T) interception should be positive and the abscissa (d_i) negative. The latter results are not explained by the considered model framework, raising possible constraints in the TLM conception. In order to understand and optimize the TLM architecture, first, the metallic contacts were deposited on a Si substrate to calculate Si contact resistance and sheet resistance. It was found that similar to TiO_x film, no tendency could be observed. However, the curves did not follow the expected behaviour. This difference in positive and negative bias polarity current suggests that some electronic asymmetry should exist, which was blocking the charge transport. So, it was assumed that the native SiO_x layer, although thin, could be responsible for this effect. To test this latter assumption, the same architecture was employed. However, the contacts deposition, the native oxide was remove from the Si substrate surface by a etch on an anhydrous hydrofluoric acid

(HF) and alcohol vapour atmosphere for 20 min. The measured IV curves for latter Si devices are presented in Fig. 4.40. The curves have perfect linear behaviour, and as the contact spacing increased the curve suffers a decrease in the slope value. This is observed in all four configurations. An important point, is the current saturation at $\pm$ 10 mA. This is not a physical phenomenon, but the current limit detection value set on the system.

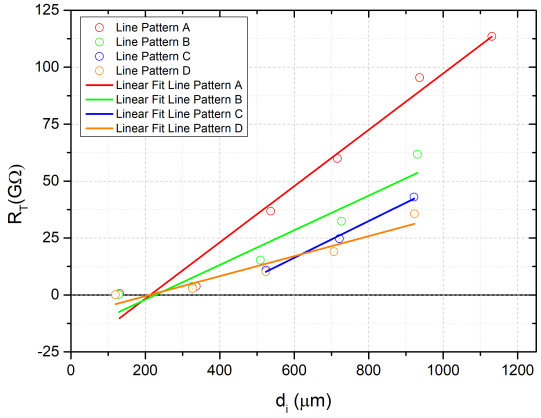

Figure 4.39: TLM R_T *vs* d_i plot, for the ZnO_x film.

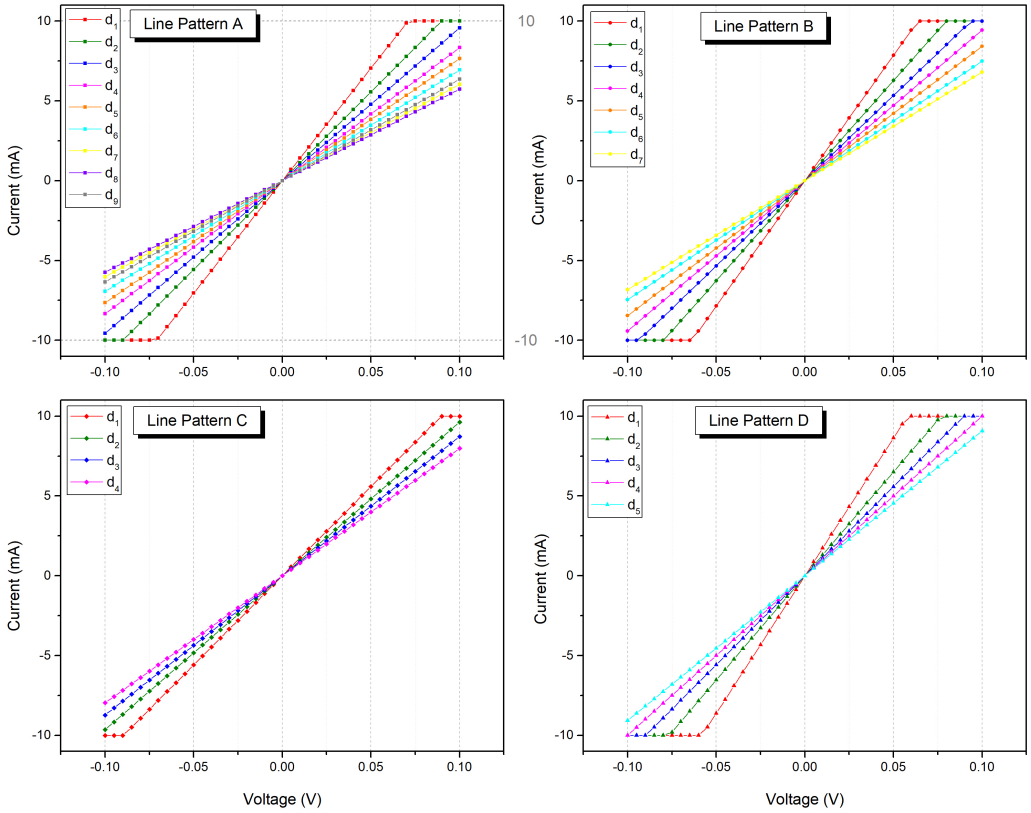

Figure 4.40: TLM IV curves for Si, for all four configurations: line pattern A, B, C, and D.

Considering the Ohms law once again the R_T can be calculated, and plotted against the contact spacing. Fig. 4.41 (a) presents such plot. The R_T *vs* d_i have good linear tendency and the slopes have almost the same value of abscissa interception. The calculations for all four configuration, considering error propagation and a weighed average with the uncertainties, provides a sheet resistance equal to 124.4 $\pm$ 2.5 Ω, a transfer length of 491.4 $\pm$ 17.2 μm, and a contact resistance of 0.30 $\pm$ 0.02 $\Omega\cdot$ cm^2. With these values, the Si resistivity can be determined to be 9.0 $\pm$ 2.5 $\Omega\cdot$ m for the 725 $\pm$ 25 nm thick substrate. The results are within the considered range provided by the supplier, ρ_{Si} = 1-100 $\Omega\cdot$ m. Although, the distance from the top and bottom contact edges to the substrate edge is not zero ($\delta \neq 0$, Fig. 3.14). This means that lateral current flow may exist, which increases the resistance between the adjacent contacts and leads to inaccurate value. In order to consider this lateral current flow the QTD-TLM was applied, where the lateral current flow is modelled through an extra parallel resistance. [101] Fig. 4.41 (b) presents the QTD-TLM $R_T^{'}$ *vs* d_i. It is cleat the change in slope, since all 4 curves have equal slope value and a small variation on the interception is seen. This correction leads to a Si sheet resistance of 403.1 $\pm$ 7.3 Ω, transfer length of 404.7 $\pm$ 13.7 μm, and a contact resistance of 0.66 $\pm$ 0.04 $\Omega\cdot cm^2$. The Si resistivity can be estimated to be 29 $\pm$ 2 $\Omega\cdot$ m.

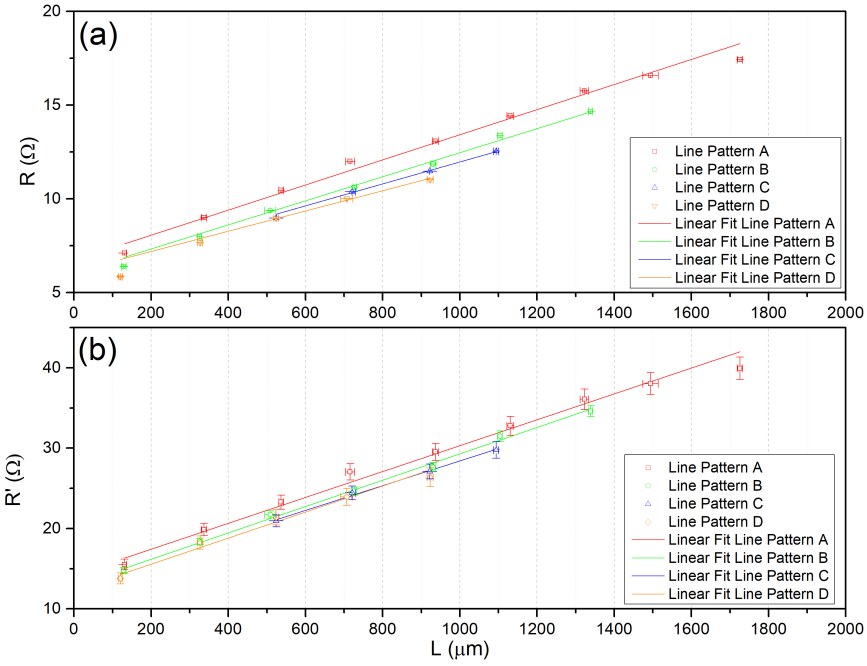

Figure 4.41: R_T *vs* d_i measurement plot, of the Si substrate, with (a) the conventional 1D TLM and (b) the correction for lateral current flow, QTD-TLM.

In order to understand if the previous ZnO_x and TiO_x TLM results were motivated by their thin layers, a 30 nm Cu layer was studied. Fig. 4.42 shows the measured IV curves for the Cu film. Similar to the Si IV curves, a linear tendency was obtained for all curves and a constant variation with the contact spacing increase.

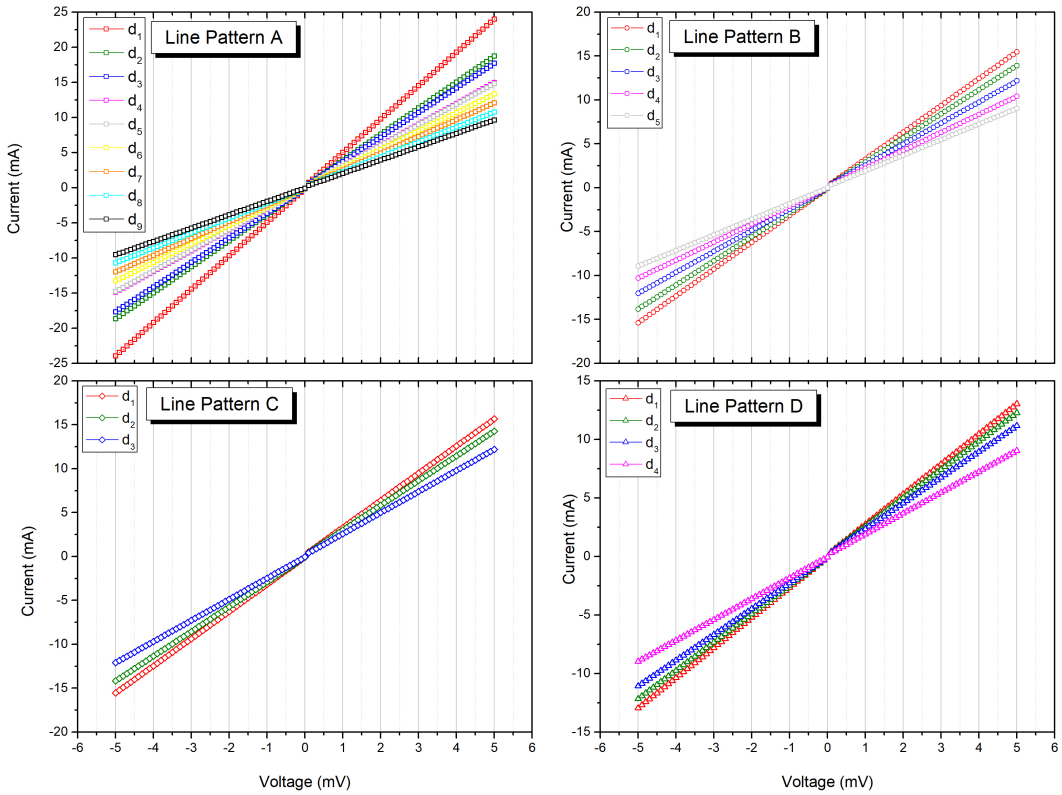

Figure 4.42: Cu TLM device IV curves, for all four configurations: line pattern A, B, C, and D.

From the Cu IV curves and the Ohms law, the R_T *vs* d_i dependency was obtained and plotted in Fig, 4.43. The Cu sheet resistance was determined to be 3.9 $\pm$ 0.2 Ω, the transfer length 452 $\pm$ 40 μm, and the contact resistance 8.3 $\pm$ 1.5 $m\Omega{\cdot}cm^2$. The Cu resistivity is calculated to be 115.8 $\pm$ 5.5 $n\Omega{\cdot}$m. The obtained resistivity is one order of magnitude higher than the reference value, 16.8 $n\Omega{\cdot}$m [163], which can be justified by two reasons: (1) the Cu resistivity increases with film thickness decrease, for magnetron sputtering deposited films [164], and (2) there may exist, inside and/or at the film surface Cu and Cu oxide (CuO and Cu_2O) phases that alter the film resistivity. [165]. It can be speculated that the latter reasons were not the cause for the high determined resistivity, but the film thickness. Although, TLM has been applied to determine these parameters for films with thickness between 5-30 nm [166, 167, 100, 168]. Hence, the film thickness should not be a problem when performing the TLM analysis.

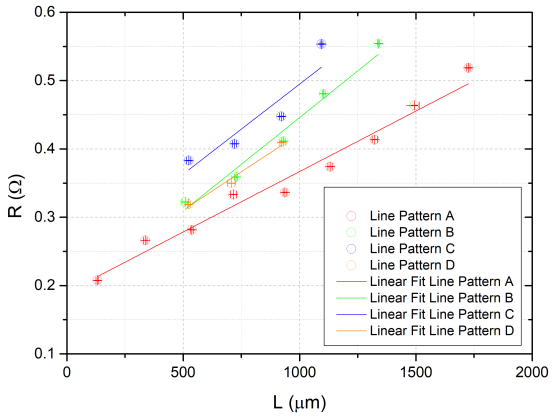

Figure 4.43: R_T *vs* d_i TLM measurement final plot, of the Cu film.

These previous results show that the devices architecture needs to be improved for thin film consideration. The new configuration, so called TLM B, instead of having an uniform film deposited in the all substrate area, such as in Fig. 3.4 (a), only has film below the contact areas, such as shown in Fig. 3.4 (b). [169, 167] Note that in this configuration, only the contact resistance will change between two different samples, since the sheet resistance reflects the resistance of the Si substrate below the films. Furthermore, this Si sheet resistance can be used to detect outliers in the measurements. The first sample analysed by this TLM B new configuration, was a 30 nm individual layers of SiO_x. It was expected that with this configuration, a linear IV plots would be obtained and that the R_c would be determined with high accuracy. Nevertheless, this was not the observed. The IV curves once again, do not have a linear behaviour, presenting different trends with negative and positive bias, and when increasing the contact spacings, the tendency is not correct. In order to understand this not expected trends, a closer look was taken at the IV curve obtained for the first contact pair, with spacing d_1.

Four charge transport mechanisms were considered in Fig. 4.44: (a) $ln(J)$ *vs* $ln(E)$ for Ohmic, (b) $ln(J)$ *vs* $E^{1/2}$ for Thermionic emission or Schottky, where the charge carrier can pass over the barrier, (c) $ln(J/E)$ *vs* $E^{1/2}$ for Frenkel-Poole (F-P) emission, where one trapped charge is emitted, and (d) $ln(J/E^2)$ *vs* $1/E$ for Fowler-Nordheim tunnelling, where the charges tunnel through the barrier. [170] In these equations, J is the current density and E the electric field. By observing the positive and negative bias curves, in each plot (a, b, c, or d), a difference between them can be seen. If a transport mechanism is happening, then the plot experiences a linear behaviour and the slope translates the intensity or amplitude of such mechanism. On Fig. 4.44 (a), (b) and (c), is possible to observe that all fours transport mechanisms occur at higher voltages, and at the low voltages only Ohmic, Schottky and F-P emission seem to occur. However, it is not clear what occurs at lower voltages. So, the existence of so many charge transport mechanisms, and the not predominance of Ohmic behaviour, limits the applicability of the TLM since Ohmic behaviour is required.

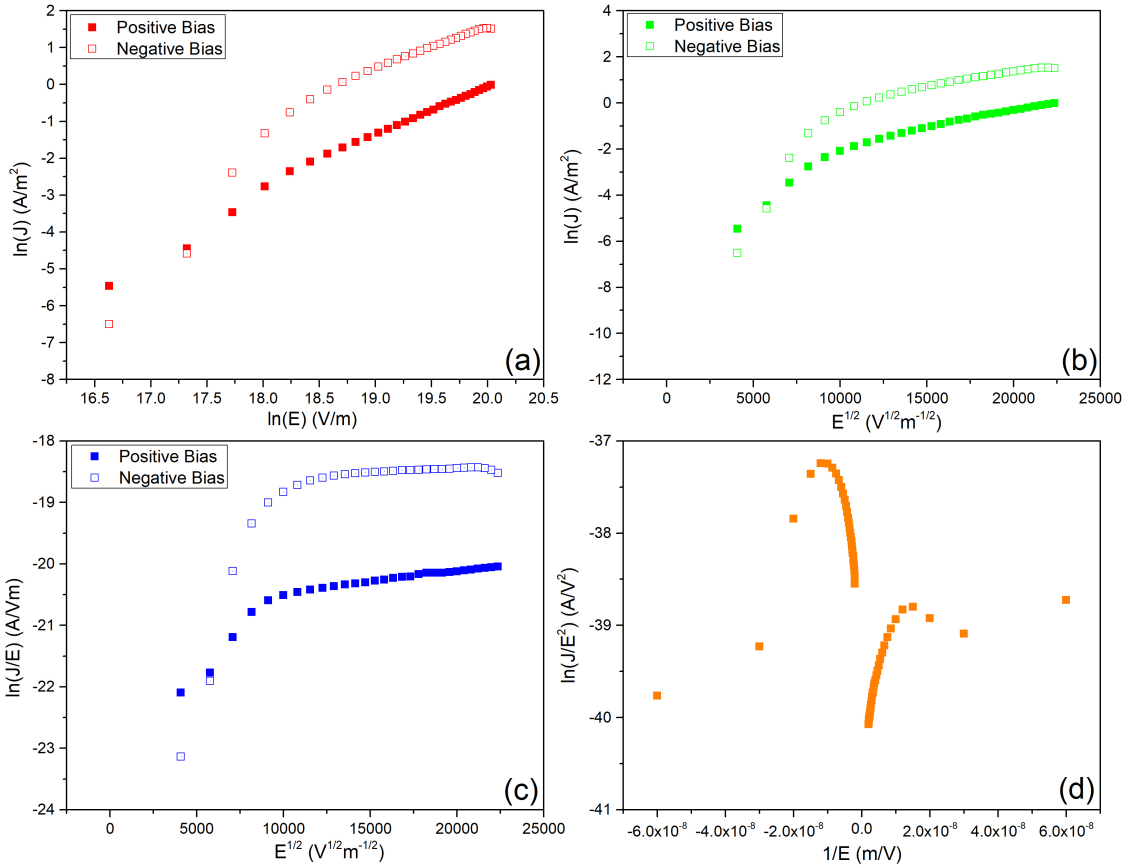

Figure 4.44: Current analysis of the TLM device for (a) Ohmic, (b) Schottky, (c) F-P emission, and (d) F-N tunnelling behaviour, in the -15 to 15 V range.

The existence of several transport mechanisms in a simple individual layer, can indicate a more complex operation for the nanolaminates. As said, this highlights the importance of this home-made devices in order to anticipate possible working limitations before the nanolaminates introduction in real optoelectronic devices. Moreover, the different architecture approaches used in the developed devices during this work, show the importance to customize and optimize those for a specific purpose.

4.5.3 Metal-Oxide-Semiconductor Devices

In Section 4.4 it was concluded that sample TZ2, the one with a complete electronic characterisation, had a too high conduction band offset with CIGS which may limit the electron selectivity. Although the conduction and valence band offset are essential to selectivity, there are other ways that can aid selectivity. In this scope, Metal-oxide-semiconductor (MOS) devices were developed to access the field-effective passivation capabilities of the designed samples, which is estimates by the fixed charge density (Q_f). The fabrication of these devices was similar to the capacitors ones. The major difference was the fact that the AlSiCu layer was deposited on the rear side of the Si substrate, instead of the front, to provide a back contact. Then, the sample layer, and circular AlSiCu contacts were deposited sequentially on the front side. Hence, the final structure is AlSiCu/Si/sample/AlSiCu (circular contacts). Only samples TZ0.1, TZ0.2, and ZT2 passivation

performance was studied. The assessment of these sample's Q_f parameter was a simple preliminary study. To estimate the Q_f value the Conductance method [97] was applied, where CV and Cf measurements need to be performed. In the equipment used to perform such measurements, the sample is modelled as a resistance in parallel with a capacitor. So in one voltage or frequency sweep, the capacitance and conductance (G) dependences can be measured. The conductance although not necessary in this calculation, can be helpful in detecting misconceptions or can be used to estimate other parameters. The applied voltage, on the CV measurements, has a sinusoidal behaviour with an amplitude of 25 mV and a given frequency f, and the CF and Gf curves were measures at 0 V.

Regarding the data analysis, it was observed different behaviours of CV when the applied voltage frequency was altered. This may indicate a major influence of the series resistance (R_s) of the device, on the measurements. [171] Moreover, on the GV measurements there is no peak present, which further confirms the dominant influence of the series resistance. [172, 173] The effect of this series resistance is mostly related to the device architecture and fabrication, and was corrected by introducing this resistance in the Conductance model. [173] Hence, the first step ii to correct the capacitance and conductance measurements, removing the series resistance component. Then the conductance method can be applied to estimate the Q_f. An intermediate step is the determination of the flat band voltage (V_{fb}) - condition where no band bending occurs, which is determined by the Inflection Point Method [174]. Also, it was necessary to introduce the semiconductor and metal contact work functions, which were retrieved from the literature. [175, 171]

Table 4.15: MOS analysis intermediate and final estimated values. The R_s and V_{fb} have a standard deviation (ω) associated with the estimated values, while Q_f has an uncertainty (δ).

Sample	R_s (Ω)	σ_{R_s} (Ω)	V_{fb} (V)	σV_{fb} (V)	$\times 10^{12} Q_f$ (cm^{-2})	$\times 10^{12} \delta Q_f$ (cm^{-2})
TZ0.1	224.7	24.4	-0.71	0.09	3.0	0.5
TZ0.2	283.3	14.9	-0.47	0.08	-13.8	0.4
ZT2	121.5	70.2	-0.87	0.03	259	23

The final results of this MOS analysis are presented in 4.15. The nanolaminate ZT2 shows a higher V_{fb} value, which can be correlated to the high number of interfaces that induce band bending inside its structure. Considering the Q_f value, the single layer of TiO_x (TZ0.1) shows a hole field-effect passivation, due to the same charge polarity, and ZnO_x (TZ0.2) a electron field-effect passivation, which was not expected since this material has electron selective capabilities. [53, 59] The nanolaminate TZ2 presented a significant enhancement on the absolute value of fixed charge density when compared to the individual layers, with a hole field-effect passivation capability. Thus, the nature of the fixed charge density of the ZT2 nanolaminate is compatible with an electron selective contact, since those will repel holes operating alongside the valence band offset, of 1.7 eV for CIGS and ZT2, to block holes. On the other hand, electrons will be attracted to this layer which may help to overcome a the electronic barrier between the CIGS and the selective contact.

5

Conclusion

In this work several multilayers systems were developed based in amorphous oxides, considering nominal SiO_x, SiN_x, TiO_x, ZnO_x, and HfO_x, to study their potential integration in optoelectronic devices as selective contacts, in particular in CIGS solar cells. From a fundamental point of view, single layers based on the aforementioned oxides were also studied.

A well behaved multilayer structure was verified by STEM imaging for a particular nanolaminate, grown by PECVD at near 300°C, with 3 nm SiO_x and SiN_x bilayer structure. A deviation of 13% in thickness was obtained, in comparison to the nominal value, as the bilayer presents a average value of 5.2 nm, instead of the nominal 6 nm. Despite a multi-structural architecture, the elemental distribution in the EDS line profiles did not show a clear distribution compatible with single layers of SiO_x and SiN_x. Thus, XPS were carried out to study the nanolaminate composition.

The XPS analysis revealed deviation in the elemental composition with respect to the nominal one. Single layers of $SiO_{1.7}$, $SiO_{0.2}N_{1.0}$, $TiO_{2.1}$, $ZnO_{0.7}$, and $HfO_{1.8}$ were obtained. Considering the approximately 10 nm thickness obtained by XPS, some results point for variation in the sublayer thickness in comparison to the nominal value, compatible with the observation in the STEM analysis. For the nanolaminates based on SiO_x-SiN_x, significant differences in the compositions regarding the single layer were obtained. A possible competition between N and O during deposition is suggested, taking into account that an increase in N leads to a significant decrease in O, and a decrease in N leads to a similar decrease in O. Highlighting the lack of control during the PECVD deposition, which it is not suitable for nano tailoring. The PECVD available at INL is mostly used for deposition of hundreds of nanometres layers where this meticulous control is less significant. Thus, this point lead to the rationale that PECVD is not optimized for a meticulous nano tailoring deposition. Moreover, nanolaminate deposition is a continuous process, and no chamber cleaning/purge occurs between the different materials deposition. So the chamber atmosphere can have previous gas precursors that will alter the chemical reaction and change the deposited film composition. Thus, it is clear that PECVD deposition is not optimized, and is not adequate, with the current conditions, for the deposition of thin films and for nanolaminates. Regarding the TiO_x, ZnO_x, and HfO_x nanolaminates, deposited by Magnetron Sputtering, the XPS results suggests a higher composition control in comparison to PECVD. However, the results point to sublayer thick-

nesses variations, which is compatible with the several deposition rate calibrations needed in order to reproduce the samples, during this work. Deviations in the nanolaminate composition, regarding the individual layers, were also observed, and may be controlled though a purge process in between each sublayer deposition. This is, however, an inexistent step in a Magnetron Sputtering process, as in the PECVD.

Despite the optical behaviour, for all nanolaminates, not being fully described by the effective medium approximation, the refractive index was tailored to exhibit values in a range compatible with the integration of those nanolaminates as selective contacts in CIGS solar cells. Several based TiO_x and ZnO_x nanolaminates present n values in the 2-2.5 range.

The electronic properties of the surface were analysed considering it as the CIGS/selective contact interface. It was observed a difference in conductivity of the nanolaminates in comparison with the individual layer, mostly due to composition differences. The electronic surface structure of a nanolaminate of 5 nm ZnO_x and 10 nm TiO_x, with a 2 times bilayer repetition, was fully characterized. An 1.2 eV conduction band offset was obtained for CIGS with this nanolaminate, while a valence band offset of 1.7 eV was respectively obtained, which meets the goal to block holes. The same nanolaminate presented a enhanced absolute value of fixed charge density, in comparison to its individual layers. The nature of this fixed charge density leads to hole field-effect passivation capability, compatible with an electron selective contact. The valence and conduction band offsets, joined with this field-effect passivation, leads to an improved electron selective contact.

Several home-made devices were developed to characterize the electric properties of the nanolaminates. Different transport mechanisms were identified in an individual layer, which may indicate complex transport mechanisms in the nanolaminate systems. This analysis shows the need to anticipate possible working limitations before the nanolaminates integration in real optoelectronic devices. Furthermore, the different architecture approaches used, show the importance to customize those to a specific objective. However, those need to be further optimized to fully comprehend the electrical behaviour and the impact of this multistructure when integrated on an optoelectronic device.

From a technological point of view, and considering CIGS based compounds for top layers of emerging tandem solar cells, that requires high bandgap value, as well as improved charge carrier extraction, the developed materials may have an important role as a potential electron selective contact with suitable band alignment.

The systematic approach used throughout this work allows a clear identification of the physical properties of nanolaminates. Our preliminary results clearly indicate the possibility of tailoring these properties to match technological requirements. The scientific path defined in the course of this work looks, therefore, very promising for the development of materials *à la carte*.

Future Work

The future work can be divided in two distinct paths: (1) integration of the studied samples in the CIGS technology, and (2) optimization and development of new architectures.

The first step must be a complete electronic characterization of the studied samples, to access the charge carrier selectivity. In this regard, determination of the fixed charge and the interface trap density, to discuss the passivation capabilities, should also be scrutinized. Moreover, the optimization of the electric home-made devices, to accurately access the sample's properties, while working on load, must also be carried out. The different CIGS compounds should be searched and its optoelectronic structure investigated, to integrate the nanolaminates as electrons selective contacts in conventional CIGS solar cells, or even tandem on.

New nanolaminates can be developed and studied, with the materials used in this work or new ones, in different and more complex architectures. To do so, the deposition process must be optimized to allows thickness and composition control of the sublayers. Between each sublayer deposition the chamber must be purged, the temperature should be accurately determined, the deposition ratios should be more extensively studied. Furthermore, this work can be mirrored for the development of holes selective contacts.

Bibliography

[1] P. Janthon, S. Luo, S. M. Kozlov, F. Viñes, J. Limtrakul, D. G. Truhlar, and F. Illas, "Bulk properties of transition metals: A challenge for the design of universal density functionals", *J. Chem. Theory Comput.*, vol. 10, no. 9, pp. 3832–3839, 2014.

[2] Compound Interest, "The Periodic Table's Endangered Elements", 2015. Acessed on: August, 2021. Available: https://www.compoundchem.com/2015/08/19/endangered-elements/.

[3] X. Chen and H. Baumgart, "Advances in atomic layer deposition (ALD) nanolaminate synthesis of thermoelectric films in porous templates for improved seebeck coefficient", *Materials (Basel)*, vol. 13, no. 6, pp. 1–20, 2020.

[4] Fr B.-Y. Li, F. Chen, H.-N. Xiong, L. Tang, J.-X. Shao, and Z.-J. Yang, "Unified and ultimate high pressure phase of several nanolaminate $M_{n+1}AX_n$ (n = 1, 2, 3, etc.) ceramics from first principles", *Results Phys.*, vol. 28, p. 104681, 2021.

[5] L. Fu and W. Xia, "MAX Phases as Nanolaminate Materials: Chemical Composition, Microstructure, Synthesis, Properties, and Applications", *Adv. Eng. Mater.*, vol. 23, no. 4, pp. 1–31, 2021.

[6] L. Zhang, P. Yu, J. Fan, Y. Li, Y. Gao, and G. Li, "High pressure induced the polymorphism phase transition in the $Fe_{40}Mn_{40}Co_{10}Cr_{10}$ multi-principal element alloy", *Intermetallics*, vol. 136, p. 107268, 2021.

[7] J. Azadmanjiri, J. Wang, C. C. Berndt, and A. Yu, "2D layered organic-inorganic heterostructures for clean energy applications", *J. Mater. Chem. A*, vol. 6, no. 9, pp. 3824–3849, 2018.

[8] International Renewable Energy Agency (IRENA), "World energy transitions Outlook: 1.5º Pathway", Abu Dhabi, 2021.

[9] I. M. Peters, C. D. Rodriguez Gallegos, S. E. Sofia, and T. Buonassisi, "The Value of Efficiency in Photovolt.", *Joule*, vol. 3, no. 11, pp. 2732–2747, 2019.

[10] Fraunhofer Institute for Solar Energy Systems, "Photovoltaics Report", Freiburg, 2021.

[11] L. M. Mansfield, A. Kanevce, S. P. Harvey, K. Bowers, C. Beall, S. Glynn, and I. L. Repins, "Efficiency increased to 15.2% for ultra-thin $Cu(In,Ga)Se_2$ solar cells", *Prog. Photovolt. Res. Appl.*, vol. 26, no. 11, pp. 949–954, 2018.

[12] M. Nakamura, K. Yamaguchi, Y. Kimoto, Y. Yasaki, T. Kato, and H. Sugimoto, "Cd-Free $Cu(In,Ga)(Se,S)_2$ Thin-Film Solar Cell With Record Efficiency of 23.35 %", *IEEE J. Photovolt.*, vol. 9, no. 6, pp. 1863–1867, 2019.

[13] I. V. G. K. S. Novoselov, A. K. Geim, S. V. Morozov, D. Jiang, Y. Zhang, S. V. Dubonos and A. A. Firsov, "Electric Field Effect in Atomically Thin Carbon Films", *Science*, vol. 306, no. 5696, pp. 666–669, 2004.

[14] Yury Gogo, *Nanomaterials Handbook*, New York: CRC Press, 2006.

[15] R. K. Goyal, *Nanomaterials and Nanocomposites: Synthesis, Properties, Characterization Techniques, and Applications*, New York: CRC Press, 2017.

[16] J. Liu, H. Zhang, M. Qiu, Z. Peng, M. K. Leung, W. F. Lin, and J. Xuan, "A review of non-precious metal single atom confined nanomaterials in different structural dimensions (1D-3D) as highly active oxygen redox reaction electrocatalysts", *J. Mater. Chem. A*, vol. 8, no. 5, pp. 2222–2245, 2020.

[17] J. Azadmanjiri, C. C. Berndt, J. Wang, A. Kapoor, V. K. Srivastava, and C. Wen, "A review on hybrid nanolaminate materials synthesized by deposition techniques for energy storage applications", *J. Mater. Chem. A*, vol. 2, no. 11, pp. 3695–3708, 2014.

[18] J. Azadmanjiri, C. C. Berndt, J. Wang, A. Kapoor, and V. K. Srivastava, "Nanolaminated composite materials: Structure, interface role and applications", *RSC Adv.*, vol. 6, no. 111, pp. 109361–109385, 2016.

[19] M. Nasim, Y. Li, M. Wen, and C. Wen, "A review of high-strength nanolaminates and evaluation of their properties", *J. Mater. Sci. Technol.*, vol. 50, pp. 215–244, 2020.

[20] Y. Hinuma, H. Hayashi, Y. Kumagai, I. Tanaka, and F. Oba, "Comparison of approximations in density functional theory calculations: Energetics and structure of binary oxides", *Phys. Rev. B*, vol. 96, p. 094102, 2017.

[21] M. Knez, K. Nielsch, and L. Niinistö, "Synthesis and surface engineering of complex nanostructures by atomic layer deposition", *Adv. Mater.*, vol. 19, no. 21, pp. 3425–3438, 2007.

[22] D. Muñoz-Rojas, V. H. Nguyen, C. Masse de la Huerta, S. Aghazadehchors, C. Jiménez, and D. Bellet, "Spatial Atomic Layer Deposition (SALD), an emerging tool for energy materials. Application to new-generation photovoltaic devices and transparent conductive materials", *Comptes Rendus Phys.*, vol. 18, no. 7-8, pp. 391–400, 2017.

[23] J. Wang, Q. Zhou, S. Shao, and A. Misra, "Strength and plasticity of nanolaminated materials", *Mater. Res. Lett.*, vol. 5, no. 1, pp. 1–19, 2017.

[24] N. M. Litchinitser, "Nonlinear optics in metamaterials", *Adv. Phys. X*, vol. 3, no. 1, pp. 702–719, 2018.

[25] L. Alloatti, C. Kieninger, A. Froelich, M. Lauermann, T. Frenzel, K. Köhnle, W. Freude, J. Leuthold, M. Wegener, and C. Koos, "Second-order nonlinear optical metamaterials: ABC-type nanolaminates", *Appl. Phys. Lett.*, vol. 107, no. 12, p. 121903, 2015.

[26] T. F. Fuerst, M. O. Reese, and C. A. Wolden, "PECVD Synthesis of Flexible Optical Coatings for Renewable Energy Applications", *Plasma Process. Polym.*, vol. 13, no. 1, pp. 184–190, 2016.

[27] S. Y. Jeong, H. R. Shim, Y. Na, K. S. Kang, Y. Jeon, S. Choi, E. G. Jeong, Y. C. Park, H. E. Cho, J. Lee, J. H. Kwon, S. G. Im, and K. C. Choi, "Foldable and washable textile-based OLEDs with a multi-functional near-room-temperature encapsulation layer for smart e-textiles", *npj Flex. Electron.*, vol. 5, no. 1, pp. 1–9, 2021.

[28] D. Suh, "Stacked and nanolaminated Al_2O_3/TiO_2 for surface passivation and encapsulation of silicon", *Phys. Status Solidi - Rapid Res. Lett.*, vol. 9, no. 6, pp. 344–347, 2015.

[29] Y. Wang, Z. Yu, Y. Yang, and J. Sun, "Bright red electroluminescence from Al_2O_3/Eu_2O_3 nanolaminate films fabricated by atomic layer deposition on silicon", *Scr. Mater.*, vol. 196, p. 113750, 2021.

[30] A. Kashir and H. Hwang, "A CMOS-compatible morphotropic phase boundary", *Nanotechnology*, vol. 32, no. 44, p. 445706, 2021.

[31] W. Li, Z. Chen, R. N. Premnath, B. Kabius, and O. Auciello, "Controllable giant dielectric constant in AlO_x/TiO_y nanolaminates", *J. Appl. Phys.*, vol. 110, no. 2, p. 024106, 2011.

[32] S. Fu, R. Shen, P. Zhu, and Y. Ye, "Metal-interlayer-metal structured initiator containing Al/CuO reactive multilayer films that exhibits improved ignition properties", *Sens Actuator A: Phys.*, vol. 292, pp. 198–204, 2019.

[33] J. Xu, Y. Shen, C. Wang, J. Dai, Y. Tai, Y. Ye, R. Shen, H. Wang, and M. R. Zachariah, "Controlling the energetic characteristics of micro energy storage device by in situ deposition Al/MoO_3 nanolaminates with varying internal structure", *Chem. Eng. J.*, vol. 373, pp. 345–354, 2019.

[34] D. K. Simon, P. M. Jordan, M. Knaut, T. Chohan, T. Mikolajick, and I. Dirnstorfer, "ALD Al_2O_3 based nanolaminates for solar cell applications", *2015 IEEE 42nd Photovolt. Spec. Conf. (PVSC)*, vol. 2, pp. 1–6, 2015.

[35] I. Dirnstorfer, T. Chohan, P. M. Jordan, M. Knaut, D. K. Simon, J. W. Bartha, and A. Al, "$Al_2O_3 - TiO_2$ Nanolaminates for Conductive Silicon Surface Passivation", *EEE J. Photovolt.*, vol. 6, no. 1, pp. 86–91, 2016.

[36] F. Liu, Q. Zeng, J. Li, X. Hao, A. Ho-Baillie, J. Tang, and M. A. Green, "Emerging inorganic compound thin film photovoltaic materials: Progress, challenges and strategies", *Mater. Today*, vol. 41, pp. 120–142, 2020.

[37] J. L. Thomas Feurer, Patrick Reinhard, Enrico Avancini, Benjamin Bissig, "Progress in thin film CIGS photovoltaics: Research and development, manufacturing, and applications", *Prog. Photovolt. Res. Appl*, vol. 25, pp. 645–667, 2016.

[38] M. Ochoa, S. Buecheler, A. N. Tiwari, and R. Carron, "Challenges and opportunities for an efficiency boost of next generation $Cu(In,Ga)Se_2$ solar cells: Prospects for a paradigm shift", *Energy Environ. Sci.*, vol. 13, no. 7, pp. 2047–2055, 2020.

[39] P. M. Salomé, H. Rodriguez-Alvarez, and S. Sadewasser, "Incorporation of alkali metals in chalcogenide solar cells", *Sol. Energy Mater. Sol. Cells*, vol. 143, pp. 9–20, 2015.

[40] S. Siebentritt, E. Avancini, M. Bär, J. Bombsch, E. Bourgeois, S. Buecheler, *et al.*, "Heavy Alkali Treatment of $Cu(In,Ga)Se_2$ Solar Cells: Surface versus Bulk Effects", *Adv. Energy Mater.*, vol. 10, no. 8, p. 1903752, 2020.

[41] P. Salomé, V. Fjällström, A. Hultqvist, and M. Edoff, "Na doping of CIGS solar cells using low sodium-doped mo layer", *IEEE J. Photovolt.*, vol. 3, no. 1, pp. 509–513, 2013.

[42] M. Green, K. Emery, Y. Hishikawa, W. Warta, E. Dunlop, D. Barkhouse, O. Gunawan, T. Gokmen, T. Todorov, and D. Mitzi, "Solar cell efficiency tables (version 40)", *IEEE Trans Fuzzy Syst*, vol. 20, no. 6, pp. 1114–1129, 2012.

[43] P. Jackson, R. Wuerz, D. Hariskos, E. Lotter, W. Witte, and M. Powalla, "Effects of heavy alkali elements in $Cu(In,Ga)Se_2$ solar cells with efficiencies up to 22.6%", *Phys. Status Solidi - Rapid Res. Lett.*, vol. 10, no. 8, pp. 583–586, 2016.

[44] K. Mitchell, C. Eberspacher, J. Ermer, and D. Pier, "Single and tandem junction $CuInSe_2$ cell and module technology", *Conf. Rec. IEEE Photovolt. Spec. Conf.*, vol. 2, pp. 1384–1389, 1988.

[45] L. M. Mansfield, A. Kanevce, S. P. Harvey, K. Bowers, C. Beall, S. Glynn, and I. L. Repins, "Efficiency increased to 15.2% for ultra-thin $Cu(In,Ga)Se_2$ solar cells", *Prog. Photovolt. Res. Appl.*, vol. 26, no. 11, pp. 949–954, 2018.

[46] A. Oliveira, J. Barbosa, A. Violas, J. Teixeira, K. Oliveira, T. Lopes, J. Cunha, M. Curado, M. Monteiro, C. Rocha, C. Vinhais, P. Fernandes, and P. Salomé, "Optoelectronic simulations for novel light management concepts in $Cu(In,Ga)Se_2$ solar cells", *Proc. SPIE*, vol. 11681, p. 1168108, 2021.

[47] P. M. Salomé, B. Vermang, R. Ribeiro-Andrade, J. P. Teixeira, J. M. Cunha, M. J. Mendes, S. Haque, J. Borme, H. Águas, E. Fortunato, R. Martins, J. C. González, J. P. Leitão, P. A. Fernandes, M. Edoff, and S. Sadewasser, "Passivation of Interfaces in Thin Film Solar Cells:

Understanding the Effects of a Nanostructured Rear Point Contact Layer", *Adv. Mater. Interfaces*, vol. 5, no. 2, pp. 1–10, 2018.

[48] M. Monteiro, M. A. Curado, A. J. N. Oliveira, K. Oliveira, J. P. Teixeira, W. C. Chen, M. Edoff, P. M. P. Salomé, P. A. Fernandes, and A. G. Silva, "X-ray Photoelectron Spectroscopy for Studying Passivation Architectures of $Cu(In,Ga)Se_2$ Cells", *EEE 48th Photovolt. Spec. Conf. (PVSC)*, pp. 890–892, 2021.

[49] K. Oliveira, W.-c. Chen, J. Lontchi, A. J. N. Oliveira, J. P. Teixeira, M. Edoff, P. A. Fernandes, and P. M. P. Salomé, "SiO_x patterned based substrates implemented in $Cu(In,Ga)Se_2$ ultrathin solar cells : optimum thickness", *EEE 48th Photovolt. Spec. Conf. (PVSC)*, pp. 928–930, 2021.

[50] M. A. Curado, J. P. Teixeira, M. Monteiro, E. F. Ribeiro, R. C. Vilão, H. V. Alberto, J. M. Cunha, T. S. Lopes, K. Oliveira, O. Donzel-Gargand, A. Hultqvist, S. Calderon, M. A. Barreiros, W. Chiappim, J. P. Leitão, A. G. Silva, T. Prokscha, C. Vinhais, P. A. Fernandes, and P. M. Salomé, "Front passivation of $Cu(In,Ga)Se_2$ solar cells using Al_2O_3: Culprits and benefits", *Appl. Mater. Today*, vol. 21, p. 100867,2020.

[51] J. M. Cunha, K. Oliveira, J. Lontchi, T. S. Lopes, M. A. Curado, J. R. Barbosa, C. Vinhais, W. C. Chen, J. Borme, H. Fonseca, J. Gaspar, D. Flandre, M. Edoff, A. G. Silva, J. P. Teixeira, P. A. Fernandes, and P. M. Salomé, "High-Performance and Industrially Viable Nanostructured SiO_x Layers for Interface Passivation in Thin Film Solar Cells", *Sol. RRL*, vol. 5, no. 3, pp. 1–13, 2021.

[52] C. Yu, S. Xu, J. Yao, and S. Han, "Recent advances in and new perspectives on crystalline silicon solar cells with carrier-selective passivation contacts", *Crystals*, vol. 8, no. 11, p. 430, 2018.

[53] J. Melskens, B. W. Van De Loo, B. Macco, L. E. Black, S. Smit, and W. M. Kessels, "Passivating Contacts for Crystalline Silicon Solar Cells: From Concepts and Materials to Prospects", *IEEE J. Photovolt.*, vol. 8, no. 2, pp. 373–388, 2018.

[54] S. Glunz, M. Bivour, C. Messmer, F. Feldmann, R. Muller, C. Reichel, A. Richter, F. Schindler, J. Benick, and M. Hermle, "Passivating and Carrier-selective Contacts - Basic Requirements and Implementation", *IEEE 44th Photovolt. Spec. Conf. (PVSC)*, pp. 2064–2069, 2018.

[55] A. Onno, C. Chen, P. Koswatta, M. Boccard, and Z. C. Holman, "Passivation, conductivity, and selectivity in solar cell contacts: Concepts and simulations based on a unified partial-resistances framework", *J. Appl. Phys.*, vol. 126, no. 18, p. 183103, 2019.

[56] X. Jiang, P. Zhang, J. Zhang, J. Wang, G. Li, X. Fang, L. Yang, and X. Chen, "High Performance of PEDOT:PSS/n-Si Solar Cells Based on Textured Surface with AgNWs Electrodes", *Nanoscale Res. Lett.*, vol. 13, p. 53, 2018.

[57] K. K. Markose, M. Shaji, S. Bhatia, P. R. Nair, K. J. Saji, A. Antony, and M. K. Jayaraj, "Novel Boron-Doped p-Type Cu_2O Thin Films as a Hole-Selective Contact in c-Si Solar Cells", *ACS Appl. Mater. Interfaces*, vol. 12, no. 11, pp. 12972–12981, 2020.

[58] C. Altinkaya, E. Aydin, E. Ugur, F. H. Isikgor, A. S. Subbiah, M. De Bastiani, J. Liu, A. Babayigit, T. G. Allen, F. Laquai, A. Yildiz, and S. De Wolf, "Tin Oxide Electron-Selective Layers for Efficient, Stable, and Scalable Perovskite Solar Cells", *Adv. Mater.*, vol. 33, no. 15, pp. 1–32, 2021.

[59] E. Yalcin, M. Can, C. Rodriguez-Seco, E. Aktas, R. Pudi, W. Cambarau, S. Demic, and E. Palomares, "Semiconductor self-assembled monolayers as selective contacts for efficient PiN perovskite solar cells", *Energy Environ. Sci.*, vol. 12, no. 1, pp. 230–237, 2019.

[60] Y. Yu and P. Gao, "Development of electron and hole selective contact materials for perovskite solar cells", *Chinese Chem. Lett.*, vol. 28, no. 6, pp. 1144–1152, 2017.

[61] J. Dréon, Q. Jeangros, J. Cattin, J. Haschke, L. Antognini, C. Ballif, and M. Boccard, "23.5%-Efficient Silicon Heterojunction Silicon Solar Cell Using Molybdenum Oxide As Hole-Selective Contact", *Nano Energy*, vol. 70, p. 104495, 2020.

[62] L. G. Gerling, S. Mahato, A. Morales-Vilches, G. Masmitja, P. Ortega, C. Voz, R. Alcubilla, and J. Puigdollers, "Transition metal oxides as hole-selective contacts in silicon heterojunctions solar cells", *Sol. Energy Mater. Sol. Cells*, vol. 145, pp. 109–115, 2016.

[63] O. Almora, L. G. Gerling, C. Voz, R. Alcubilla, J. Puigdollers, and G. Garcia-Belmonte, "Superior performance of V2O5 as hole selective contact over other transition metal oxides in silicon heterojunction solar cells", *Sol. Energy Mater. Sol. Cells*, vol. 168, no. May, pp. 221–226, 2017.

[64] H. S. Kim, J. E. Park, M. Patel, H. Kim, D. S. Kim, S. K. Byeon, D. Lim, and J. Kim, "Optically transparent and electrically conductive NiO window layer for Si solar cells", *Mater. Lett.*, vol. 174, pp. 10–13, 2016.

[65] Z. Yang, P. Gao, J. Sheng, H. Tong, C. Quan, X. Yang, K. W. Chee, B. Yan, Y. Zeng, and J. Ye, "Principles of dopant-free electron-selective contacts based on tunnel oxide/low work-function metal stacks and their applications in heterojunction solar cells", *Nano Energy*, vol. 46, pp. 133–140, 2018.

[66] M. Liu, Y. Zhou, G. Dong, W. Wang, J. Wang, C. Liu, F. Liu, and D. Yu, "SnO_2/Mg combination electron selective transport layer for Si heterojunction solar cells", *Sol. Energy Mater. Sol. Cells*, vol. 200, p. 109996, 2019.

[67] Y. Wan, C. Samundsett, J. Bullock, T. Allen, M. Hettick, D. Yan, P. Zheng, X. Zhang, J. Cui, J. McKeon, A. Javey, and A. Cuevas, "Magnesium Fluoride Electron-Selective Contacts for Crystalline Silicon Solar Cells", *ACS Appl. Mater. Interfaces*, vol. 8, no. 23, pp. 14671–14677, 2016.

[68] T. Matsui, M. Bivour, P. F. Ndione, R. S. Bonilla, and M. Hermle, "Origin of the tunable carrier selectivity of atomic-layer-deposited TiO_x nanolayers in crystalline silicon solar cells", *Sol. Energy Mater. Sol. Cells*, vol. 209, p. 110461, 2020.

[69] A. Kahouli, O. Lebedev, M. Ben Elbahri, B. Mercey, W. Prellier, S. Riedel, M. Czernohorsky, F. Lallemand, C. Bunel, and U. Lüders, "Structural and Dielectric Properties of Subnanometric Laminates of Binary Oxides", *ACS Appl. Mater. Interfaces*, vol. 7, no. 46, pp. 25679–25684, 2015.

[70] J. H. Lee, K. H. Min, M. G. Kang, K. T. Jeong, J. I. Lee, H. eun Song, S. Park, and J. S. Park, "Efficiency characteristics of a silicon oxide passivation layer on p-type crystalline silicon solar cell at low illumination", *Curr. Appl. Phys.*, vol. 19, no. 6, pp. 683–689, 2019.

[71] J. Kim, J. Park, J. H. Hong, S. J. Choi, G. H. Kang, G. J. Yu, N. S. Kim, and H. E. Song, "Double antireflection coating layer with silicon nitride and silicon oxide for crystalline silicon solar cell", *J. Electroceramics*, vol. 30, no. 1-2, pp. 41–45, 2013.

[72] C. Y. Chen, K. S. Chang-Liao, J. J. Ho, and T. K. Wang, "Improved programming/erasing speed of charge-trapping flash device with tunneling layer formed by low temperature nitrogen-rich SiN/SiO_2 stack", *Solid. State. Electron.*, vol. 78, pp. 22–27, 2012.

[73] X. Cheng, H. Haug, M. D. Sabatino, J. Zhu, and E. S. Marstein, "Electronic Properties of $a-SiO_xN_y:H/SiN_x$ Stacks for Surface Passivation of P-Type Crystalline Si Wafers", *IEEE J. Photovolt.*, vol. 6, no. 5, pp. 1103–1108, 2016.

[74] L. Janßen, H. Windgassen, D. L. Bätzner, B. Bitnar, and H. Neuhaus, "Silicon nitride passivated bifacial Cz-silicon solar cells", *Sol. Energy Mater. Sol. Cells*, vol. 93, no. 8, pp. 1435–1439, 2009.

[75] M. J. Rivera, E. B. Ramírez, B. Juárez, J. González, J. M. García-León, L. Escobar-Alarcón, and J. C. Alonso, "Low temperature-pyrosol-deposition of aluminum-doped zinc oxide thin films for transparent conducting contacts", *Thin Solid Films*, vol. 605, pp. 108–115, 2016.

[76] S. Calnan, J. Hüpkes, B. Rech, H. Siekmann, and A. N. Tiwari, "High deposition rate aluminium-doped zinc oxide films with highly efficient light trapping for silicon thin film solar cells", *Thin Solid Films*, vol. 516, no. 6, pp. 1242–1248, 2008.

[77] X. Yang, Q. Bi, H. Ali, K. Davis, W. V. Schoenfeld, and K. Weber, "High-Performance TiO_2-Based Electron-Selective Contacts for Crystalline Silicon Solar Cells", *Adv. Mater.*, vol. 28, no. 28, pp. 5891–5897, 2016.

[78] J. Cui, Y. Wan, Y. Cui, Y. Chen, P. Verlinden, and A. Cuevas, "Highly effective electronic passivation of silicon surfaces by atomic layer deposited hafnium oxide", *Appl. Phys. Lett.*, vol. 110, p. 021602, 2017.

[79] P. M. Jordan, D. K. Simon, T. Mikolajick, and I. Dirnstorfer, "Trapped charge densities in Al_2O_3-based silicon surface passivation layers", *J. Appl. Phys.*, vol. 119, p. 215306, 2016.

[80] S. M. Rupich and Y. J. Chabal, "Wet chemical modification of H-terminated si surfaces as a first step in atomic layer deposition", in *Encyclopedia of Interfacial Chemistry*, Elsevier, pp. 886–900, 2018.

[81] M. J. Madou, *Fundamentals of Microfabrication and Nanotechnology, Volume II: Manufacturing Techniques for Microfabrication and Nanotechnology*, 3rd ed. New York: CRC Press, 2018.

[82] Krishna Seshan, *Handbook of Thin Film Deposition*, 3rd ed. Great Britain: Elsevier Inc., 2012.

[83] Bharat Bhushan, *Springer Handbook of Nanotechnology*, 4th ed. Germany: Springer International Publishing, 2017.

[84] C. Mack, *Fundamental Principles of Optical Lithography: The Science of Microfabrication*, 6th ed. England: Wiley, 2007.

[85] D. Abou-Ras, T. Kirchartz, and U. Rau, *Advanced Characterization Techniques for Thin Film Solar Cells: Volume 1*, 2nd ed. Germany: Wiley-VCH, 2016.

[86] L. Reimer and H. Kohl, *Transmission Electron Microscopy: Physics of Image Formation*, 5th ed. Germany: Springer International Publishing, 2008.

[87] C. P. Kasap S., *Springer Handbook of Electronic and Photonic Materials*, 2nd ed. Trento: Springer International Publishing, 2017.

[88] M. C. Rowe and B. J. Brewer, "AMORPH: A statistical program for characterizing amorphous materials by X-ray diffraction", *Comput. Geosci.*, vol. 120, pp. 21–31, 2018.

[89] H. Fujiwara and R. W. Collins, *Spectroscopic Ellipsometry for Photovolt. Volume 1: Fundamental Principles and Solar Cell Characterization*, Springer International Publishing, 2018.

[90] H. G. Tompkins and J. N. Hilfiker, *Spectroscopic Ellipsometry: Practical Application to Thin Film Characterization*, States of America: Momentum Press, 2016.

[91] H. Fujiwara, *Spectroscopy Ellipsometry: Principles and Applications*, Japan: Wiley, 2007.

[92] A. Dahshan and K. A. Aly, "Determination of the thickness and optical constants of amorphous Ge-Se-Bi thin films", *Philos. Mag.*, vol. 89, no. 12, pp. 1005–1016, 2009.

[93] P. V. et al E. Marquez, J. Ramirez-Malo, "Calculation of the thickness and optical constants of amorphous arsenic sulphide films from their transmission spectra", *J. Phys. D Appl. Phys.*, no. 25, p. 535, 1992.

[94] O. S. Heavens, *Optical properties of thin solid films*, London: Dover Publications, 1955.

[95] H. Macleod, *Thin-Film Optical Filters*, 5th ed. Boca Raton, FL: CRC Press, 2014.

[96] Hufner, *Photoelectron Spectroscopy: Principles and Applications*, 3rd ed. Germany: Springer, 2003.

[97] J. M. Cunha, P. A. Fernandes, A. Hultqvist, J. P. Teixeira, S. Bose, B. Vermang, S. Garud, D. Buldu, J. Gaspar, M. Edoff, J. P. Leitao, and P. M. Salomé, "Insulator Materials for Interface Passivation of $Cu(In,Ga)Se_2$ Thin Films", *IEEE J. Photovolt.*, vol. 8, no. 5, pp. 1313–1319, 2018.

[98] D. K. Schroder, "Contact Resistance and Schottky Barriers", in *Semiconductor Material and Device Characterization*, 3rd ed. United States of America: Wiley, 2006, pp. 127–184.

[99] H. J. Ueng, D. B. Janes, and K. J. Webb, "Error analysis leading to design criteria for transmission line model characterization of ohmic contacts", *IEEE Trans. Electron Devices*, vol. 48, no. 4, pp. 758–766, 2001.

[100] W. Wang, H. Lin, Z. Yang, Z. Wang, J. Wang, L. Zhang, M. Liao, Y. Zeng, P. Gao, B. Yan, and J. Ye, "An Expanded Cox and Strack Method for Precise Extraction of Specific Contact Resistance of Transition Metal Oxide/n-Silicon Heterojunction", *IEEE J. Photovolt.*, vol. 9, no. 4, pp. 1113–1120, 2019.

[101] E. F. Chor and J. Lerdworatawee, "Quasi-two-dimensional transmission line model (QTD-TLM) for planar ohmic contact studies", *IEEE Trans. Electron Devices*, vol. 49, no. 1, pp. 105–111, 2002.

[102] P. Borowicz, A. Taube, W. Rzodkiewicz, M. Latek, and S. Gierałtowska, "Raman spectra of high-κ dielectric layers investigated with micro-raman spectroscopy comparison with silicon dioxide", *Sci. World J.*, vol. 2013, p. 208081, 2013.

[103] L. Y. Zhao, H. Jalili, N. Panjwani, T. Chan, Z. H. He, N. F. Heinig, and K. T. Leung, "Formation of ferromagnetic iron core-shell nanocubes on a H-terminated Si(100) surface by electrodeposition", *Electrochem. Solid-State Lett.*, vol. 10, no. 10, pp. 1–4, 2007.

[104] W. Chen, T. N. Truong, H. T. Nguyen, C. Samundsett, S. P. Phang, D. MacDonald, A. Cuevas, L. Zhou, Y. Wan, and D. Yan, "Influence of PECVD deposition temperature on phosphorus doped poly-silicon passivating contacts", *Sol. Energy Mater. Sol. Cells*, vol. 206, p. 110348, 2020.

[105] J. W. Hoon, K. Y. Chan, and C. Y. Low, "XRD investigations on film thickness and substrate temperature effects of DC magnetron sputtered ZnO films", *Adv. Mater. Res.*, vol. 845, pp. 241–245, 2014.

[106] C. H. Hsu, H. Y. Chen, and C. J. Tsai, "Stoichiometry dependence of electrochemical behavior of silicon oxide thin film for lithium ion batteries", *J. Power Sources*, vol. 438, p. 226943, 2019.

[107] A. G. Rolo, O. Conde, and M. J. Gomes, "Structural and optical studies of CdS nanocrystals embedded in silicon dioxide films", *Thin Solid Films*, vol. 318, pp. 108–112, 1998.

[108] R. S. Pessoa, F. P. Pereira, G. E. Testoni, W. Chiappim, H. S. Maciel, and L. V. Santos, "Effect of substrate type on structure of TiO_2 thin film deposited by atomic layer deposition technique", *J. Integr. Circuits Syst.*, vol. 10, no. 1, pp. 38–42, 2015.

[109] M. S. Yadav, N. Singh, and S. M. Bobade, "Zinc oxide nanoparticles and activated charcoal-based nanocomposite electrode for supercapacitor application", *Ionics (Kiel)*, vol. 24, no. 11, pp. 3611–3630, 2018.

[110] M. Ginting, S. Taslima, K. Sebayang, D. Aryanto, T. Sudiro, and P. Sebayang, "Preparation and characterization of zinc oxide doped with ferrite and chromium", *AIP Conf. Proc.*, vol. 1862, p. 030062,, 2017.

[111] S. Talam, S. R. Karumuri, and N. Gunnam, "Synthesis, Characterization, and Spectroscopic Properties of ZnO Nanoparticles", *ISRN Nanotechnology*, vol. 2012, pp. 1–6, 2012.

[112] M. Y. Ho, H. Gong, G. D. Wilk, B. W. Busch, M. L. Green, P. M. Voyles, D. A. Muller, M. Bude, W. H. Lin, A. See, M. E. Loomans, S. K. Lahiri, and P. I. Räisänen, "Morphology and crystallization kinetics in HfO_2 thin films grown by atomic layer deposition", *J. Appl. Phys.*, vol. 93, no. 3, pp. 1477–1481, 2003.

[113] G. Greczynski and L. Hultman, "C 1s Peak of Adventitious Carbon Aligns to the Vacuum Level: Dire Consequences for Material's Bonding Assignment by Photoelectron Spectroscopy", *ChemPhysChem*, vol. 18, no. 12, pp. 1507–1512, 2017.

[114] P. Swift, "Adventitious carbon the panacea for energy referencing?", *Surf. Interface Anal.*, vol. 4, no. 2, pp. 47–51, 1982.

[115] N. K.S. Kim, "Charge Transfer shake up satellites in XPS of cations and anions of $SrTiO_3$, TiO_2 and Sc_2O_3", *Chem. Phys. Lett.*, vol. 31, no. 2, pp. 312–317, 1975.

[116] H. Hernández-Arriaga, E. López-Luna, E. Martínez-Guerra, M. M. Turrubiartes, A. G. Rodríguez, and M. A. Vidal, "Growth of HfO_2/TiO_2 nanolaminates by atomic layer deposition and $HfO_2 - TiO_2$ by atomic partial layer deposition", *J. Appl. Phys.*, vol. 121, no. 6, p. 064302, 2017.

[117] A. O. T. Patrocínio, E. B. Paniago, R. M. Paniago, and N. Y. Iha, "XPS characterization of sensitized n-TiO_2 thin films for dye-sensitized solar cell applications", *Appl. Surf. Sci.*, vol. 254, no. 6, pp. 1874–1879, 2008.

[118] R. Lukose, M. Lisker, F. Akhtar, M. Fraschke, T. Grabolla, A. Mai, and M. Lukosius, "Influence of plasma treatment on SiO_2/Si and Si_3N_4/Si substrates for large-scale transfer of graphene", *Sci. Rep.*, vol. 11, no. 1, pp. 1–10, 2021.

[119] C. S. Solanki and H. K. Singh,"Principle of Dielectric-Based Anti-reflection and Light Trapping, in *Anti-reflection and Light Trapping in c-Si Solar Cells*", Singapore: Springer, 2017, Chapter 3, pp. 43–63.

[120] S. Minoura, K. Kodera, T. Maekawa, K. Miyazaki, S. Niki, and H. Fujiwara, "Dielectric function of $Cu(In,Ga)Se_2$ based polycrystalline materials", *J. Appl. Phys.*, vol. 113, no. 6, p. 063505, 2013.

[121] R. Carron, E. Avancini, T. Feurer, B. Bissig, P. A. Losio, R. Figi, C. Schreiner, M. Bürki, E. Bourgeois, Z. Remes, M. Nesladek, S. Buecheler, and A. N. Tiwari, "Refractive indices of layers and optical simulations of $Cu(In,Ga)Se_2$ solar cells", *Sci. Technol. Adv. Mater.*, vol. 19, no. 1, pp. 396–410, 2018.

[122] S. Minoura, T. Maekawa, K. Kodera, A. Nakane, S. Niki, and H. Fujiwara, "Optical constants of $Cu(In,Ga)Se_2$ for arbitrary Cu and Ga compositions", *J. Appl. Phys.*, vol. 117, no. 19, p. 195703, 2015.

[123] C. Schinke, P. Christian Peest, J. Schmidt, R. Brendel, K. Bothe, M. R. Vogt, I. Kröger, S. Winter, A. Schirmacher, S. Lim, H. T. Nguyen, and D. Macdonald, "Uncertainty analysis for the coefficient of band-to-band absorption of crystalline silicon", *AIP Adv.*, vol. 5, no. 6, p. 067168, 2015.

[124] M. R. Vogt, H. Hahn, H. Holst, M. Winter, C. Schinke, M. Kontges, R. Brendel, and P. P. Altermatt, "Measurement of the optical constants of soda-lime glasses in dependence of iron content and modeling of iron-related power losses in crystalline si solar cell modules", *IEEE J. Photovolt.*, vol. 6, no. 1, pp. 111–118, 2016.

[125] L. Gao, R. Lemarchand, and M. Lequime, "Refractive index determination of SiO_2 layer in the UV/Vis/NIR range: Spectrophotometric reverse engineering on single and bi-layer designs", *J. Eur. Opt. Soc.*, vol. 8, p. 13010, 2013.

[126] Kevin Luke, Yoshitomo Okawachi, Michael R. E. Lamont, Alexander L. Gaeta and M. Lipson, "Broadband mid-infrared frequency comb generation in a Si_3N_4 microresonator", *Opt. Lett.*, vol. 40, no. 21, pp. 4823–486, 2015.

[127] H. P. Ma, H. L. Lu, J. H. Yang, X. X. Li, T. Wang, W. Huang, G. J. Yuan, F. F. Komarov, and D. W. Zhang, "Measurements of microstructural, chemical, optical, and electrical properties of silicon-oxygen-nitrogen films prepared by plasma-enhanced atomic layer deposition", *Nanomaterials*, vol. 8, no. 12, p. 1008, 2018.

[128] Z. H. Dai, R. J. Zhang, J. Shao, Y. M. Chen, Y. X. Zheng, J. D. Wu, and L. Y. Chen, "Optical properties of zinc-oxide films determined using Spectroscopic ellipsometry with various dispersion models", *J. Korean Phys. Soc.*, vol. 55, no. 3, pp. 1227–1232, 2009.

[129] G. Droulers, A. Beaumont, J. Beauvais, and D. Drouin, "Spectroscopic ellipsometry on thin titanium oxide layers grown on titanium by plasma oxidation", *J. Vac. Sci. Technol. B*, vol. 29, no. 2, p. 021010, 2011.

[130] S. Sarkar, V. Gupta, M. Kumar, J. Schubert, P. T. Probst, J. Joseph, and T. A. König, "Hybridized Guided-Mode Resonances via Colloidal Plasmonic Self-Assembled Grating", *ACS Appl. Mater. Interfaces*, vol. 11, no. 14, pp. 13752–13760, 2019.

[131] C. Stelling, C. R. Singh, M. Karg, T. A. König, M. Thelakkat, and M. Retsch, "Plasmonic nanomeshes: Their ambivalent role as transparent electrodes in organic solar cells", *Sci. Rep.*, vol. 7, p. 42530,, 2017.

[132] M. D. Huang, S. Du, H. Y. Li, C. W. Liu, and X. H. Tang, "A study on structure and optical properties of sputtered TiO_2 films", *Adv. Mater. Res.*, vol. 875-877, pp. 223–227, 2014.

[133] P. L. Washington, H. C. Ong, J. Y. Dai, and R. P. Chang, "Determination of the optical constants of zinc oxide thin films by spectroscopic ellipsometry", *Appl. Phys. Lett.*, vol. 72, no. 25, pp. 3261–3263, 1998.

[134] M. F. Al-Kuhaili, "Optical properties of hafnium oxide thin films and their application in energy-efficient windows", *Opt. Mater. (Amst)*, vol. 27, no. 3, pp. 383–387, 2004.

[135] J. M. Khoshman and M. E. Kordesch, "Optical properties of a-HfO_2 thin films", *Surf. Coatings Technol.*, vol. 201, no. 6, pp. 3530–3535, 2006.

[136] A. Wiatrowski, A. Obstarczyk, M. Mazur, D. Kaczmarek, and D. Wojcieszak, "Characterization of HfO_2 optical coatings deposited by MF magnetron sputtering", *Coatings*, vol. 9, no. 2, pp. 1–20, 2019.

[137] O. Hunderi and K. Johannessen, "Effective-medium description of superlattices and the effect on non-locality", *Superlattices Microstruct.*, vol. 3, no. 2, pp. 193–198, 1987.

[138] D. Caffrey, E. Norton, C. Coileáin, C. M. Smith, I. V. Shvets, and K. Fleischer, "Increasing the refractive index of materials via nanolamination: A-IGZO/TiO_2 nanolaminates", *Phys. Rev. Mater.*, vol. 2, no. 9, pp. 1–8, 2018.

[139] J. López-Medina, W. O. Carvalho, J. Vazquez-Arce, E. Moncada-Villa, O. N. Oliveira, M. H. Farías, H. Tiznado, and J. R. Mejía-Salazar, "Refractive index of ZnO ultrathin films alternated with Al_2O_3 in multilayer heterostructures", *Nanotechnology*, vol. 31, no. 50, p. 505715, 2020.

[140] R. Williams, "Photoemission of Electrons from Silicon into Silicon Dioxide", *IEEE Trans. Electron Devices*, vol. 12, no. 9, p. 503, 1965.

[141] B. Roul, M. Kumar, M. K. Rajpalke, T. N. Bhat, and S. B. Krupanidhi, "Binary group III-nitride based heterostructures: Band offsets and transport properties", *J. Phys. D: Appl. Phys.*, vol. 48, no. 42, p. 423001, 2015.

[142] S. Gutmann, M. Conrad, M. A. Wolak, M. M. Beerbom, R. Schlaf, M. T. Greiner, Z. H. Lu, *et al.*, "Thin-film metal oxides in organic semiconductor devices: Their electronic structures, work functions and interfaces", *J. Appl. Phys.*, vol. 2013, no. 9, pp. 1–16, 2013.

[143] I. S. Yu, Y. W. Wang, H. E. Cheng, Z. P. Yang, and C. T. Lin, "Surface passivation and antireflection behavior of ALD TiO_2 on n-type silicon for solar cells", *Int. J. Photoenergy*, vol. 2013, p. 431614, 2013.

[144] C. Dette, M. A. Pérez-Osorio, C. S. Kley, P. Punke, C. E. Patrick, P. Jacobson, F. Giustino, S. J. Jung, and K. Kern, "TiO_2 anatase with a bandgap in the visible region", *Nano Lett.*, vol. 14, no. 11, pp. 6533–6538, 2014.

[145] S. Gutmann, M. Conrad, M. A. Wolak, M. M. Beerbom, and R. Schlaf, "Work function measurements on nano-crystalline zinc oxide surfaces", *J. Appl. Phys.*, vol. 111, no. 12, p. 123710, 2012.

[146] T. V. Perevalov, V. A. Gritsenko, S. B. Erenburg, A. M. Badalyan, H. Wong, and C. W. Kim, "Atomic and electronic structure of amorphous and crystalline hafnium oxide: X-ray photoelectron spectroscopy and density functional calculations", *J. Appl. Phys.*, vol. 101, no. 5, p. 53704, 2007.

[147] A. Kumar, S. Mondal, and K. S. Rao, "Structural, electrical, band alignment and charge trapping analysis of nitrogen-annealed Pt/HfO_2/p-Si (100) MIS devices", *Appl. Phys. A Mater. Sci. Process.*, vol. 122, no. 12, pp. 11–14, 2016.

[148] S. S. Nekrashevich and V. A. Gritsenko, "Electronic structure of silicon oxynitride: Ab-initio and experimental study, comparison with silicon nitride", *J. Appl. Phys.*, vol. 110, no. 11, p. 114103, 2011.

[149] X. Q. Wei, B. Y. Man, M. Liu, C. S. Xue, H. Z. Zhuang, and C. Yang, "Blue luminescent centers and microstructural evaluation by XPS and Raman in ZnO thin films annealed in vacuum, N_2 and O_2", *Phys. B Condens. Matter*, vol. 388, pp. 145–152, 2007.

[150] A. Klein, C. Körber, A. Wachau, F. Säuberlich, Y. Gassenbauer, S. P. Harvey, D. E. Proffit, and T. O. Mason, "Transparent conducting oxides for photovoltaics: Manipulation of fermi level, work function and energy band alignment", *Materials (Basel)*, vol. 3, no. 11, pp. 4892–4914, 2010.

[151] M. G. Helander, M. T. Greiner, Z. B. Wang, and Z. H. Lu, "Pitfalls in measuring work function using photoelectron spectroscopy", *Appl. Surf. Sci.*, vol. 256, no. 8, pp. 2602–2605, 2010.

[152] J. Keller, K. V. Sopiha, O. Stolt, L. Stolt, C. Persson, J. J. Scragg, T. Törndahl, and M. Edoff, "Wide gap $(Ag,Cu)(In,Ga)Se_2$ solar cells with different buffer materials - A path to a better heterojunction", *Prog. Photovolt. Res. Appl.*, vol. 28, no. 4, pp. 237–250, 2020.

[153] J. Lindahl, U. Zimmermann, P. Szaniawski, T. Torndahl, A. Hultqvist, P. Salomé, C. Platzer-Björkman, and M. Edoff, "Inline $Cu(In,Ga)Se_2$ co-evaporation for high-efficiency solar cells and modules", *IEEE J. Photovolt.*, vol. 3, no. 3, pp. 1100–1105, 2013.

[154] C. Frisk, C. Platzer-Björkman, J. Olsson, P. Szaniawski, J. T. Wätjen, V. Fjällström, P. Salomé, and M. Edoff, "Optimizing Ga-profiles for highly efficient $Cu(In,Ga)Se_2$ thin film solar cells in simple and complex defect models", *J. Phys. D: Appl. Phys.*, vol. 47, no. 48, p. 485104, 2014.

[155] S. H. Wei and A. Zunger, "Band offsets at the CdS/$CuInSe_2$ heterojunction", *Appl. Phys. Lett.*, vol. 63, no. 18, pp. 2549–2551, 1993.

[156] T. Minemoto, T. Matsui, H. Takakura, Y. Hamakawa, T. Negami, Y. Hashimoto, T. Uenoyama, and M. Kitagawa, "Theoretical analysis of the effect of conduction band offset of window/CIS layers on performance of CIS solar cells using device simulation", *Sol. Energy Mater. Sol. Cells*, vol. 67, no. 1-4, pp. 83–88, 2001.

[157] J. H. Sung, J. H. Park, D. S. Jeon, D. Kim, M. J. Yu, A. C. Khot, T. D. Dongale, and T. G. Kim, "Retention enhancement through capacitance-dependent voltage division analysis in 3D stackable TaO_x/HfO_2-based selectorless memristor", *Mater. Des.*, vol. 207, p. 109845, 2021.

[158] M. Rahimabady, L. Lu, and K. Yao, "Nanocomposite multilayer capacitors comprising $BaTiO_3 - TiO_2$ and poly (vinylidene fluoride-hexafluoropropylene) for dielectric-based energy storage ", *J. Adv. Dielectr.*, vol. 4, no. 2, p. 1450009, 2014.

[159] G. Z. Zhang, H. Wu, C. Chen, T. Wang, P. Y. Wang, L. Q. Mai, J. Yue, and C. Liu, "Transparent capacitors based on nanolaminate $Al_2O_3/TiO_2/Al_2O_3$ with H_2O and O_3 as oxidizers", *Appl. Phys. Lett.*, vol. 104, no. 16, pp. 1–5, 2014.

[160] C. Y. Chou, C. H. Lin, W. H. Chen, B. J. Li, and C. Y. Liu, "High-dielectric-constant silicon nitride thin films fabricated by radio frequency sputtering in Ar and Ar/N_2 gas mixture", *Thin Solid Films*, vol. 709, p. 138198, 2020.

[161] N. Konofaos, E. K. Evangelou, X. Aslanoglou, M. Kokkoris, and R. Vlastou, "Dielectric properties of CVD grown SiON thin films on Si for MOS microelectronic devices", *Semicond. Sci. Technol.*, vol. 19, no. 1, pp. 50–53, 2004.

[162] N. H. Langton and D. Matthews, "The dielectric constant of zinc oxide over a range of frequencies", *Br. J. Appl. Phys.*, vol. 9, no. 11, pp. 453–456, 1958.

[163] R. A. Matula, "Electrical resistivity of copper, gold, palladium, and silver", *J. Phys. Chem. Ref. Data*, vol. 8, no. 4, pp. 1147–1298, 1979.

[164] B. Giroire, M. Ali Ahmad, G. Aubert, L. Teule-Gay, D. Michau, J. J. Watkins, C. Aymonier, and A. Poulon-Quintin, "A comparative study of copper thin films deposited using magnetron sputtering and supercritical fluid deposition techniques", *Thin Solid Films*, vol. 643, pp. 53–59, 2017.

[165] L. De Los Santos Valladares, D. H. Salinas, A. B. Dominguez, D. A. Najarro, S. I. Khondaker, T. Mitrelias, C. H. Barnes, J. A. Aguiar, and Y. Majima, "Crystallization and electrical resistivity of Cu_2O and CuO obtained by thermal oxidation of Cu thin films on SiO_2/Si substrates", *Thin Solid Films*, vol. 520, no. 20, pp. 6368–6374, 2012.

[166] S. Lange, S. Hensel, A. Hähnel, V. Naumann, T. Urban, M. Müller, and C. Hagendorf, "Contact and Bulk Resistivity Screening for Advanced Crystalline Silicon Solar Cell Concepts by an Economical and Reliable Transfer Length Measurement Method Based on Laser Micro-Patterning", *Phys. Status Solidi Appl. Mater. Sci.*, vol. 218, no. 2, pp. 1–6, 2021.

[167] S. Kailasam, R. A. Vijayan, D. Amirthaganesan, S. Srinath, V. Viswanathan, S. Masilamani, P. Krishnamoorthy, and M. Varadharajaperumal, "Accuracy of Contact Resistivity Measurements for Electron-Selective Titanium Oxide Contacts in n-Type c-Si Solar Cell", *IEEE J. Photovolt.*, vol. 11, no. 3, pp. 613—619, 2021.

[168] L. G. Gerling, S. Mahato, C. Voz, R. Alcubilla, and J. Puigdollers, "Characterization of transition metal oxide/silicon heterojunctions for solar cell applications", *Appl. Sci.*, vol. 5, no. 4, pp. 695–705, 2015.

[169] S. Krause, K. Kaufmann, K. Lancaster, V. Naumann, S. Großer, and C. Hagendorf, "Fs-laser micro machining for μ-TLM resistivity test structures in photovoltaic TCO multilayers", *Photonics Sol. Energy Syst. VI*, vol. 9898, p. 98980R, 2016.

[170] D. K. Schroder, *Semiconductor Material and Device Characterization*, 3rd ed. United States of America: Wiley, 2006.

[171] A. W. Dweydari and C. H. Mee, "Work function measurements on (100) and (110) surfaces of aluminium", *Phys. Status Solidi*, vol. 27, no. 1, pp. 223–230, 1975.

[172] S. M. Sze and K. K. Ng, *Physics of Semiconductor Devices*, 3rd ed., New Jersey: Wiley, 2007

[173] J. B. E.H.Nicollian, *Nicollian Metal Oxide Semiconductior Physics and Technology*, United States of America: Wiley, 1982.

[174] R. Winter, J. Ahn, P. C. McIntyre, and M. Eizenberg, "New method for determining flatband voltage in high mobility semiconductors", *J. Vac. Sci. Technol. B*, vol. 31, no. 3, p. 030604, 2013.

[175] W. J. Lee, N. S. Parmar, and J. W. Choi, "High work function MoO_2 and ReO_2 contacts for p-type Si and GaN by a room-temperature non-vacuum process", *Mater. Sci. Semicond. Process.*, vol. 71, pp. 374–377, 2017.

[176] H. Y. Barbara Lafuente, R. T. Downs and N. Stone, "The power of databases: The RRUFF project", in *Highlights Mineralogical Crystallography*, Boston, De Gruyter (O), 2016, Chapter 1, pp. 1–30.

[177] H. C. Swart, E. D. Van Hattum, W. M. Arnoldbik, and F. H. Habraken, "Comparison of SiO_x structure in RF sputtered samples", *Phys. Status Solidi C Conf.*, vol. 1, no. 9, pp. 2286–2291, 2004.

Appendices

A

AutoCAD Design

Fig. A.1 presents the design of the shadow masks developed in the AutoCAD platform. The outer circle represents the edge of the Si wafer form where the shadow masks would be fabricated, and the inner circle the imposed limited of usable wafer. This limit was self imposed, since the resit coating on the wafer boards is not uniform, what could lead to problems. So, that area was avoided. On the design, four frame-like pattern can be seen and one line pattern for each different configuration (A, B, C, and D)[1]. The patterns were organized in a way to minimize the number of fragile areas where the wafer could brake.

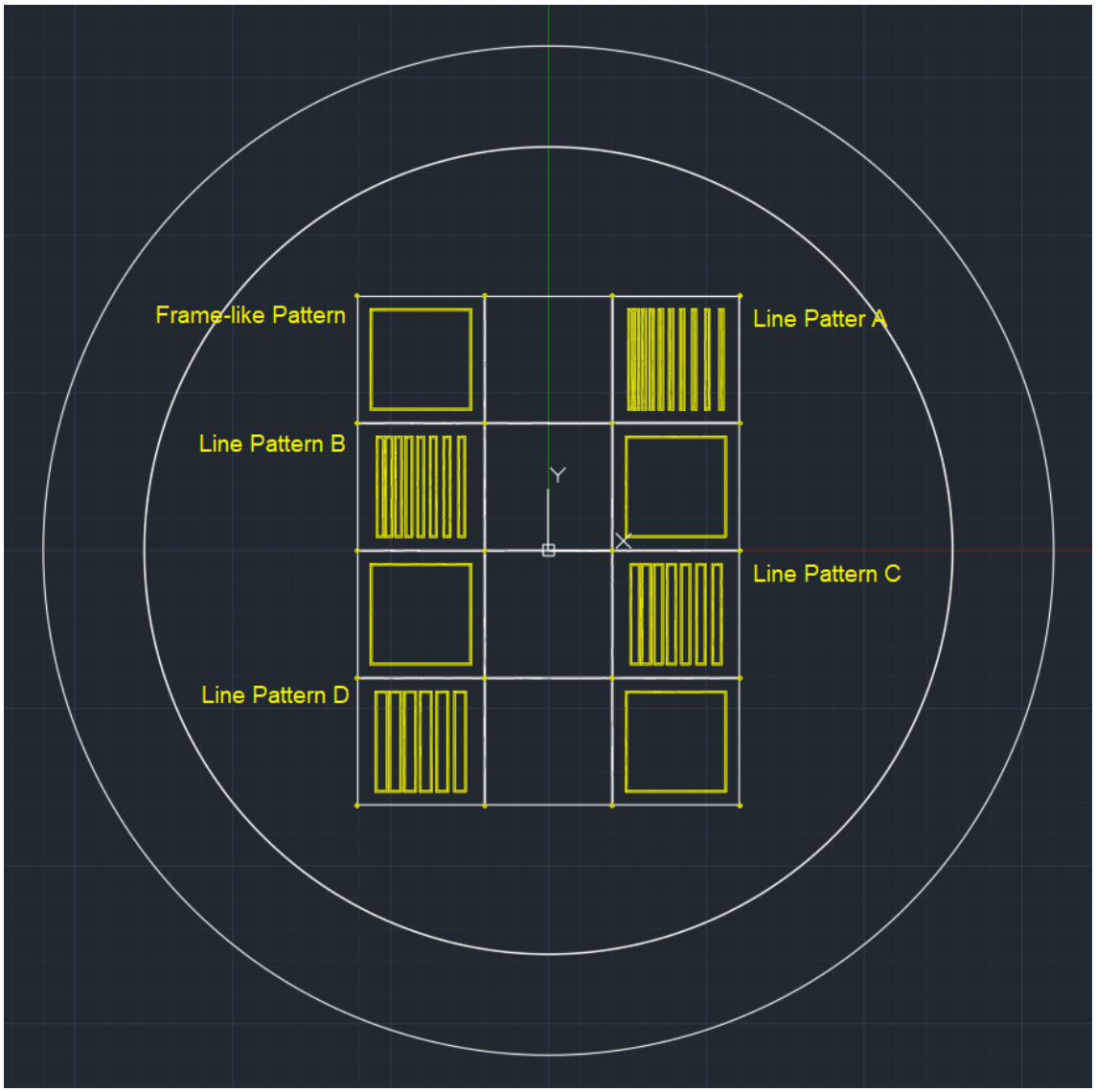

Figure A.1: Print screen of the AutoCAD design of the developed shadow mask.

[1] If necessary recall the shadow masks dimensions in Table 3.4 and Fig. 3.7.

B

Raman Spectrum

Fig. B.1 shows the similarity between the measured Si substrate and the SiO_x layer Raman spectra. No peak corresponding to the SiO_2 wa found. The peak at 300 cm^{-1}, the plateau at 950-1000 $cm-1$, and the peak at $\sim$ 525 cm^{-1} were assigned to c-Si. [176]

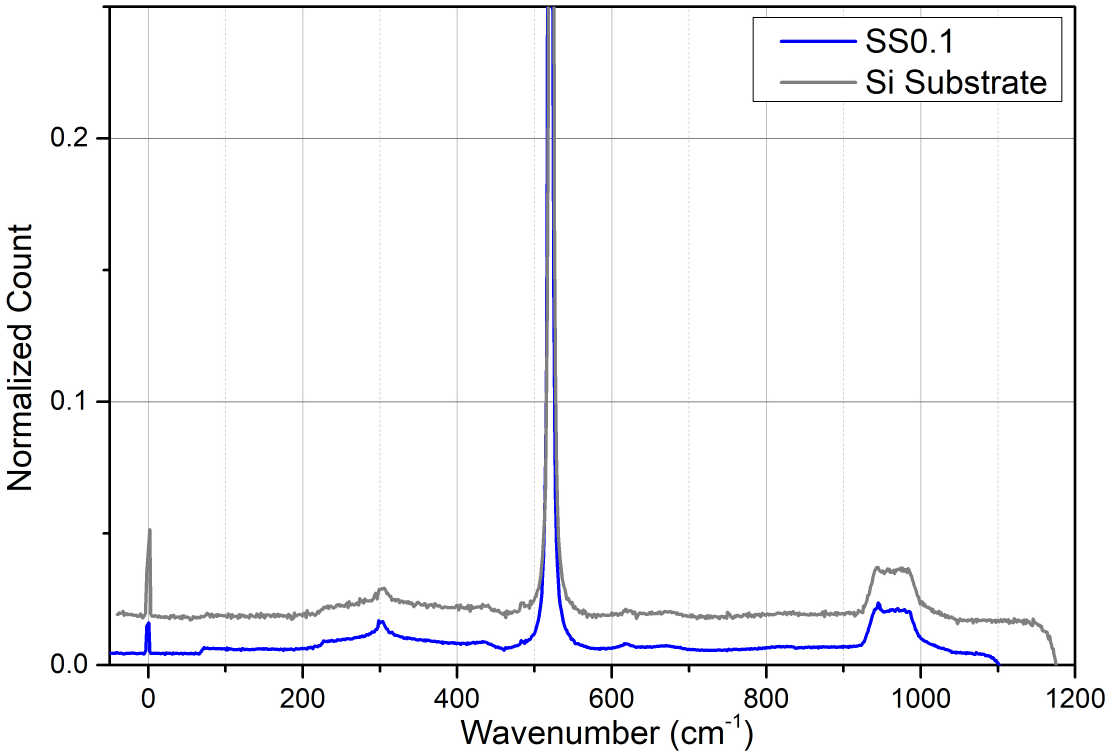

Figure B.1: Sample SS0.1 and Si substrate Raman spectra.

C

XPS Spectra

Fig. C.1 presents the as measured XPS survey spectrum of sample SS0.1, an individual layer of SiO_x. The peaks were identified with the Advantage software, and can be seen that more than the sample element peaks (C, Si, and O) can be identified. The OKL1 and OKL2 peaks correspond to the emission of an Auger electron, due to a transmission from levels L1 and L2 to K, respectively. The sodium (Na), Fluorine (F), N, and calcium (Ca) peaks are considered contaminations, with negligible content.

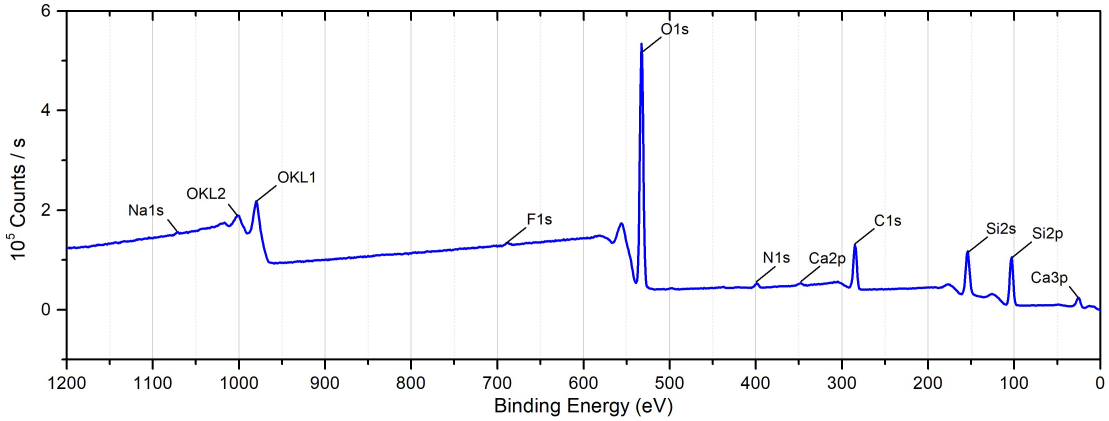

Figure C.1: As measured XPS survey of sample SS0.1.

Fig. C.2, C.3, C.4, C.5, C.6, and C.7, show the elements spectrum regions used for the element quantification of samples SS10.2, SS5.3, SS5.4, TZ2, ZT3, and HT2, respectively. Regarding sample SS10.2 O 1s spectra, Fig. C.2 (a), is noticeable the appearance of a new C=O peak [118], when comparing the samples SS0.1, which was also observed in sample SS10.1. The Si 2p spectra of the samples SS5.3 and SS5.4 (Fig. C.3 (b) and Fig. C.4 (b), respectively) show one extra peak, when compared with samples SS0.1 and SS0.2, identified as an Si^{+1} oxidation state [177]. The sub-oxide Ti 2p states can be observed in samples ZT3 and HT2 (Fig. C.6 (c) and Fig. C.7 (c), respectively), due to the nanolaminate top layer being TiO_x. Also, on sample HT2 spectra (Fig. C.7 (b)) is possible to observe two artefacts: (1) one small and broad peak close to the Hf $4f_{5/2}$ peak, identified as a weak HfO_2 loss feature, and (2) the charge transfer satellite, identified before on sample TZ0.1.

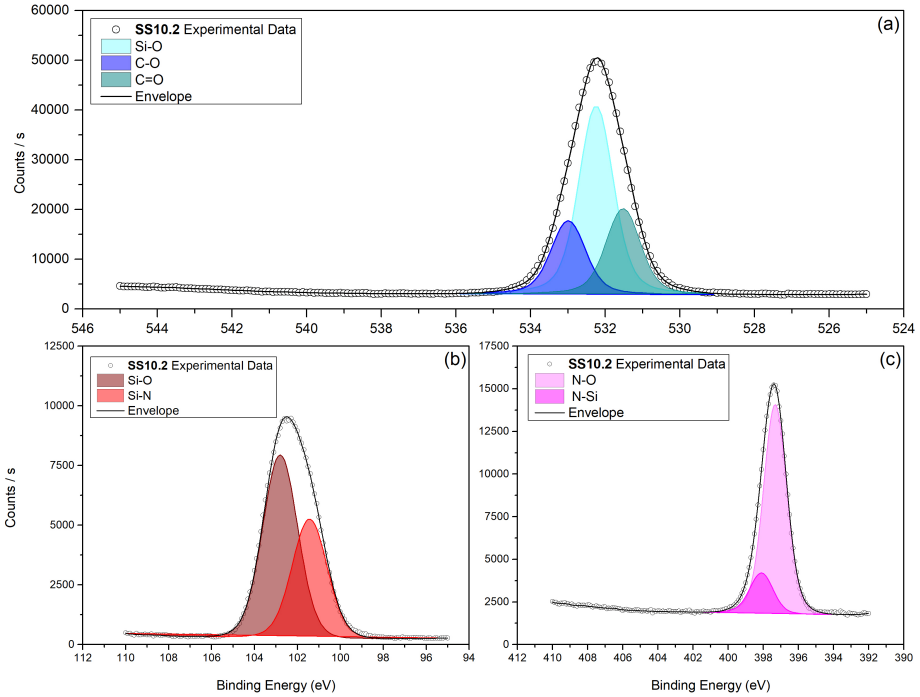

Figure C.2: As measured XPS spectra of (a) O 1s, (b) Si 2p, (c) Ni 1s binding energy regions for Clean analysis of sample SS10.2, respectively.

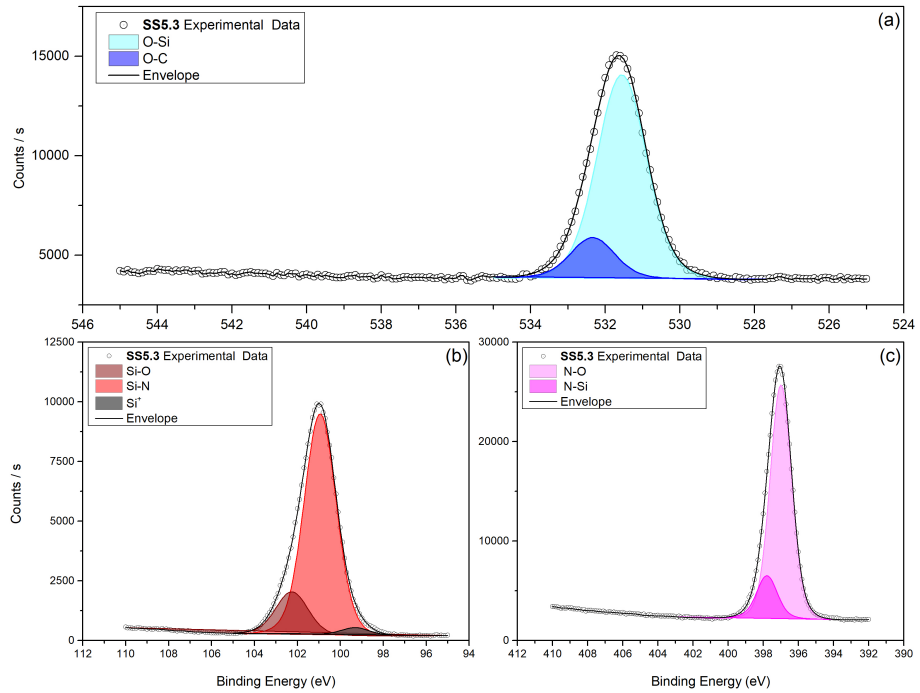

Figure C.3: As measured XPS spectra of (a) O 1s, (b) Si 2p, (c) Ni 1s binding energy regions for Clean analysis of sample SS5.3, respectively.

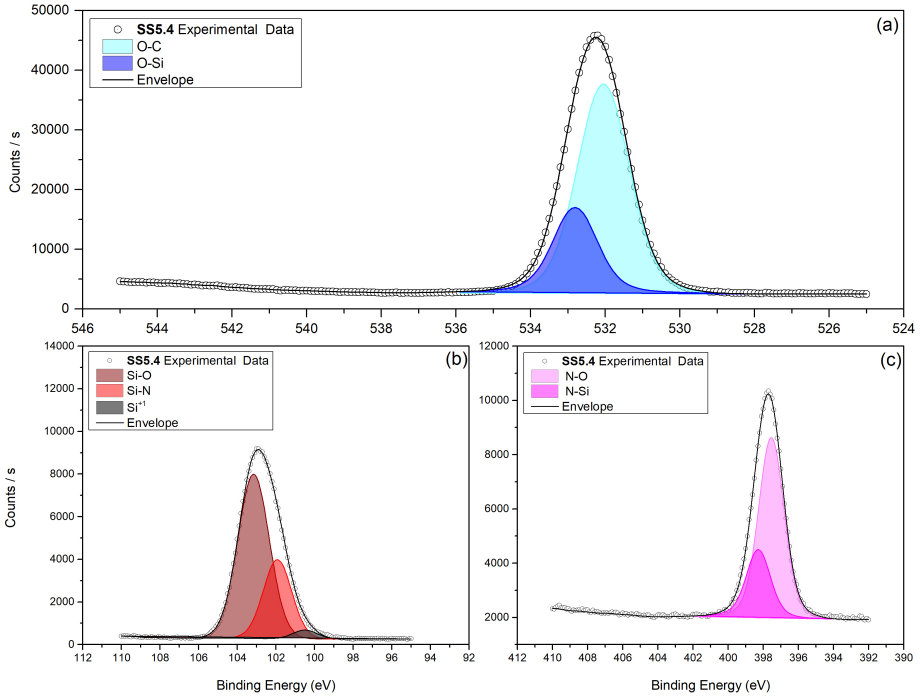

Figure C.4: As measured XPS spectra of (a) O 1s, (b) Si 2p, (c) Ni 1s binding energy regions for Clean analysis of sample SS5.4, respectively.

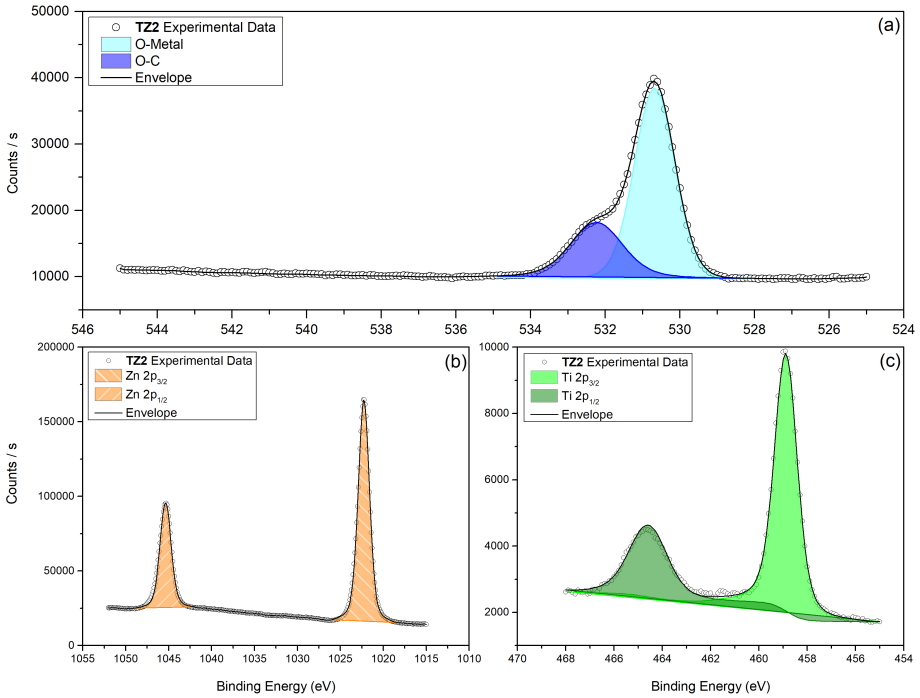

Figure C.5: As measured XPS spectra of (a) O 1s, (b) Zn 2p, (c) Ti 2p binding energy regions for Clean analysis of sample TZ2, respectively.

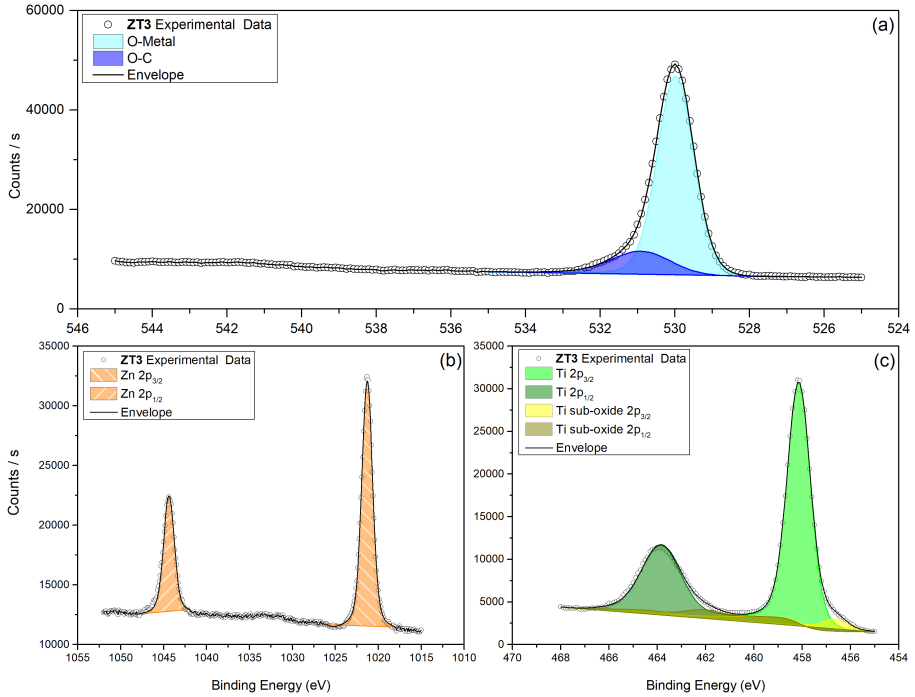

Figure C.6: As measured XPS spectra of (a) O 1s, (b) Zn 2p, (c) Ti 2p binding energy regions for Clean analysis of sample ZT3, respectively.

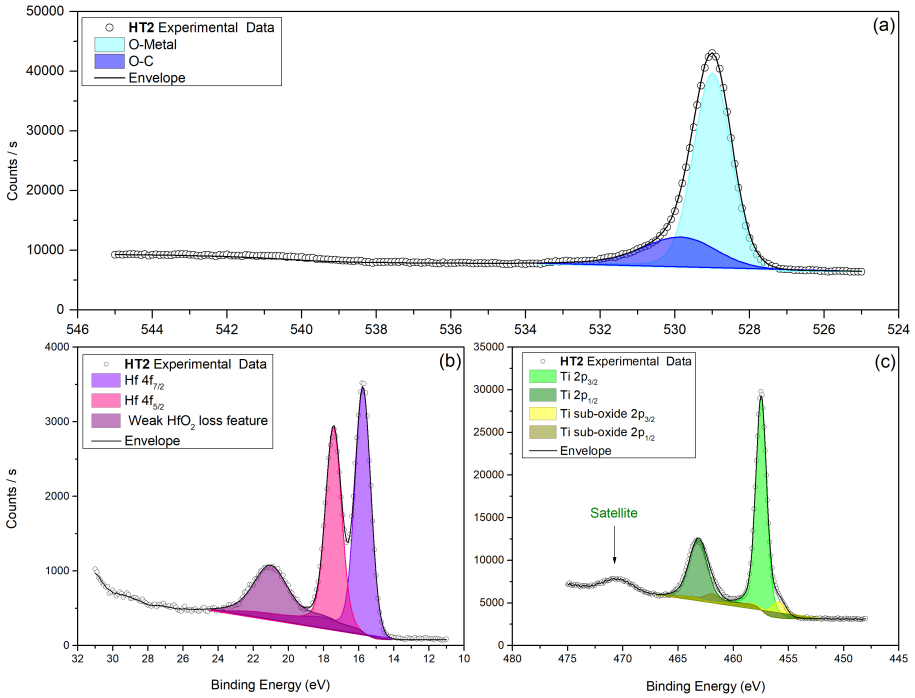

Figure C.7: As measured XPS spectra of (a) O 1s, (b) Hf 4f, (c) Ti 2p binding energy regions for Clean analysis of sample HT2, respectively.

D

Reflectance graphics and Samples Refractive Index and Thickness

Fig. D.1 (a), (b) and (c), shows the reflectance graphics, measured and determined, of the individual layers of SiO_x, HfO_x, and SiN_x, respectively. The corresponding graphics of the individual layers of TiO_x and ZnO_x were already presents in Fig. 4.26.

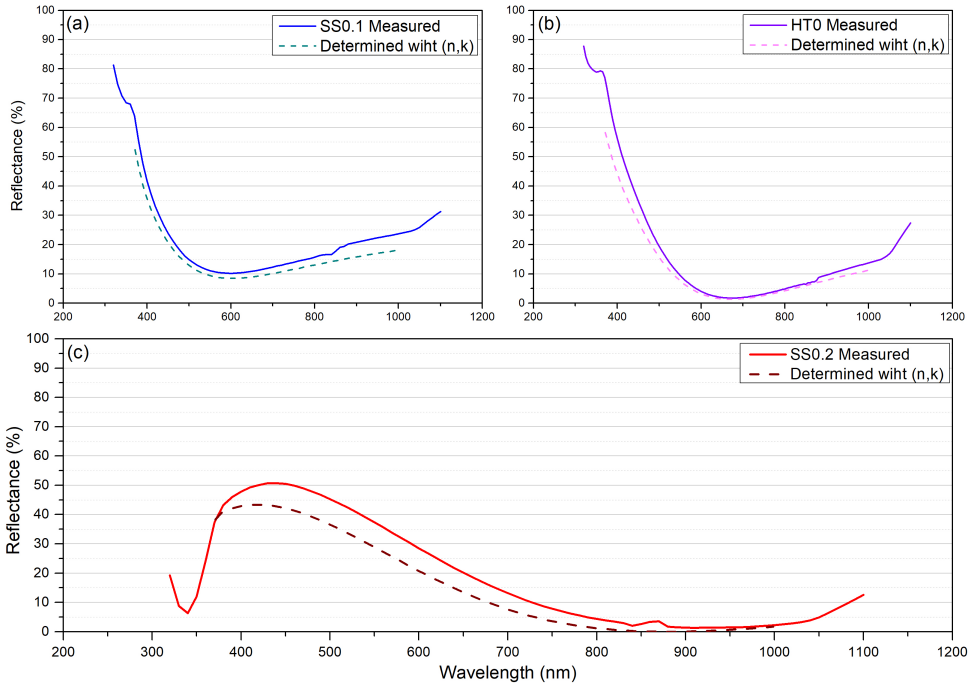

Figure D.1: Reflectance graphics, with the measured and determined with optical constants (n,k), for samples (a) SS0.1, (b) HT0, and (c) SS0.2.

Table D.1: Refractive index values, of all samples, determined with Ellipsometry.

Sample	SS0.1	SS0.2	SS10.1	SS10.2	SS10.3	SS10.4
Refractive Index at 600nm	1.48	1.95	1.62	1.65	1.72	1.58
Sample	SS0.1	SS0.2	SS5.1	SS5.2	SS5.3	SS5.4
Refractive Index at 600nm	1.48	1.95	1.71	1.57	1.78	1.56
Sample	TZ0.1	TZ0.2	TZ1.1	TZ1.2	TZ2	TZ3
Refractive Index at 600nm	1.91	1.87	1.93	2.02	2.04	1.91
Sample	TZ0.2	TZ0.1	ZT1.1	ZT1.2	ZT2	ZT3
Refractive Index at 600nm	1.87	1.91	1.94	1.85	2.01	2.06
Sample	HT0	TZ0.1	HT1	HT2	-	-
Refractive Index at 600nm	1.74	1.91	1.80	1.78	-	-

Table D.1 lists the refractive index values for all analysed samples. With these, it is more evident the nanolaminates tendency and refractive index variation upon sublayer thickness and composition variation.

Table D.2: Nominal and measured, with profilometer and ellipsometer, thickness values of the studied samples deposited on Si substrate.

Sample	Nominal	Profilometer	Ellipsometer
SS0.1	100	[1]	96.93
SS0.2	100	[1]	113.68
SS10.1	20	[1]	25.3
SS10.2	40	[1]	48.45
SS10.3	30	[1]	36.4
SS10.4	30	[1]	34.93
SS5.1	15	[1]	19.52
SS5.2	15	[1]	19.28
SS5.3	20	[1]	24.35
SS5.4	20	[1]	23.39
TZ0.1	30	[1]	24.1
TZ0.2	30	30.10	23.15
TZ1.1	30	26.63	28.09
TZ1.2	30	29.29	27
TZ2	30	[1]	26.85
TZ3	30	34.36	31.83
ZT1.1	30	28.84	27.04
ZT1.2	30	29.20	29.20
ZT2	30	[1]	29.76
ZT3	30	28.78	31.83
HT0	100	91.97	96.03
HT1	30	28.89	34.43
HT2	30	30.51	35.51

Table D.2 lists the nominal, measured by profilometer and ellipsometer thickness values for all analysed samples. As it is clear, most of measured samples actual thickness is not equal to the nominal value. This is due to the estimation of the deposition time, and because no thickness control occurs during deposition. Some have big deviation and other have below 1 nm deviation, although, on average, the samples have a $\pm$ 5.1 nm deviation from the nominal value.

[1] Was no possible to measure the samples thickness with the Profilometer, because the ink lines did not wash off completely after the deposition.